

AperTO - Archivio Istituzionale Open Access dell'Università di Torino

Characterization of MOFs. 2. Long and Local Range Order Structural Determination of MOFs by Combining EXAFS and Diffraction Techniques

This is the author's manuscript

Original Citation:

Availability:

This version is available <http://hdl.handle.net/2318/138918> since 2017-05-12T14:41:12Z

Publisher:

Royal Society of Chemistry

Published version:

DOI:10.1039/9781849737586-00143

Terms of use:

Open Access

Anyone can freely access the full text of works made available as "Open Access". Works made available under a Creative Commons license can be used according to the terms and conditions of said license. Use of all other works requires consent of the right holder (author or publisher) if not exempted from copyright protection by the applicable law.

(Article begins on next page)



UNIVERSITÀ DEGLI STUDI DI TORINO

This is an author version of the contribution published on:

Questa è la versione dell'autore dell'opera:

E. Borfecchia, D. Gianolio, G. Agostini, S. Bordiga, C. Lamberti,

“Characterization of MOFs. 2. Long and Local Range Order Structural Determination of MOFs by Combining EXAFS and Diffraction Techniques”

in: *Metal Organic Frameworks as Heterogeneous Catalysts*; F. X. Llabrés i Xamena and J. Gascón, Ed.; Royal Society of Chemistry, Cambridge, 2013, p. 143-208, Chapter 5

The definitive version is available at:

La versione definitiva è disponibile alla URL:

<http://pubs.rsc.org/en/content/chapter/bk9781849735728-00143/978-1-84973-572-8#!divabstract>

2.4. Long and local range order structural determination of MOFs by combining EXAFS and diffraction techniques

E. Borfecchia^a, D. Gianolio^{a,b}, G. Agostini^a, S. Bordiga^a, and C. Lamberti^{a,*}

^a*Department of Chemistry, NIS Centre of Excellence and INSTM Reference Center, Via Giuria 7, University of Turin, 10125 Torino, Italy. E-mail carlo.lamberti@unito.it*

^b*Diamond Light Source Ltd, Harwell Science and Innovation Campus, OX11 0DE, Didcot, United Kingdom*

1. Introduction

This chapter is divided into two parts. The former, including Sections 2, 3 and 4, provides the basic concepts needed to understand the physics that is behind X-rays and neutron scattering and photoelectron backscattering. This first part has a specific didactic purpose. At the beginning, the scattering process is introduced in a general way and only successively differentiation between crystalline samples and amorphous samples is made, leading to the Bragg equation or to the Debye equation and to the Pair Distribution Function (PDF) approach, respectively. The basics of Extended X-ray Absorption Fine Structure (EXAFS) spectroscopy is also reported. The latter includes recent examples from the literature where the concepts described in the first part have been applied to the understanding of the structure of different MOFs materials.

The large unit cells, the enormous flexibility and variation in structural motifs of MOFs represent a big challenge in the characterization of MOF materials, particularly in cases where single crystal diffraction data are not available. Indeed, solving complex structures with powder data, even if of high quality, is far to be trivial.¹⁻⁵ The selected cases reported in Section 5 will show that in cases where only powder diffraction data are available additional structural information, are often mandatory in order to solve the structure. Three additional and complementary techniques will be discussed in this chapter. (i) Neutron powder diffraction (NPD) data allows to better define the structure of the organic linkers (formed by low-Z elements only) and to obtain data with higher signal/noise in the high q region: $q = 4\pi \sin(\theta)/\lambda$. (ii) Total scattering (PDF approach) allows to shed light on the structure of amorphous MOFs and to provide additional information of crystalline ones. (iii) The atomic selectivity of EXAFS spectroscopy, performed at the metal K- or L-edges, provides the local structure of the inorganic cornerstones or backbones. There are cases where the inorganic cornerstones does not follow the symmetry of the overall structure. In such cases diffraction techniques will just "see" an average structure, missing the local structure: a lack that may be critical for understanding the specific properties of the material. In such cases PDF and EXAFS spectroscopy can be fundamental to understand the actual structure of the material as they do not require long range periodicity. In particular, EXAFS is the tool that provides complementary structural information on the inorganic cluster and the way it binds to the ligand. Selected examples will show how EXAFS and/or PDF will be relevant in: (i) confirming the structure obtained from diffraction refinements; (ii) highlighting that the inorganic cornerstone has a lower symmetry with respect to that of the organic framework; (iii) obtaining structural information on MOF subjected to amorphization processes (iv) obtaining the local structure of the inorganic cluster in the desolvated material after coordination of a probe (or reactant) molecule, including cluster deformation upon molecule coordination and metal-molecule binding distance; (v) evidencing the presence of impurities in form of amorphous extra-phases.

This chapter is not aimed in reporting an exhaustive review on the most relevant papers that have significantly contributed in understanding MOFs structure, so the reported bibliography is by no way comprehensive and has not been chosen on the basis of the scientific impact of the papers. The chapter is conversely aimed to provide general guidelines and to explain the information that can be obtained using the different structural techniques and to stress their complementarity. As detailed in a different chapter of this book,⁶ also vibrational and electronic spectroscopies are

extremely informative. Although not directly described in this chapter, theoretical calculations represent an important support to the experimental techniques, allowing to check for example the stability of a structure inferred from Rietveld refinement. For a detailed description of density functional theory (DFT) methods applied to MOFs materials the reader is referred to another chapter of the present book.⁷

2. X-rays and neutron scattering: basic background

2.1. X-ray scattering: theoretical background

In this Section first the physics of the X-ray elastic scattering process will be briefly discussed, showing how to derive very general equations, valid both for crystalline materials and less ordered systems. Subsequently, the peculiarities of the X-ray scattering both from perfect crystals and non-crystalline samples, as amorphous solids and solutions will be highlighted. The fundamental mathematical instruments employed for data modeling will be therefore separately discussed depending on the ordering level. In particular, the Laue conditions and the structure factor equation will be introduced for crystalline systems, whereas the Debye equation and the radial Pair Distribution Functions (PDF) formalism will be presented in relation to less-ordered materials. With this background it will be possible to investigate not only the large variety of crystalline MOFs but also the fraction of amorphous MOFs obtained after gas absorption or pressure gradients. In addition, crystallization processes, where the MOFs structure progressively emerges from the precursors in the solvent medium, can be monitored.

X-rays are suitable for structural determination because they are photons having a wavelength λ of the same order of the interatomic distance in condensed matter. The photon energy is linked to the photon wavelength (λ) by the relation $E = h\nu = hc/\lambda$, c being the speed of light ($c = 2.9979 \cdot 10^{10}$ m/s), h the Planck constant ($h = 6.626 \cdot 10^{-34}$ Js), so that: $hc = 12.3984 \text{ \AA keV}$. As a consequence, the relationship between photon energy (in keV) and the photon wavelength (λ) is:

$$E = 12.3984 (\text{\AA keV}) / \lambda \quad (1)$$

2.1.1 X-ray elastic scattering: basic physical principles. When an X-ray beam interacts with the sample, a part of the incoming radiation is elastically scattered. Details on the quantum-mechanical theory developed to describe such process can be found in the original reports by Waller and Wentzel,⁸⁻¹¹ as well as in later specialized literature.¹²⁻¹⁴ Hereinafter, only a synthetic discussion of fundamental concepts and key equations is proposed. Once an X-ray plane wave of wavevector \mathbf{k} is impinging on a sample having an electron density $\rho_e(\mathbf{r})$, the amplitude of the scattered X-ray wave $A(\mathbf{q})$ is expressed by Eq. (2):

$$A(\mathbf{q}) = \int \rho_e(\mathbf{r}) \exp(-i\mathbf{q} \cdot \mathbf{r}) d\mathbf{r} \quad (2)$$

where the integration on \mathbf{r} runs on the space occupied by the sample. In Eq. (2), $\mathbf{q} = \mathbf{k} - \mathbf{k}_0$ is the wave vector proportional to the momentum transfer ($\mathbf{p}: \mathbf{p} = h/(2\pi)\mathbf{q}$) during the elastic scattering interaction (scattering vector), as schematically represented in Figure 1a, where \mathbf{k}_0 and \mathbf{k} are the incident and the scattered wave vectors respectively, with $|\mathbf{k}_0| = |\mathbf{k}| = 2\pi/\lambda$. From the simple geometrical construction in Figure 1b it is evident that the modulus of the scattering vector is:

$$q = |\mathbf{q}| = 4\pi \sin\theta / \lambda \quad (3)$$

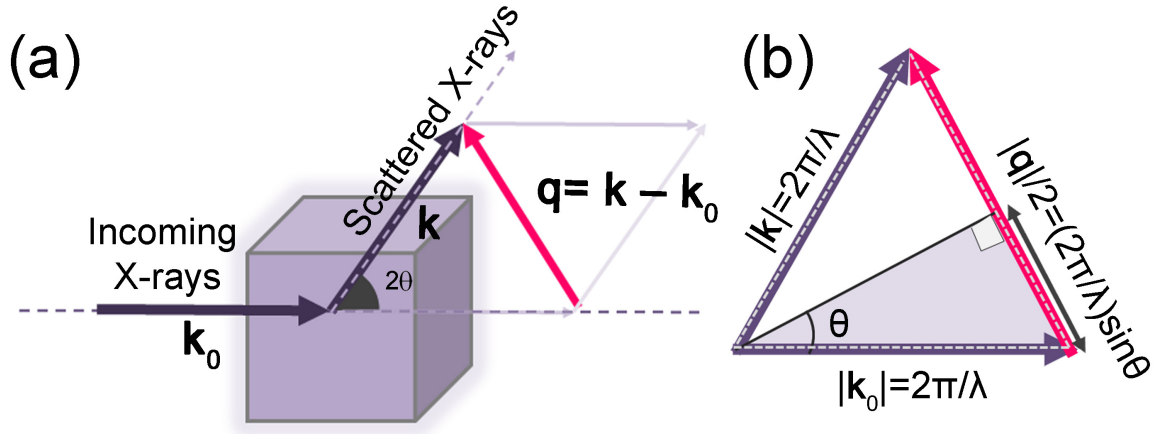


Figure 1. Part (a): schematic representation of the elastic scattering process; \mathbf{k}_0 and \mathbf{k} are the incident and the scattered wave vectors respectively, while $\mathbf{q} = \mathbf{k} - \mathbf{k}_0$ is the vector describing the momentum transfer during the interaction, and 2θ is the scattering angle. In the experiment, a detector is positioned along the \mathbf{k} direction to collect scattered intensity $I(\mathbf{q}) = |A(\mathbf{q})|^2$, see Eq. (4). Part (b): Geometrical construction for the determination of the modulus of the scattering vector $|\mathbf{q}| = 4\pi\sin\theta/\lambda$. Unpublished figure.

The X-ray scattering amplitude $A(\mathbf{q})$ and the sample electron density $\rho_e(\mathbf{r})$, expressed as a function of the 3D coordinate \mathbf{r} , are related by a Fourier transform, i.e. Eq. (2). This relation is of key importance and shows how the X-ray scattering signal is intimately dependent on the sample structure. However, we are experimentally limited to measure only the square modulus of the scattering amplitude $A(\mathbf{q})$, that is the scattered intensity $I(\mathbf{q})$ expressed by Eq. (4):

$$I(\mathbf{q}) = |A(\mathbf{q})|^2 = \left| \int \rho_e(\mathbf{r}) \exp(-i\mathbf{q} \cdot \mathbf{r}) d\mathbf{r} \right|^2 \quad (4)$$

As will be discussed in details in Section 2.1.4.4, any information on the X-ray phase is unavoidably lost: this long-standing complication in crystallography is well-known as the “phase problem”.¹⁵ As a consequence, it is impossible to apply directly the Fourier transform relation between $\rho_e(\mathbf{r})$ and $I(\mathbf{q})$ and therefore determine $\rho_e(\mathbf{r})$ from the measured $I(\mathbf{q})$.

However, we are allowed to express the global electron density $\rho_e(\mathbf{r})$ as a superimposition of the individual atomic electron densities centered in the nuclear positions \mathbf{r}_n , Eq. (5), where ρ_n is the electron density of the n^{th} atom and the vector \mathbf{r} describes a generic position from the origin of the reference system.

$$\rho_e(\mathbf{r}) = \sum_n \rho_n(\mathbf{r}) \otimes \delta(\mathbf{r} - \mathbf{r}_n) = \sum_n \rho_n(\mathbf{r} - \mathbf{r}_n) \quad (5)$$

where \otimes represent the convolution product of two functions and where δ is the Dirac delta-function. By combining Eq. (2) and eq. (5) it is possible to express the scattering amplitude $A(\mathbf{q})$ in the framework of the \mathbf{r}_n positions as follows:

$$\begin{aligned} A(\mathbf{q}) &= \int \left[\sum_n \rho_n(\mathbf{r} - \mathbf{r}_n) \right] e^{(-i\mathbf{q} \cdot \mathbf{r} - i\mathbf{q} \cdot \mathbf{r}_n + i\mathbf{q} \cdot \mathbf{r}_n)} d\mathbf{r} = \\ &= \sum_n \left[\int \rho_n(\mathbf{r} - \mathbf{r}_n) e^{-i\mathbf{q} \cdot (\mathbf{r} - \mathbf{r}_n)} d(\mathbf{r} - \mathbf{r}_n) \right] e^{-i\mathbf{q} \cdot \mathbf{r}_n} = \sum_n f_n(\mathbf{q}) e^{-i\mathbf{q} \cdot \mathbf{r}_n} \end{aligned} \quad (6)$$

where the index n runs over all atoms included in the sample (i.e. on a number of atoms comparable with the Avogadro number !) and where $f_n(\mathbf{q})$ is the so-called atomic form factor for the n^{th} atom,^{13,14} which is the Fourier transform of its electron density, as evidenced in Eq. (7):

$$f_n(\mathbf{q}) = \int \rho_n(\mathbf{r}) \exp(-i\mathbf{q} \cdot \mathbf{r}) d\mathbf{r} \quad (7)$$

Please note that Eq. (7) mirrors for the single atom Eq. (2), that holds for the whole sample. Considering that the atoms can be approximated as spheres, the atomic form factor $f_n(\mathbf{q})$ can be expressed as a function of the modulus of \mathbf{q} , i.e. $f_n(q)$. The scattered intensity can be therefore expressed as in Eq. (8):

$$I(\mathbf{q}) = \left| \sum_n f_n(q) \exp(-i\mathbf{q} \cdot \mathbf{r}_n) \right|^2 = \quad (8)$$

Atomic form factor (also referred to as atomic scattering factor) plays a crucial role in the X-rays diffraction theory. A brief description of their principal properties is therefore proposed in the next Section.

2.1.2 X-rays atomic form factors. The scattering properties of a specific atom are determined by the shape of its electron density, i.e. by the spatial charge distribution in the atomic orbitals. Here we are discussing the atomic form factor of a single, isolated, atom: the suffix n in Eq. (7) can be hence removed in both $f(q)$ and $\rho(r)$. Using Euler's formula¹⁶ we can write:

$$f(q) = \int \rho(\mathbf{r}) \exp(-i\mathbf{q} \cdot \mathbf{r}) d\mathbf{r} = \int \rho(\mathbf{r}) \cos(\mathbf{q} \cdot \mathbf{r}) d\mathbf{r} - i \int \rho(\mathbf{r}) \sin(\mathbf{q} \cdot \mathbf{r}) d\mathbf{r} \quad (9)$$

The integrals in Eq. (9) formally run over the whole space, while actually they run in the small region where the atomic electron density is significantly different from zero. So, depending on the specific atomic species considered, the integrals run over a sphere of radius in the 0.3–3.0 Å range,¹⁷ see Figure 2. As already mentioned, the electron density $\rho(\mathbf{r})$ for an isolated atom exhibits spherical symmetry, so that $\rho(-\mathbf{r}) = \rho(\mathbf{r})$.¹⁸ Under such assumption the sinus-FT in the third hand term of Eq. (9) is null (as all integrals over the whole space of an odd function) and $f(q)$ is a real function.

The fact that atoms have spatially extended orbitals instead of point-charges ones causes a reduction in the coherently scattered intensity. This reduction will be more efficient the larger either \mathbf{q} or \mathbf{r} become, because the phase shift, among the $d\mathbf{r}$ regions where the integral is performed, is determined by the scalar product $\mathbf{q} \cdot \mathbf{r}$ in the second term of Eq. (9), as sketched in Figure 2. Indeed, $\cos(\mathbf{q} \cdot \mathbf{r})$ is an oscillatory function that has, in the r -space, a period $2\pi/q$, having the nodes at $r_{\text{node}(n)} = [(2n+1)\pi/2]/q$. This means that, integrating along r the function $\rho(r) \cos(\mathbf{q} \cdot \mathbf{r})$, the integral receives a positive contribution in the $0 < r < (\pi/2)/q$. region and a negative contribution (that partially cancels the first one) in the $(\pi/2)/q < r < (3\pi/2)/q$. Positive and negative contributions alternate since we reach a region where r is sufficiently large to assure $\rho(r) \approx 0$; the integration process can be there stopped. This situation is represented in Figure 2 for an high Z atom, where the cut-off in r -space indicatively occurs at $r = 2$ Å. Reported values refer to an X-ray diffraction experiment performed with Cu $k\alpha$ radiation ($\lambda = 1.54$ Å). Increasing the scattering angle 2θ we progressively increase also the modulus of the scattering vector $q = 4\pi \sin\theta/\lambda$, see Eq. (3). Correspondently, the period $2\pi/q$ of the $\cos(\mathbf{q} \cdot \mathbf{r})$ function becomes progressively smaller, and the first node occurs at progressively shorter r values: $r_{1\text{node}} = (\pi/2)/q$. This means that $\cos(\mathbf{q} \cdot \mathbf{r})$ oscillates in r -space, more and more rapidly upon increasing q (or 2θ), as sketched in Figure 2, where red and blue segments represent r -regions where $\cos(\mathbf{q} \cdot \mathbf{r})$ assumes positive and negative values for the different scattering angles. The faster $\cos(\mathbf{q} \cdot \mathbf{r})$ oscillates, the more destructive are the interference in the integrals of Eq. (9), and the corresponding $f(q)$ value drops down for high q . This is the reason why in XRD the peaks intensity progressively drops down upon increasing the scattering vector q , see bottom right inset in Figure 2.

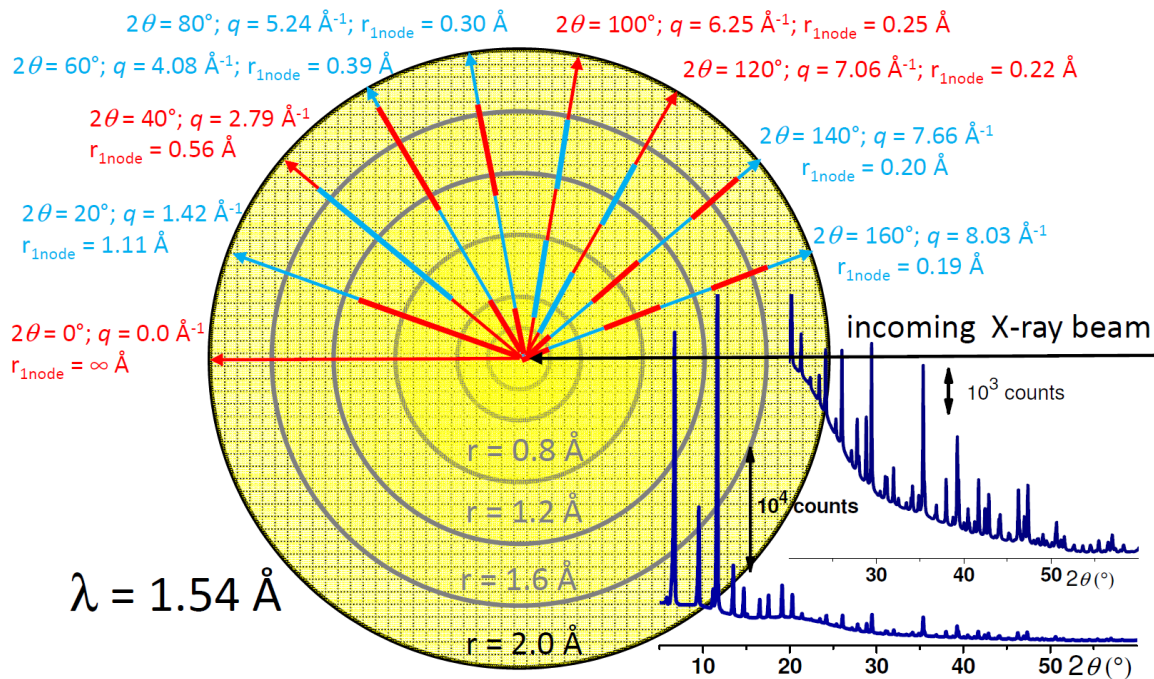


Figure 2. Main part: schematic representation of the electron density $\rho(r)$ of an high Z atom such as Hf or Ta. Concentric circles (drawn at $r = 0.2, 0.4, 0.8, 1.2, 1.6$ and 2.0 Å) represent regions of decreasing $\rho(r)$, supposing $\rho(r) \sim 0$ for $r > 2$ Å. The corresponding atomic form factor f is obtained integrating $\rho(r)$ modulated by the oscillatory function $\exp(-i \mathbf{q} \cdot \mathbf{r})$ in the spatial region $r \leq 2$ Å, see second term in Eq. (9). The black arrow represents the direction of the incoming X-ray beam: The colored arrows indicates the sign of $\text{Re}[\exp(-i \mathbf{q} \cdot \mathbf{r})] = \cos(\mathbf{q} \cdot \mathbf{r})$ along the designed scattering direction: red and blue colors represents positive and negative regions, respectively. A value $\lambda = 1.54$ Å is assumed to compute the nodes of $\cos(\mathbf{q} \cdot \mathbf{r})$. For each 2θ direction the first node occurs at $r_{1\text{node}} = (\pi/2)/q$. The intensity of the yellow color mimics the increased electron density $\rho(r)$ in proximity of the nucleus. Bottom right corner: typical XRPD pattern (desolvated HKUST-1 MOF collected with $\lambda = 1.54$ Å),¹⁹ showing the typical decrease of the Bragg peak intensity by increasing 2θ (increasing q). The insert reproduced a magnification of the high 2θ region of the same diffractogram. See Figure 3 for a direct representation of the atomic form factors f for a selection of atoms and ions. Unpublished figure.

Let us consider first the $f(q)$ function behavior at the lower scattering extreme of its domain, i.e. $q \rightarrow 0$ ($2\theta \rightarrow 0$). Here, the electronic cloud scatters the incident X-ray radiation perfectly in phase. $f(q = 0)$ is therefore equal to the total charge of the number of electrons of the atom (atomic number Z) or ion. Indeed, being $\cos(\mathbf{0} \cdot \mathbf{r}) = 1$, the second term of Eq. (9) simply becomes: $f(0) = \int \rho(\mathbf{r}) d\mathbf{r} = Ze^-$. Let us progressively increase the q value, e.g. assuming that the diffraction experiment is performed using Cu $K\alpha$ radiation ($\lambda = 1.54$ Å). At $2\theta = 20^\circ$, $q = 1.42$ Å⁻¹; at this q value the integral in Eq. (9) receives a positive contribution up to $r = 1.11$ Å, while in the 1.11-2.00 Å the contribution is negative. Prosecuting the analysis for higher scattering angles, it can be noticed that in the integration range $0 < r < 2$ Å the function $\cos(\mathbf{q} \cdot \mathbf{r})$ shows a number of nodes of: 0, 1, 2, for a scattering angle of $2\theta = 0, 20$ and 40° , respectively; a fourth node occurs at $2\theta = 100^\circ$ and a fifth is observed at $2\theta = 140^\circ$, see Figure 2.

Several quantum mechanical methods of increasing sophistication have been employed to evaluate the atomic electron density $\rho(r)$,²⁰⁻²⁵ that in turns allowed a better definition of the atomic form factors.²⁶⁻³¹ Tabulated values of $f(q)$ for all chemical elements and some relevant ions can be found in specialized literature.³² In particular, $f(q)$ is commonly expressed according to Eq. (10), hence using an approximated 9-parameter model function, introduced by Cromer and Mann.²⁸ This approach ensures a precision of 10^{-6} in the determination of the atomic form factors, and can be employed up to $q = 4\pi\sin\theta/\lambda \sim 25$ Å⁻¹ (i.e. up to $\sin\theta/\lambda \sim 2$ Å⁻¹). This q range is able to cover all

laboratory experiments. Indeed, at $2\theta = 160^\circ$, the q value reached with Cu ($\lambda = 1.54 \text{ \AA}$), Mo ($\lambda = 0.71 \text{ \AA}$) and Ag ($\lambda = 0.56 \text{ \AA}$) anodes is 8.03, 17.72 and 22.46 \AA^{-1} , respectively. The coefficients a_i , b_i and c for each chemical element are also tabulated.³²

$$f(q) = \int \rho(\mathbf{r}) \exp(-i\mathbf{q} \cdot \mathbf{r}) d\mathbf{r} \simeq \int \left[\sum_{i=1}^4 A_i e^{-B_i r^2} + c \delta(\mathbf{r}) \right] \exp(-i\mathbf{q} \cdot \mathbf{r}) d\mathbf{r} = \sum_{i=1}^4 a_i e^{-b_i q^2} + c \quad (10)$$

where $r = |\mathbf{r}|$ and $c + \sum a_i = Ze^-$. The excellent approximation (10) is based on the fact that the electron density can be well reproduced by the sum of different Gaussian functions of different standard deviation, defining the different closed shells of the orbitals: $\rho(\mathbf{r}) = \sum_i A_i \exp(-B_i r^2)$. The last equality in (10) holds because the Fourier transform of a Gaussian function is still a Gaussian:³³ $\text{FT}\{A_i \exp(-B_i r^2)\} = a_i \exp(-b_i q^2)$, where $a_i = (\pi/B_i)^{1/2} A_i$ and where $b_i = \pi^2/B_i$. For large Z atoms, the closest shells can be considered sufficiently sharp in r -space that the corresponding Gaussian can be approximated with a Dirac δ -function, which Fourier transform is constant and equal to unit in q -space.

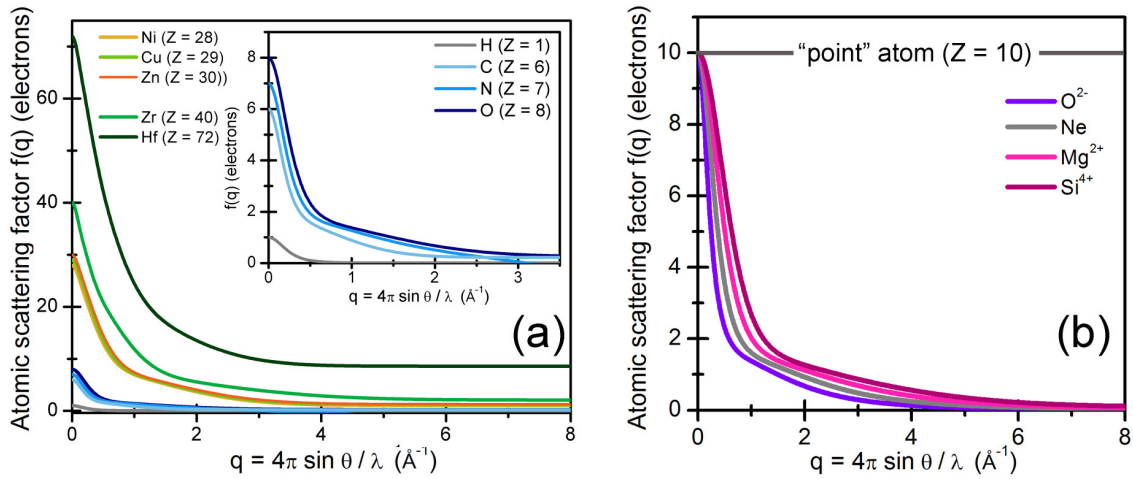


Figure 3. Part (a): $f(q)$ functions for three elements commonly present in MOFs linkers, i.e. H, C, N, and O (see also magnified detail in the inset), and for three elements which have been employed as metal centers in MOFs frameworks, i.e. Ni, Cu, Zn, Zr, Hf. . Part (b): $f(q)$ functions for three ions, iso-electronic to the Ne atom ($Z = 10$, also reported), i.e. the Mg^{2+} and Si^{4+} cations and the O^{2-} anion. The horizontal grey line $f(q) = 10 e^-$ highlights how a constant q -independent form factor would be obtained in correspondence of a $10e^-$ point charge. Unpublished figure.

Figure 3a shows the $f(q)$ plots computed using the third term of Eq. (10), for selected atoms and ions. As discussed above, $f_n(q=0) = 1, 6, 7, 8, 28, 29, 30, 40$ and $72 e^-$, for H, C, N, O, Ni, Cu, Zn, Zr and Hf atoms, respectively; i.e. $f_n(q=0) = Ze^-$. Although in the very low q -range $f(q)$ maintains values close to the Ze^- (this is true in the small angle regime, where $q < \sim 0.1 \text{ \AA}^{-1}$),³⁴ a steep decrease with increasing q is always observed for all atoms in the $0.2\text{--}2.0 \text{ \AA}^{-1}$ q region. The increasing phase differences between the waves scattered by unit volumes of electron density enhance the destructive interference phenomena (see Figure 2), rapidly driving $f(q)$ to $0 e^-$ for the light elements (see the H, C, N and O case in the inset of Figure 3a), where the c constant of Eq. (10) is null. This is not true for the high Z atoms, who exhibits a constant $f_n(q)$ slope in the whole $4 \text{ \AA}^{-1} < q < 8 \text{ \AA}^{-1}$ region, where: $f_{\text{Zr}}(q) \sim 2 e^-$ and $f_{\text{Hf}}(q) \sim 10 e^-$: this corresponds to the c constant in Eq. (10). This means that the first shell ($1s$ electrons) for Zr and the first 2 shells ($1s, 2s$ and $2p$ electrons) for Hf are confined in a r region enough small that, at $q = 8 \text{ \AA}^{-1}$, guarantees $qr \ll \pi/2$, i.e. $r \ll 0.2 \text{ \AA}$. Using the values reported by Clementi et al.²² for the radii of maximum charge density we can estimate the spatial extent of the different atomic orbitals. At $q = 8 \text{ \AA}^{-1}$, for zirconium, we obtain $r(1s, Z = 40) = 0.028 \text{ \AA}$ and $\cos(qr) = 0.975$, while for hafnium we have and $r(2s, Z = 72) = 0.077 \text{ \AA}$ and $\cos(qr) = 0.816$. These simple considerations qualitatively explain the values of the reported atomic form factors in Figure 3: $f_{\text{Zr}}(q = 8 \text{ \AA}^{-1}) = 2.07 e^-$ and $f_{\text{Hf}}(q = 8 \text{ \AA}^{-1}) = 8.58 e^-$. For

Zr(1s) $\cos(qr) \sim 1$ and the electrons belonging to the first shell behave as point charges and gives the same contribution to the $f_n(q)$ function in the investigated q domain (the residual $0.07 e^-$ represents the contribution of the 38 electrons occupying the higher shells). For Hf(2s) an higher deviation from the $\cos(qr) \sim 1$ case is observed, and the 8 electrons belonging to the 2s and 2p orbitals contribute only as $\sim 6.58 e^-$, i.e. they contribute at $\sim 82\%$ of their total charge ($2 e^-$ coming from the point charge Zr(1s) orbital).

Note that the rapid decrease of atomic form factors in the high- q range of all atoms is particularly critical when considering the fundamental role of high- q information, e.g. to improve the resolution in the reconstruction of the unit cell electron density (*vide infra*, Section 2.1.4.3).

The $f(q)$ plots reported in Figure 3a well evidences the cause of scarce X-rays are sensitivity to light atoms, primarily to H, and the reduced contrast between elements adjacent to each other. Here, $f(q)$ functions for three elements commonly present in MOFs linkers, i.e. C, N, and O (see also magnified detail in the inset of the same Figure), and some elements which have been employed as metal centers in MOFs frameworks, i.e. Ni, Cu, Zn, Zr, Hf, are reported. The Z-dependent difference in $f(q)$ values between the two groups of element is striking, and clearly demonstrate the difficulties in locating the lighter atoms of the organic linkers in the MOFs unit cells, and in distinguishing between almost iso-electronic elements such as C, N, O, or Ni, Cu, Zn, due to the high similarity between their $f(q)$ functions in the whole reported q -range.

In addition, Figure 3b reports the $f(q)$ plots for three ions, iso-electronic to the Ne atom, i.e. the Mg^{2+} and Si^{4+} cations and the O^{2-} anion: in all these cases, 10 electrons are involved in the scattering process. Indeed, it can be noticed how all the plotted $f(q)$ functions, for $q = 0$, are equal to $10 e^-$. However, a trend can be clearly recognized in the subsequent behavior of the different $f(q)$ functions, showing the role played by the r -dependence of $\rho(r)$. In particular, for the proposed cases, the decrease of $f(q)$ with q is progressively steeper considering in sequence Si^{4+} , Mg^{2+} , Ne, and O^{2-} . This behavior can be easily interpreted noticing that the phase shift in Eq. (9) is determined by the scalar product $\mathbf{q} \cdot \mathbf{r}$. Thus, the q -value and the number of involved electrons being equal, the form factor for a larger charge distribution dies out more rapidly. With respect to the reported examples, cations (Mg^{2+} and Si^{4+}) exhibit a smaller atomic radius with comparison to neutral atoms (Ne), due to the reduced shielding of the nuclear charge, and the consequent enhancement in nuclear attraction towards the remaining electrons. Similarly, a larger radius is found for negatively charged anions (O^{2-}).

Finally, it is worth noticing that, for some applications, the inelastic scattering of X-rays has to be accounted. Correspondingly, the definition of the atomic form factor is extended, including a complex anomalous scattering contribution $\Delta f(\lambda) = \Delta f'(\lambda) + i\Delta f''(\lambda)$.³⁵ The Δf contribution, dependent on the incident X-ray wavelength λ (or energy), is added to the atomic form factors f defined above, with its real and imaginary parts indicating a magnitude variation and a phase shift of the scattered wave, respectively. However, in most cases, anomalous scattering factors $\Delta f'$ and $\Delta f''$ are negligible with comparison to f , as can be noticed from tabulated numerical values.³²

2.1.3 Ordering levels and structural information level. The physical phenomena hitherto described and the related sets of equations have a general valence, and can be indistinctly applied to any kind of sample: gases, liquids, solids of amorphous or crystalline nature. In the case of crystalline materials (crystallography), the periodic long-range ordering arrangement of atoms inside the crystal lattice allows further elaboration of the general form in Eq. (8), leading for instance to Laue conditions.^{12,14,36} In such a case the elastic scattering process is commonly referred as diffraction, and the scattered intensity $I(\mathbf{q})$ is characterized by sharp, well-defined Bragg peaks. This case will be discussed in more details in the following Section 2.1.4.

When the ordering level of the investigated sample is lowered (single molecules in the gas or liquid phase or amorphous materials), the scattering signals are diffused in the entire q -space and, due to random molecular orientation, the 3D information is reduced to 1D, and can be extracted

from isotropic scattering patterns. The resulting Debye equation, and the commonly employed RDF formalism are discussed in Section 2.1.5.

A fundamental conceptual difference can be envisaged between the perfectly-ordered crystal case and systems characterized by a lower ordering level. As it will be detailed in Section 2.1.4, in a diffraction experiment, once the phases and amplitudes of hkl reflections (vide infra Eq. (12)) have been obtained, we can directly reconstruct the 3D electron density $\rho(\mathbf{r})$ from the experimental data set.

Conversely, such direct and univocal relation (*diffraction pattern* \leftrightarrow *3D structure*) is no longer valid for non-crystalline systems, due to lowering in information content. In this case, the data analysis strategy requires a conceptual inversion of the previous relation.³⁷ The relation changes into *hypothetical 3D structures* \rightarrow *simulated scattering patterns*. Best-fit of experimental 1D scattering curves then provides the most plausible 3D structure. These considerations emphasize the crucial role of theoretical modeling for the interpretation of scattering data from non-crystalline environments.

2.1.4 X-ray diffraction from perfect crystals

2.1.4.1 Laue equations. Let us focus the analysis on a perfect crystal, where the unit cell is periodically repeated in the three dimensions of the space. In particular, consider the simple case of a cubic lattice, including N_1 , N_2 and N_3 atoms in the three spatial dimensions, respectively. Here, the position \mathbf{r}_n of the n^{th} atom can be expressed in the form $\mathbf{r}_n = n_1\mathbf{a} + n_2\mathbf{b} + n_3\mathbf{c}$, with $(n_1; n_2; n_3)$ integer numbers and $(\mathbf{a}; \mathbf{b}; \mathbf{c})$ primitive vectors of the crystal lattice.

The periodic arrangement of atoms allow further elaboration of the term $|\sum_n \exp(-i\mathbf{q}\cdot\mathbf{r}_n)|^2$, appearing in Eq. (8). Substituting the expression of \mathbf{r}_n previously introduced, we obtain:

$$\sum_n \left| e^{-i\mathbf{q}\cdot\mathbf{r}_n} \right|^2 = \left| \sum_{n_1, n_2, n_3} e^{-i\mathbf{q}\cdot(n_1\mathbf{a} + n_2\mathbf{b} + n_3\mathbf{c})} \right|^2 = \left| \sum_{n_1=0}^{N_1-1} e^{-i\mathbf{q}\cdot(n_1\mathbf{a})} \right|^2 \cdot \left| \sum_{n_2=0}^{N_2-1} e^{-i\mathbf{q}\cdot(n_2\mathbf{b})} \right|^2 \cdot \left| \sum_{n_3=0}^{N_3-1} e^{-i\mathbf{q}\cdot(n_3\mathbf{c})} \right|^2 \quad (11)$$

If the system contains enough atoms and the wavelength of the incident X-ray beam is smaller enough with comparison to interatomic distances, it can be demonstrated that each of the factors of general form $|\sum_j e^{-i\mathbf{q}\cdot(j\mathbf{l})}|^2$ (with $j = n_1, n_2, n_3$ and $\mathbf{l} = \mathbf{a}, \mathbf{b}, \mathbf{c}$) in Eq. (11) is null unless scalar product $\mathbf{q}\cdot\mathbf{l}$ is equal to an integer multiple of 2π . Hence, the coherent scattered intensity is $\neq 0$ only along specific directions, i.e. particular values of \mathbf{q} , depending on atomic positions within the crystal. This condition on \mathbf{q} -values allowing constructive interference, and therefore observable scattered intensity, is expressed by the following Laue equations:³⁶

$$\mathbf{q} \cdot \mathbf{a} = h2\pi, \quad \mathbf{q} \cdot \mathbf{b} = k2\pi, \quad \mathbf{q} \cdot \mathbf{c} = l2\pi \quad (12)$$

where $(h; k; l)$ are integer numbers (also known as Miller indexes), allowed to vary in the $[-\infty, +\infty]$ range.

Laue equations can be read in several different ways, hereinafter summarized (further details and a more comprehensive mathematical description can be found in the specialized literature.^{14,38}

The Miller indexes $(h; k; l)$ appearing in Eq. (12) identify a family of parallel lattice planes, with inter-planar distance d_{hkl} . In particular, the indexes denote a plane that intercepts the three points \mathbf{a}/h , \mathbf{b}/k , and \mathbf{c}/l , or some multiple therein. Furthermore, a general solution that simultaneously verifies the Laue conditions can be expressed in the form:

$$\mathbf{q} = h\mathbf{a}^* + k\mathbf{b}^* + l\mathbf{c}^* = \mathbf{g} \quad (13)$$

where $(\mathbf{a}^*, \mathbf{b}^*, \mathbf{c}^*)$ define a new set of lattice vectors, related to the $(\mathbf{a}, \mathbf{b}, \mathbf{c})$ vectors by the following relations:

$$\mathbf{a}^* = 2\pi \frac{\mathbf{b} \wedge \mathbf{c}}{\mathbf{a} \cdot (\mathbf{b} \wedge \mathbf{c})}, \quad \mathbf{b}^* = 2\pi \frac{\mathbf{c} \wedge \mathbf{a}}{\mathbf{b} \cdot (\mathbf{c} \wedge \mathbf{a})}, \quad \mathbf{c}^* = 2\pi \frac{\mathbf{a} \wedge \mathbf{b}}{\mathbf{c} \cdot (\mathbf{a} \wedge \mathbf{b})} \quad (14)$$

This new lattice is referred to as reciprocal lattice. Each point in the reciprocal lattice corresponds to a set of lattice planes of index (hkl) in the direct lattice. Furthermore, the direction of each reciprocal lattice vector \mathbf{g} is normal to a family of real-space lattice planes, while its magnitude is proportional to the reciprocal of the interplanar spacing, i.e. $|\mathbf{g}| = 2\pi / d_{hkl}$. Laue conditions can be therefore reformulated in the implication: $I(\mathbf{q}) \neq 0 \leftrightarrow \mathbf{q} \equiv \mathbf{g}$, i.e. a non-zero diffracted intensity is measured only when the scattering vector \mathbf{q} coincides with a vector of the reciprocal lattice.

Finally, notice that the Laue conditions and the well-known Bragg law³⁹⁻⁴³ are just two different perspectives on the same physical phenomenon. Their equivalency can be easily demonstrated considering that:

(i) the general expression for the modulus of the scattering vector previously introduced, see Figure 1b and Eq. (3), is given by $|\mathbf{q}| = 4\pi\sin\theta/\lambda$;

(ii) the modulus of a generic reciprocal lattice vector is given by $|\mathbf{g}| = 2\pi/d_{hkl}$.

Then, starting from the above mentioned formulation of the Laue conditions $\mathbf{q} = \mathbf{g}$, the simple passages Eq. (15) reported below yield the Bragg law:³⁹

$$\mathbf{q} = \mathbf{g} \quad \rightarrow \quad |\mathbf{q}| = |\mathbf{g}| \quad \rightarrow \quad \frac{4\pi \sin \theta}{\lambda} = \frac{2\pi}{d_{hkl}} \quad \rightarrow \quad 2d_{hkl} \sin \theta = \lambda \quad (15)$$

2.1.4.2 The structure factor. The crystallographic unit cell is the smallest unit by which the periodic order in the crystal is repeated: once the structural information is obtained within the cell, it can be simply extended to the whole crystal by periodical replication. Consequently, hereinafter the analysis will focus on the atoms included in the unit cell.

In particular, let us introduce the so-called structure factor $F(\mathbf{q})$, defined as:

$$F(\mathbf{q}) = \sum_n f_n(q) e^{-i\mathbf{q} \cdot \mathbf{r}_n} \quad (16)$$

where $f_n(q)$ is the atomic form factor of the n -atom in the unit cell, see Eq. (7), and where the index n now runs over the atoms within the unit cell. Please note the huge difference between Eq. (16) and Eq. (8), where n was running over all the atoms of the sample! $F(\mathbf{q})$ includes all the effect of internal interference due to the geometric phase relationships between the atoms in the crystal unit cell, with each n^{th} atomic contribution weighted by its form factor $f_n(q)$.

Once the atomic form factors $f_n(q)$ for all the involved elements are known, the positions \mathbf{r}_n of the N atoms within the unit cell can be specified by their dimensionless fractional coordinates (x_n, y_n, z_n) , i.e. $\mathbf{r}_n = x_n\mathbf{a} + y_n\mathbf{b} + z_n\mathbf{c}$. When considering the case of detectable diffracted intensity, the Laue condition, Eq. (13), can be employed to simplify the $\mathbf{q} \cdot \mathbf{r}_n$ phase factor, as follows:

$$\mathbf{q} \cdot \mathbf{r}_n = (h\mathbf{a}^* + k\mathbf{b}^* + l\mathbf{c}^*) \cdot (x_n\mathbf{a} + y_n\mathbf{b} + z_n\mathbf{c}) = 2\pi (hx_n + ky_n + lz_n) \quad (17)$$

as, according to Eqs. (14), $\mathbf{a}^* \cdot \mathbf{a} = \mathbf{b}^* \cdot \mathbf{b} = \mathbf{c}^* \cdot \mathbf{c} = 2\pi$ and $\mathbf{a}^* \cdot \mathbf{b} = \mathbf{a}^* \cdot \mathbf{c} = \mathbf{b}^* \cdot \mathbf{c} = 0$. Substituting (17) in (16), the structure factor, now indexed using the Miller index (h, k, l) , can be consequently expressed as in Eq. (18), commonly referred to as the structure factor equation:

$$F_{h,k,l} = \sum_{n=1}^N f_n e^{-2\pi i(hx_n + ky_n + lz_n)} \quad (18)$$

Where the atomic scale factors f_n have to be computed for all atoms at the q value corresponding to the scattering conditions of the (h,k,l) plane: $q = 2\pi/d_{hkl}$, see Eq. (15). The square modulus of the structure factor is proportional to the intensity $I_{h,k,l}$ of the reflection measured in the diffraction pattern, corresponding to the Bragg condition being satisfied for the particular (hkl) plane:

$$I_{h,k,l} \propto |F_{h,k,l}|^2 \quad (19)$$

The use of the proportionality symbol instead of the simple equality in Eq. (19) is due the presence of other contributions to the reflection intensity, such as the Lorentz-polarization factor, the Debye-Waller factor, and the absorption factor, not discussed here for the sake of brevity. The same holds

for instrumental parameters such as incoming X-ray beam intensity and detector efficiency and angular acceptance. It is very important to notice that the structure factor $F_{h,k,l}$ is a complex quantity, which can be expressed in terms of amplitude and phase, as evidenced in Eq. (20), and graphically represented as a vector in the Argand plane:

$$F_{h,k,l} = |F_{h,k,l}|e^{i\phi(h,k,l)} = \sqrt{I_{h,k,l}}e^{i\phi(h,k,l)} \quad (20)$$

where $\phi(h, k, l)$ is the phase associated with the point in reciprocal space of coordinates (h, k, l) .

2.1.4.3 Inversion of the structure factor equation and electron density reconstruction. The end-task in diffraction crystallography is to get reliable information on the electron density function within the unit cell. For this purpose, using the Fourier relation between atomic form factor and atomic electron density, see Eq. (7), we can rewrite Eq. (18) as:

$$F_{h,k,l} = \int_{cell} \rho(x, y, z) e^{-2\pi i(hx+ky+lz)} dx dy dz \quad (21)$$

where $\rho(x,y,z)$ represents the electron density value in the point of coordinates (x, y, z) within the unit cell volume, where the integration is performed. Assume, for the moment, that the structure factor $F_{h,k,l}$ is fully determined, both in its amplitude and phase (this assumption is not fully correct, as will be discussed in Section 2.1.4.4, introducing the “phase problem”). It is hence possible to invert Eq.(21) as follows:

$$\rho(x, y, z) = \frac{1}{V} \sum_{h,k,l} F_{h,k,l} e^{2\pi i(hx+ky+lz)} \quad (22)$$

where V is the unit cell volume, assuring that both hands of Eq. (22) are measured in $e^- \text{ \AA}^{-3}$.

Due to the discrete nature of the structure factors set collected in a diffraction experiment (one structure factor $F_{h,k,l}$ for each experimentally determined and indexed hkl reflection, with a discrete ensemble of reflections), in Eq. (22) the integral is replaced by the sum over all the collected (h, k, l) values, i.e. a discrete Fourier Transform⁴⁴ is performed.

What we obtain is therefore a discrete approximation of the continuous electron density function. Consequently, the summation have to be performed on the finest possible grid of (x, y, z) points to obtain a smooth electron density distribution in the unit cell. Subsequently, connecting the points with equal electron density values, the typical wired grids are obtained (see Figure 4, white grids). The reconstructed electron density is then fitted to the effective atomic model (colored sticks in Figure 4), typically by least-squares minimization procedures.

Eqs. (21)-(22) highlight some fundamental issues, hereinafter briefly discussed. First, the “holistic” character of the diffraction technique, directly deriving from the Fourier relation between the scattering amplitude and spatial distribution of the scatterers, is evidenced. Indeed, to determine the electron density in an individual (x, y, z) point within the unit cell, the whole diffraction dataset, i.e. $F_{h,k,l}$ structure factors for all the measured reflections, is simultaneously employed. As a consequence, the achievable spatial resolution in the determination $\rho(x,y,z)$ is directly connected with the quality of the diffraction dataset employed, in terms of the number of structure factors used in the sum, and their degree of observability. In particular, the resolution level of an electron density map is commonly quantified using the minimum distance “visible” in the map, d_{min} , which can be simply deduced from Bragg's equation:

$$d_{min} = \frac{\lambda}{2 \sin \theta_{max}} = \frac{2\pi}{|q_{max}|} \quad (23)$$

where θ_{max} is the maximum angle at which a Bragg peak is detected above the noise level. Therefore, to improve the resolution level, we can either reduce the incident wavelength, or extend the collection of diffraction data up to the highest possible angles, i.e. collect data at higher q -values. Unfortunately, on the experimental ground, the steep decrease of atomic form factors (see Figure 3 in Section 2.1.2.) significantly lower the signal-to-noise ratio of diffraction data in the high-

q region, with respect to the low-q range. This means that high spatial resolution electron density maps can be obtained with a data collection strategy devoting much more acquisition time on the high q-part of the diffractograms in order to increase the statistics.

In addition, the reliability of the reconstructed electron density is also influenced by the precision in experimental determination of diffraction amplitudes (intensities) and, even more critically, by the correctness of the phasing process, that will be introduced in the next Section.

Finally, it is worth noticing that the minimum number of structure factors necessary to obtain a satisfactory reconstruction of the electron density depends on the structural complexity of the specific sample investigated. For macromolecules, and in particular for protein crystals, the available amount of experimental data is a crucial point. Furthermore, Figure 4 clearly evidences the crucial role played by the high q -region data collection in the ability of reconstructing the charge density via Eq. (22). From left to right we observe the $\rho(x,y,z)$ distributions reconstructed from data collected up to q_{\max} of 12.57, 4.89, 2.51 and 1.27 \AA^{-1} , respectively: the differences in the accuracy of the reconstructed charge densities are evident. MOFs, with unit cells volumes as large as some tens of thousands of \AA^3 indicatively containing up to 10^3 atoms, are among the more complex inorganic structures investigated via X-ray diffraction,^{45,46} and requires consequently high quality data collection in the high q -region. For this reason, neutron or synchrotron radiation data are welcome.⁴⁷⁻⁴⁹ Indeed synchrotron data are characterized by a much higher incident photon flux, while neutron scattering lengths are q -independent, vide infra Section 2.1.2.

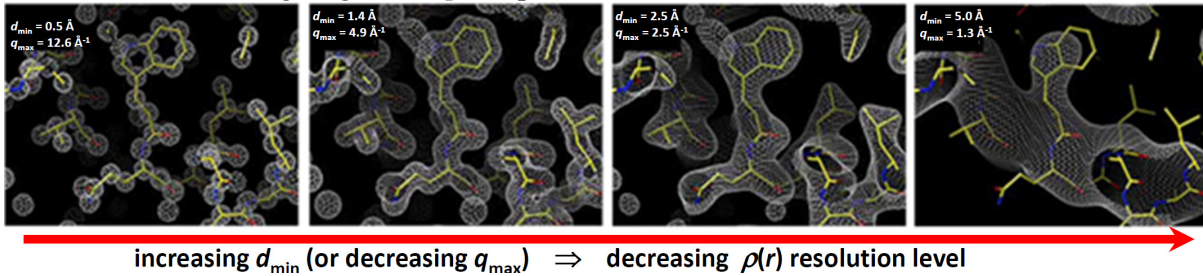


Figure 4. Effect of resolution level on electron density map. From left to right: "perfect" electron density maps calculated from the atomic model in correspondence of d_{\min} values increasing from 0.5 \AA to 5.0 \AA (the d_{\min} value is reported in white color in the top left corner of each map). The images are snapshot from a movie created by James Holton at the Advanced Light Source of the Berkeley Laboratory (California, US), that can be found on the web at the link: <http://ucxray.berkeley.edu/~jamesh/movies>. Notice that electron density maps reconstructed from experimental data likely will provide a worse fit to molecular model, and that the reported maps were calculated from an atomic model that lacked H atoms.

2.1.4.4 The phase problem. Eq. (22) can be rewritten explicitly expressing the complex nature of the structure factors, highlighted in Eq. (20). We therefore obtain:

$$\rho(x, y, z) = \frac{1}{V} \sum_{h,k,l} |F_{h,k,l}| e^{i\phi(h,k,l)} e^{2\pi i(hx+ky+lz)} \quad (24)$$

where only $|F_{h,k,l}| = (I_{h,k,l})^{1/2}$ can be obtained from the experiment. Assume now to have collected a complete set of diffraction data on a completely unknown crystal, to the best of experimental possibilities. An almost obvious question can be asked: does the diffraction data contain all the information to fully determine the structure of the crystal? Looking at Eq. (24), we can easily realize that a crucial piece of the puzzle is missing. The amplitude of the structure factor $|F_{h,k,l}|$ can be obtained simply calculating the square root of the intensity $I_{h,k,l}$, as expressed in Eq. (19). However, any information about the phase $\phi(h, k, l)$ is unavoidably lost. As depicted in Figure 5, this lack has dramatic implications, because the phases carry the most of information.

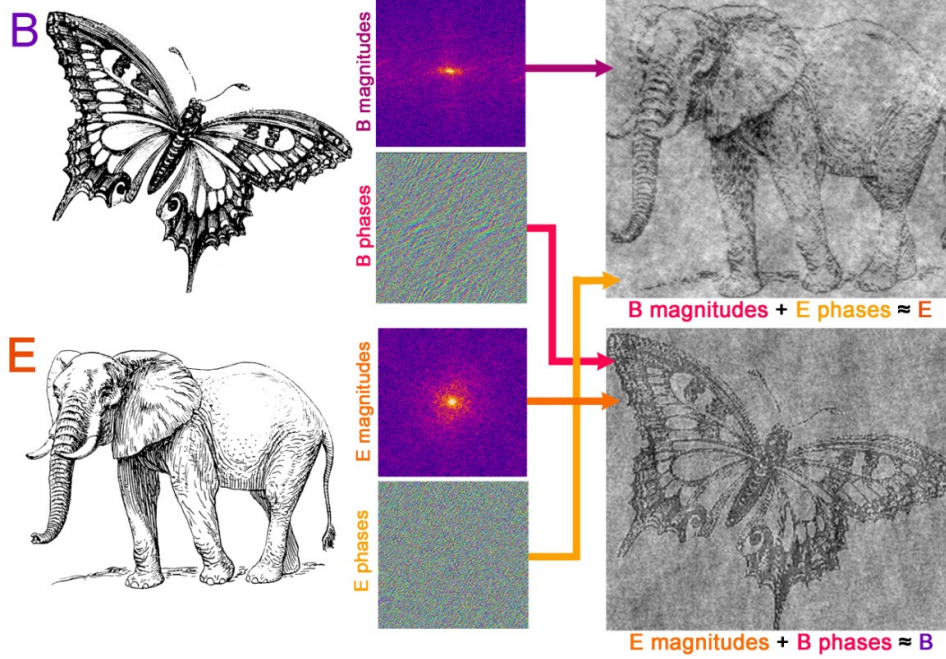


Figure 5. Visual representation of the phase problem. Left panel: pictures of a butterfly (B) and an elephant (E). These images can be treated as density maps and compute their Fourier transforms, obtaining for each picture the reported amplitudes and phases (middle panels). In right panel are reported the images obtained combining the B amplitudes and E phases (top panel) or, oppositely, E amplitudes and B phases (bottom panel). Comparing the two resulting pictures, it is striking that are the phases carry out the major part of the information. The pictures have been elaborated using the FTL-SE program.⁵⁰ Unpublished figure.

Notwithstanding this inherent limitation, in the most of cases the information contained in the diffraction dataset is enough to obtain a satisfactory level in electron density reconstruction. Indeed, several methods have been developed to determine the $\varphi(h, k, l)$ values, thus bypassing the phase problem. Among the commonest phasing approaches we can mention *ab initio* or direct methods,¹⁵ Patterson methods,⁵¹⁻⁵³ molecular replacement,^{53,54} anomalous dispersion-based methods,^{35,55-57} and charge flipping methods.⁵⁸ A detailed discussion of these methodologies is beside the scope of the present work, and can be found elsewhere in the specialized literature.⁵⁹⁻⁶¹

2.1.4.5 The effect of the crystal vibrations on the diffracted intensity. All the equations written so far in Sections 2.1.4.1-2.1.4.4 holds for ideally perfect crystals where atoms of the unit cell occupies defined \mathbf{r}_n positions that do not change with time, i.e. hold neglecting the phenomenon of thermal vibrations in solids. If one would be able to totally eliminate the thermal effects, the Bragg reflections would be uniformly sharp with no dependence on scattering angle to the distribution of intensities.⁶² Actually, even in the 0-Kelvin limit, atoms vibrates inside a lattice, so that the atomic position are no more time independent but can be represented as a time-dependent displacement $\mathbf{u}_n(t)$ around the atomic equilibrium positions \mathbf{r}_n used so far: $\mathbf{r}_n(t) = \mathbf{r}_n + \mathbf{u}_n(t)$. This fact leads to a modification of the definition of the structure factor $F(\mathbf{q})$, see Eq. (16), that takes into account the atomic displacements $\mathbf{u}_n(t)$. As the time dependence of $\mathbf{u}_n(t)$ is, by several order of magnitude, faster than the acquisition time of a standard diffraction experiment, then Eq. (16) still holds if we make a time averaging over the atomic positions:

$$F(\mathbf{q}) = \langle \sum_n f_n(q) e^{-i\mathbf{q}\cdot\mathbf{r}_n(t)} \rangle = \sum_n f_n(q) \langle e^{-i\mathbf{q}\cdot\mathbf{r}_n(t)} \rangle = \sum_n f_n(q) e^{-i\mathbf{q}\cdot\mathbf{r}_n} \langle e^{-i\mathbf{q}\cdot\mathbf{u}_n(t)} \rangle \quad (25)$$

where the symbol $\langle \dots \rangle$ indicates the time averaging and where $\langle \exp(-i\mathbf{q}\cdot\mathbf{r}_n) \rangle = \exp(-i\mathbf{q}\cdot\mathbf{r}_n)$, as \mathbf{r}_n are time independent. Now, developing up to the quadratic term of the Taylor series the exponential containing the atomic displacements, we obtain: $\langle \exp(-i\mathbf{q}\cdot\mathbf{u}_n(t)) \rangle \sim 1 - i\langle \mathbf{q}\cdot\mathbf{u}_n(t) \rangle - 1/2\langle [\mathbf{q}\cdot\mathbf{u}_n(t)]^2 \rangle =$

$1 - \frac{1}{2} \langle [\mathbf{q} \cdot \mathbf{u}_n(t)]^2 \rangle$ because $\langle \mathbf{q} \cdot \mathbf{u}_n(t) \rangle = 0$ since the atomic displacements are uncorrelated and random when averaged over a sufficient long time.^{38,62} Defining $\alpha_n(t)$ the angle between the vectors \mathbf{q} and $\mathbf{u}_n(t)$ we can rewrite the scalar product as follows: $\langle \exp(-i\mathbf{q} \cdot \mathbf{u}_n(t)) \rangle \sim 1 - \frac{1}{2} q^2 \cdot \langle u_n^2(t) \rangle \langle \cos^2[\alpha_n(t)] \rangle$. Defining the isotropic mean squared displacement of the n -th atom as $u_n^2 = \langle u_n(t) \rangle^2$ and being geometrical average of $\cos^2[\alpha_n(t)]$ over a sphere equal to $\frac{1}{3}$, we finally obtain: $\langle \exp(-i\mathbf{q} \cdot \mathbf{u}_n(t)) \rangle \sim 1 - \frac{1}{6} q^2 u_n^2 \sim \exp(-\frac{1}{6} q^2 u_n^2)$. Indeed, the mid member of the last equation corresponds with the first term of the Taylor series of the exponential in the third member. Consequently, Eq. (25) can be rewritten as:

$$F(\mathbf{q}) \simeq \sum_n f_n(q) e^{-i\mathbf{q} \cdot \mathbf{r}_n} e^{-\frac{1}{6} q^2 u_n^2} = \sum_n f_n(q) e^{-i\mathbf{q} \cdot \mathbf{r}_n} e^{-W_n} \quad (26)$$

where the last exponential is a damping factor that further reduces the scattering amplitudes in the high q (or high $\sin(\theta)/\lambda$) part of the diffraction patterns. Figure 6a reports pictorially a 1D-representation of the effect that the thermal motion has on the spread of the atomic electron density. The atomic motion is usually defined using the Debye-Waller factor⁶²⁻⁶⁴ $W_n = 1/6 q^2 u_n^2$ or using the isotropic temperature factor $B_n = 8\pi^2 u_n^2$. According to the different conventions, the exponential that accounts for the dumping of the diffracted intensities due to the thermal motion of the atoms can be written as $\exp(-q^2 u_n^2/6)$ or as $\exp(-2W_n)$ or as $\exp[-\frac{1}{3} B_n \sin^2(\theta)/\lambda^2]$. According to Eq. (26), the measured intensity $I(\mathbf{q})$ can be expressed by:

$$I(\mathbf{q}) = |F(\mathbf{q})|^2 \simeq \sum_n f_n^2(q) |e^{-i\mathbf{q} \cdot \mathbf{r}_n}|^2 e^{-2W_n} \quad (27)$$

where each n -th term of the sum is damped by a factor $\exp(-2W_n)$. On the experimental ground, to limit the dumping effect described so far, low temperature data collections are welcome, in order to keep mean squared displacement u_n^2 of the atoms as low as possible.

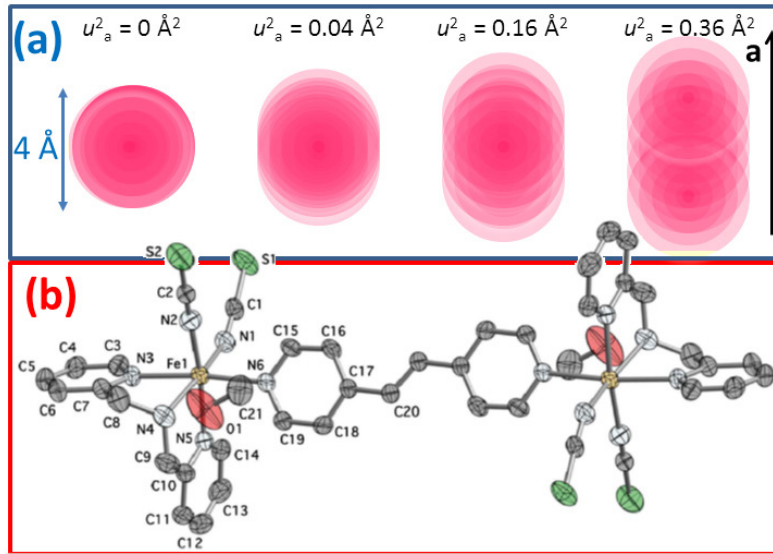


Figure 6. Part (a): pictorial representation on how the atomic displacement is able to spread the electron density in space. The same atom used in Figure 2, having the appreciable atomic electron density confined within a sphere of radius 2 \AA , is here represented assuming a mean squared displacement u_a^2 of, from left to right, 0, 0.04, 0.16 and 0.36 \AA^2 , respectively. For simplicity, only the atomic displacement along the a axis is here represented, assuming $u_b^2 = u_c^2 = 0 \text{ \AA}^2$. From what has been discussed in Sections 2.1.2 and 2.1.4.5, it is evident that the larger is the electron density spread, the larger will be the dumping of the scattered intensity at high q values. Part (b): molecular structure of $[\{\text{Fe}(\text{dpia})(\text{NCS})_2\}_2(\text{bpe})] \cdot 2\text{CH}_3\text{OH}$ MOF at 290 K where the thermal ellipsoids obtained after a structural refinement are reported (H atoms are omitted for clarity). Ellipsoids enclose 30% probability. From the refined structure it emerges how the atoms S1, S2 and O1 exhibits quite anisotropic displacement parameters. Reproduced with permission from Matouzenko et al.,⁶⁶ copyright (2011) Royal Society of Chemistry.

In the simplified discussion followed in this section we supposed that all atoms undergone an isotropic displacement along the three directions \mathbf{a} , \mathbf{b} and \mathbf{c} ; this allowed us to write $\langle \mathbf{q} \cdot \mathbf{u}_n(t) \rangle = \frac{1}{3} q^2 u_n^2$. Actually, the different strength of the chemical bonds around atom n can result in different atomic displacements along the three independent directions. An ellipsoid is a convenient way of visualizing the anisotropic vibration of atoms inside a lattice and therefore its 3D time-averaged position. We so speak about *thermal ellipsoids*, more formally termed *atomic displacement parameters* (adp), that are ellipsoids used to indicate the magnitudes and directions of the thermal vibration of the different atoms in the unit cell. Thermal ellipsoids are actually tensors (i.e. mathematical objects which allow the definition of magnitude and orientation of vibration with respect to three mutually independent axes). The three principal axes of the thermal vibration of an atom n are denoted $u_{n,a}^2$, $u_{n,b}^2$ and $u_{n,c}^2$, and the corresponding thermal ellipsoid is based on these axes. The size of the ellipsoid is scaled so that it occupies the space in which there is a particular probability of finding the electron density of the atom.⁶⁵ An example of structure reporting the refined thermal ellipsoid is reported in Figure 6b. The reconstruction, for all atoms in the unit cell of the thermal ellipsoids requires a very high quality data set. In most of the cases only isotropic thermal factors can be independently refined.

Finally, please note that, as the measured scattered intensity, $I(\mathbf{q})$, is the squared modulus of the structure factor $F(\mathbf{q})$, see Eq. (8), then the thermal motion affect the measured intensity according to the following law: $I(\mathbf{q}) = I_0(\mathbf{q}) \exp(-\frac{1}{3} q^2 u^2)$, where $I_0(\mathbf{q})$ is the expected intensity in case of ideal crystal characterized by non-vibrating atoms.

2.1.5 X-ray scattering from non-crystalline samples. In non-crystalline samples (gases, liquids, and amorphous materials), where only short range ordering is present, the probed volume is constituted by a statistical ensemble of sub-systems (molecules) randomly oriented. We can start from the general form in Eq. (8) and explicitly express the square modulus operation (that for a generic complex number z is given by $|z|^2 = z z^*$, $z \in \mathbf{C}$), according to the passages reported below:

$$\begin{aligned} I(\mathbf{q}) &= \left| \sum_n f_n(q) \exp(-i\mathbf{q} \cdot \mathbf{r}_n) \right|^2 = \\ &= \left[\sum_n f_n(q) \exp(-i\mathbf{q} \cdot \mathbf{r}_n) \right] \left[\sum_m f_m(q) \exp(i\mathbf{q} \cdot \mathbf{r}_m) \right] = \quad (28) \\ &= \sum_n \sum_m f_n(q) f_m(q) \exp(-i\mathbf{q} \cdot (\mathbf{r}_n - \mathbf{r}_m)) \end{aligned}$$

We are therefore allowed to isotropically average on all possible orientations the resulting form,^{13,14,67} obtaining a greatly simplified formula in which the scattered intensity is expressed as a function of one instead of three spatial dimensions. The resulting form, eq. (29), is named Debye equation:⁶⁸

$$I(q) = \sum_n \sum_m f_n(q) f_m(q) \frac{\sin(qr_{nm})}{qr_{nm}} \quad (29)$$

where r_{nm} is the distance between n^{th} and m^{th} atom.

The Debye equation represents the key theoretical instrument in interpreting results from X-ray scattering experiments involving non-crystalline samples. However, the direct use of Eq. (29) is associated with some critical issues, in particular passing from gas-phase scattering to experiments involving solution-phase or solid non-crystalline systems. Indeed, when dealing with many-atoms systems (more than 500 atoms), calculation using Debye equation is extremely resource-consuming, due to the extremely high number of possible combinations of n and m indexes.

For these reasons, it is useful to express the Debye formula in terms of radial distribution functions (RDF) $g_{nm}(r)$.⁶⁹⁻⁷¹ RDF are defined in such a way that the probability of finding a m -type atom at distance r from an n -type atom is equal to $4\pi r^2 g_{nm}(r)$ (in Figure 7 is reported a schematic representation of how RDF are obtained).

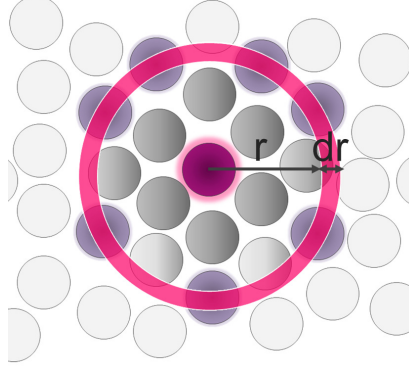


Figure 7. Scheme of the radial distribution function (RDF) $g(r)$. The RDF is a measure to determine the correlation between particles within a system. Specifically, it is an average measure of the probability of finding a particle at a distance of r away from a given reference particle. The general algorithm involves the determination of the number of particles within r and $r+dr$ (circular yellow shell in the figure) from the reference particle (represented in violet).

Using the formalism of RDF, Eq. (29) can be reformulated as in Eq. (30):¹⁴

$$I(q) = \sum_n N_n^2 f_n^2(q) + \sum_m \sum_{n \neq m} \frac{N_n N_m}{V} f_n(q) f_m(q) \cdot \int_0^\infty (g_{nm}(r) - 1) \frac{\sin(qr)}{qr} 4\pi r^2 dr \quad (30)$$

where the indexes n and m run over all the atoms types included in the sample, N_n and N_m are the numbers of n -type and m -type atoms respectively and V the volume of the sample probed by X-rays.

In the case of gas-phase scattering, the RDF $g_{nm}(r)$ can be approximated to a Dirac delta function and consequently Eq. (30) reduces again to Eq. (29). Eq. (30) highlights the possibility of obtaining a simulated $I(q)$ curve directly using the $g_{nm}(r)$ functions for the system of interest, to be used for comparison with the measured scattering data. This, hence, represents the theoretical basis for modeling and interpretation of scattering experiments, providing a direct connection between acquired scattered intensity and structural features of the sample. More sophisticated analysis approaches will be then applied depending on sample peculiarities and the specific experimental conditions. In particular, depending on the investigated angular range, the SAXS (Small Angle X-ray Scattering)^{34,72,73} and WAXS (Wide Angle X-ray Scattering)¹⁴ techniques can be distinguished, providing structural information of different nature, and on different length-scales. At the highest q -exchanged values we have the total scattering or Pair Distribution Function (PDF) approach,⁷⁴ that will be discussed in more details in Section 4, once the basic concepts of EXAFS have been introduced in Section 3, while relevant examples in MOFs characterization will be reported in Section 5.5. For space limitation, the SAXS theory will not be discussed, consequently no example on the use of SAXS in MOFs characterization will be reported in Section 5. We will here just quote some relevant papers on this subject.⁷⁵⁻⁸⁰

2.2. Neutron diffraction

2.2.1. Historical background. In his PhD thesis of 1924, de Broglie assigned to any massive particle a wavelength λ given by the ratio between the Plank constant ($h = 6.626068 \times 10^{-34}$ Js) and its momentum $p = mv$:⁸¹

$$\lambda = h/p = h/[mv\sqrt{(1 - v^2/c^2)}] \sim h/(mv) \quad \text{for } v/c \ll 1 \quad (31)$$

successively named as de Broglie's wavelength. The de Broglie's intuition opened the possibility to perform diffraction experiments using as incident beam, instead of X-rays, any kind of particle beam of defined momentum \mathbf{p} having a modulus p in the order of 7×10^{-24} kg m s⁻¹, so that the corresponding λ will be in the range of 1 Å. This value is obtained for neutrons having a speed of about 4000 m/s, and for electrons moving at two percent of the light speed c , see Table 1, so that relativistic corrections are useless for neutrons and in first approximation negligible for electrons.⁸²

Table 1. Rest mass (m , both in kg and in mc^2 units), charge (q) and spin (s) for electrons and neutrons, that represent the two most used particle beams for diffraction experiments. The last column report the particle speed (v , both in m/s and in c units: $c = 2.9979 \times 10^8$ m/s) and the particle energy (E) for particles having a de Broglie wavelength of $\lambda = 1$ Å. For comparison, the last row reports the corresponding values for a photon of the same wavelength, see Eq. (1).

Particle	m (kg)	mc^2 (MeV)	q (C)	s (\hbar)	Values for $\lambda = 1$ Å			
					v (m/s)	v/c	E (eV)	p (kg m s ⁻¹)
electron	9.1094×10^{-31}	0.511	1.6022×10^{-19}	1/2	7.2739×10^6	2.4263×10^{-2}	150.412	6.626×10^{-24}
neutron	1.6749×10^{-27}	939.565	0	1/2	3.9560×10^3	1.3196×10^{-5}	8.180×10^{-2}	6.626×10^{-24}
X-rays photon	0	0	0	1	2.9979×10^8	1	12398.4×10^{-4}	6.626×10^{-24}

As the technology needed to produce X-ray tubes was already available since some years,⁸³ electron sources of sufficient intensity became available in the twenties. The natural particle candidate to experimentally test de Broglie's theory was therefore the electron. The experimental proof of the de Broglie's idea, providing a remarkable validation of the particle-wave dualism, arrived in 1927 by Davisson and Germer. The scientists, at Bell Telephone laboratories, obtained an electron diffraction pattern from a thin Ni single crystal.⁸⁴ Independently at the University of Aberdeen, Thomson and Reid passed a beam of electrons first through a thin celluloid⁸⁵ film and subsequently through a thin Pt⁸⁶ film. In both laboratories diffraction patterns explainable combining the Bragg equation with the de Broglie assumption were detected. Several other observations followed these pioneering works,⁸⁷⁻⁸⁹ and some historical perspectives are available in the literature.^{90,91}

The use of neutrons, discovered by Chadwick in 1932,⁹²⁻⁹⁴ in diffraction experiments was postponed till the first nuclear reactors were available.⁹⁵ The first neutron diffraction experiments were carried out in the second half of the forties by Wollan and Shull, using the Graphite Reactor at Oak Ridge,⁹⁶⁻¹⁰³ and by Fermi and Marshall, using the heavy water pile at the Argonne National Laboratory.^{104-106 107}

In the following electron diffraction will not be discussed anymore. This choice is related to the difficulties in collecting electron diffraction patterns on non damaged MOF crystals.¹⁰⁸ The main problem is the pronounced instability of MOFs under the electron beam, leading to loss of long range order information after mere seconds of illumination by the electron beam. Particularly experimental set up such as cryogenic sample holder stages and very low electron illumination conditions are mandatory to hope to obtain significant results.^{109,110} It is so not surprising to realize that the literature contains very few contributions where electron scattering in Transmission Electron Microscope (TEM) instruments has been used to characterize MOFs structures¹⁰⁸⁻¹¹⁵

2.1.2. Analogies and differences between neutrons and X-ray scattering. Although electron, neutron, and X-ray scattering interactions with matter are based on different physical processes, the resulting diffraction patterns are analyzed using the same coherent scattering approach described above for X-rays.^{116,117} Basically, once the concept of de Broglie wavelength (29) is established, Bragg equation can be rewritten as:

$$2d_{hkl} \sin(\theta) = h/(mv) \quad (32)$$

and applied to describe experiments performed with electrons or neutrons, as Eq. (15) is used for X-rays.

Neutrons interacts with the nuclei, i.e. with objects having a size of few fm ($1 \text{ fm} = 10^{-5} \text{ \AA}$). This implies that the nuclei with the same number of protons but with a different number of neutrons (isotopes) will behave as two completely different scattering objects in neutron diffraction: this was not true for X-rays where the scattering comes from the electrons. The interaction with nuclei implies that, in Eq. (9), both $\exp(-\mathbf{q}\cdot\mathbf{r})$ and $\cos(\mathbf{q}\cdot\mathbf{r})$ can be considered as ~ 1 , for any q value practically attainable in diffraction experiments (even those where the data collection is extended at very high angles, employing a very short λ at synchrotron sources). Consider now a nucleus with $r = 2 \text{ fm}$, at $q = 50 \text{ \AA}^{-1}$. In this case $qr = 10^{-3}$ and $\cos(qr)$ differs from units at the nine decimal digit only. This implies that the neutron scattering intensity is constant at any θ (or q) and does not drop off at high θ (or q) values as occurs for the X-ray scattering, see Figure 2 and related discussion. Neutron diffraction is consequently intrinsically superior to XRD in the collection of high quality data at high q , which is a key advantage in the structure refinement of complex structures like MOFs, see Section 2.1.4.3. This superiority is clearly visible in Figure 8a, where the simulated neutron diffraction pattern of desolvated UiO-66 is compared with the corresponding simulated XRPD pattern. *Vide infra* in the examples section Figure 18ab for a comparison between experimental neutron and X-ray diffraction patterns of $\text{Cr}_3(\text{BTC})_2$ MOF.

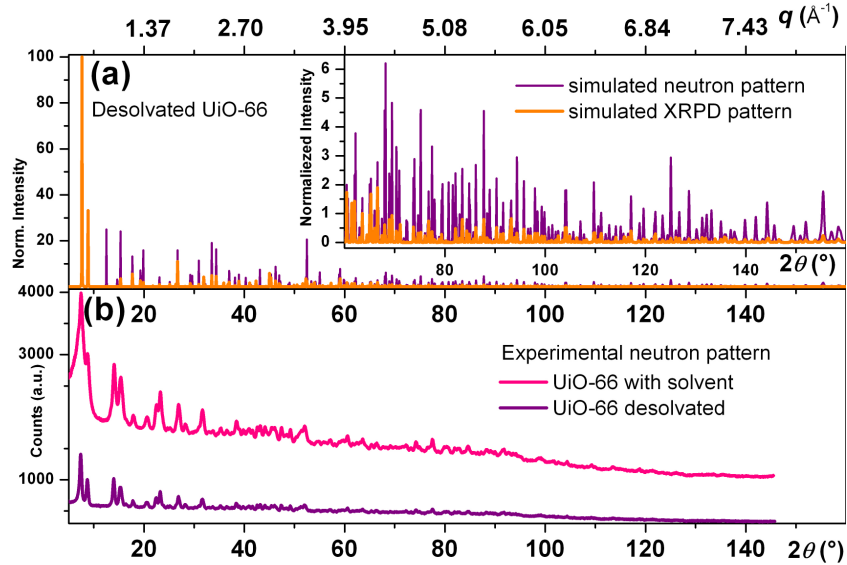


Figure 8. Part (a): comparison between the simulation of the X-ray (orange) and neutron (violet) diffraction patterns for UiO-66 MOF in its desolvated form ($\lambda = 1.954 \text{ \AA}$). Unpublished figure, by courtesy of A. Piovano (ILL, Grenoble F). Part (b): experimental neutron diffraction patterns of UiO-66 MOF before (pink curve, collected at 300 K) and after (violet curve, collected at 523 K) solvent removal. Unpublished data collected at Super-D2B instrument (ILL, Grenoble F) with $\lambda = 1.59 \text{ \AA}$: by courtesy of M. Ceretti (University of Montpellier-2, F).

The nuclear scattering intensity for neutrons is quantified by the total absorption cross section σ_{tot} , defined as the total number of neutrons scattered per second, normalized by the incident neutron flux Φ . As Φ is given by the number of incident neutrons per second per surface area, σ_{tot} is an area, usually measured in barn ($1 \text{ barn} = 1 \times 10^{-28} \text{ m}^2 = 100 \text{ fm}^2$, that approximately represents the geometrical cross sectional area of a uranium nucleus). The nuclear scattering intensity for neutrons can be alternatively quantified with the corresponding nuclear scattering length b , defined as the radius of an ideal hard sphere able to provide the same scattering. b is consequently related to σ_{tot} by the simple geometric relationship:

$$\sigma_{\text{tot}} = 4\pi \langle |b|^2 \rangle \quad (33)$$

where 4π comes from the integration over the whole solid angle Ω and where the “ $\langle \rangle$ ” symbol represents the statistical average over the neutron and nucleus spins. Indeed it has been demonstrated since the earliest studies of Fermi that the neutron-nucleus interaction is spin dependent.¹⁰⁷ Defining \mathbf{s} and \mathbf{I} the neutron and the nucleus spin, respectively, the b parameter can be defined as:¹¹⁸

$$b = b_c + 2 b_i [I(I+1)]^{-1/2} \mathbf{s} \cdot \mathbf{I} \quad (34)$$

where b_c and b_i are the coherent and incoherent neutron scattering lengths of the nucleus, respectively. On this basis, the total cross section σ_{tot} is given by the contribution of a coherent (σ_c) and an incoherent (σ_i) cross section:¹¹⁸

$$\sigma_{\text{tot}} = \sigma_c + \sigma_i \quad \text{where } \sigma_c = 4\pi |b_c|^2 \text{ and } \sigma_i = 4\pi |b_i|^2 \quad (35)$$

The coherent scattering depends on the scattering vector \mathbf{q} , and contains the structural information. The incoherent scattering is isotropic and, in a diffraction experiment, contributes to an overall increase of the background. Samples prepared with isotopic substitutions can be used to minimize σ_i and consequently increase the quality of the neutron diffraction data. In this regard, the most relevant case concern the hydrogen atom where for ^1H we have $b_c = -3.74$ fm and $b_i = 25.27$ fm, while for ^2H we have $b_c = 6.67$ fm and $b_i = 4.04$ fm. The synthesis of MOFs with deuterated ligands will consequently significantly decrease the neutron incoherent scattering.¹¹⁹ This effect is clearly visible in the experimental neutron diffraction data reported in Figure 8b where, the removal of the solvent inside the UiO-66 pores, causes a decrease of the scattering background by a factor larger than three. Indeed the solvent molecule, dimethylformamide (DMF), has seven hydrogen atoms ($\text{CH}_3)_2\text{NC(O)H}$ so that they are the major responsible for the incoherent neutron scattering of the solvated material. The patterns reported in Figure 8b are further informative because they show a clear decrease of the Bragg peak intensities at high 2θ moving from the solvated to the desolvated form of UiO-66. This is due to the thermal vibrations of the lattice. Indeed, the solvated UiO-66 has been measured at 300 K, while the data collection of the desolvated form has been performed at 523 K. This experimental result shows how, according to Eq. (26), the atomic thermal motion introduces a q -dependence on the scattering amplitudes also for neutron scattering. Indeed, the q -independence of the neutron scattering length is based on the point-dimension of the nuclei (few fm), but the atomic thermal motion moves the atoms (and so the nuclei) by fractions of Å, see Figure 6a. In other words, the nuclear density is a Dirac-delta function only in ideal lattices where vibrations are absent. In real lattices the nuclear density is actually spread because of the atomic vibration. On an experimental ground, this spread can be significantly reduced by adopting cryogenic sample environments.

Both b_c and b_i are defined by nuclear interaction, that can not be quantified by theory, so they must be determined experimentally.¹¹⁸ As shown in Figure 9, b_c has no specific dependence with Z , as was the case of the atomic scattering factor for X-rays (see Figure 3). This implies that for atoms having similar Z values, we can find isotopes having consistently different b_c values. As a consequence, neutron diffraction experiments can easily discriminate them. Analogously, light elements, that very weakly contribute to the overall X-ray scattering signal, may have $|b_c|$ values comparable to some high- Z elements, or even higher. Therefore a neutrons-based analysis multiplies the chances to locate low- Z elements with respect to the X-ray case.

Care must be done when comparing the results obtained with X-rays or neutron data collections because the former provides the electron density, while the latter provides the nuclear density. It is so common that the O–H (or C–H) distances refined from X-ray are markedly shorter than those refined from neutron data on the same compound. This is due to the fact that neutron scattering provides the correct nuclear-nuclear distance, while XRD observe that the electron cloud along the O–H (or C–H) bond is localized closer to the O (or C) atom, owing to its higher electronegative character. As an example, for the sucrose molecule ($\text{C}_{12}\text{H}_{22}\text{O}_{11}$), crystallizing with two molecules per cell in the monoclinic space group $P2_1$, the refined O–H (O–H) distance determined by X-rays is 0.79 Å (0.96 Å), while that determined by neutrons is 0.97 Å (1.095 Å).¹²⁰

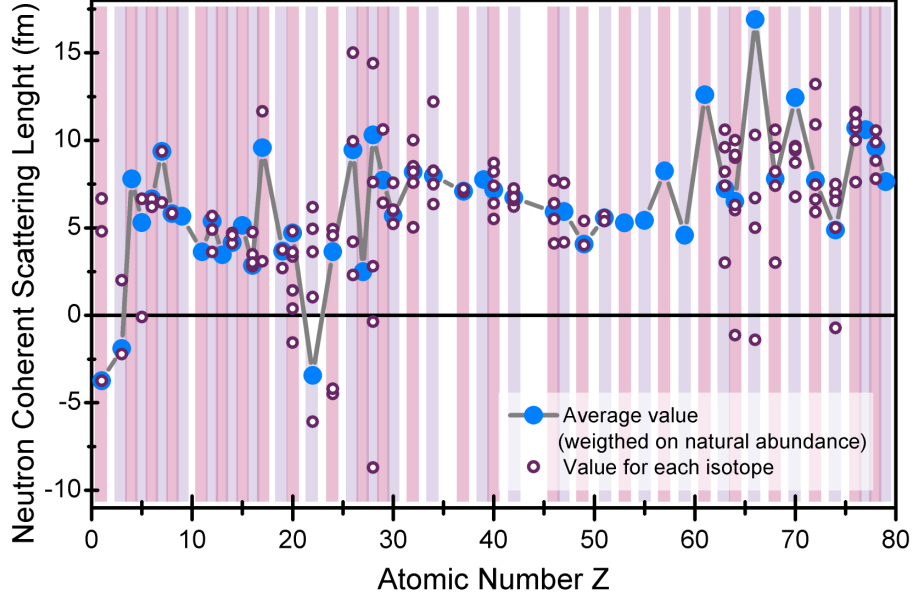


Figure 9. Selection of coherent neutron scattering lengths b_c as a function of Z . For each selected element, the full cyan spheres refer to the average value weighted on the natural isotopes abundance, while the violet circles refer to the specific isotopes. Unpublished figure, reporting values from the tables of Sears;¹¹⁸ the same data are also available on line on the NIST web site (<http://www.ncnr.nist.gov/resources/n-lengths/>).

As reported in Table 1, there are six orders of magnitude in energy between a neutron and an X-ray with $\lambda = 1 \text{ \AA}$. This means that the energy release of a neutron beam on the sample is negligible with respect to that occurring using an X-ray beam, particularly when a synchrotron source is used. This aspect guarantees that there is no risk of radiation damage on the sample for relatively short acquisitions. Conversely the sample can become radioactive after exposure to a neutron beam, a risk not present with X-rays. In such cases the samples can be not available for additional experiments for a while. Additional critical aspects of neutron diffraction concern the low neutron cross section and the low flux of neutron sources, forcing the scientists to synthesize huge amount of sample and requiring long data collections. Moreover, on one hand it is particularly difficult to obtain highly monochromatic neutron beams and on the other hand the $\Delta\theta$ accuracy of the detector is larger with respect to the X-ray diffraction case. Note that, for the same instrument, the $\Delta\theta$ accuracy is λ -dependent. As consequence, as it can be noticed differentiating the Bragg law see Eq.(15), we obtain:

$$\Delta d_{hkl} = \left| \frac{\partial d_{hkl}}{\partial \lambda} \right| \Delta \lambda + \left| \frac{\partial d_{hkl}}{\partial \theta} \right| \Delta \theta = \frac{1}{2 \sin(\theta)} \Delta \lambda + \frac{\lambda \cos(\theta)}{2 \sin^2(\theta)} \Delta \theta \quad (36)$$

The larger dispersion in the wavelength selected by the monochromator ($\Delta\lambda$) and a poorer $\Delta\theta$ resolution induces a larger incertitude on the lattice inter-planar distance determination. Typical values of $\Delta d/d$ obtained at neutron diffractometer are in the 10^{-2} – 10^{-3} range. This problem can be significantly overcome with a sophisticated combination of movable multi-detector, see e.g. the Super-D2B two axis instrument at ILL reactor (able to reach $\Delta d/d \sim 5 \times 10^{-4}$).¹²¹ Alternatively, the polychromatic time-of-flight (TOF) detection mode¹²² can be employed, see e.g. the HRPD instrument at the ISIS spallation neutron source able to reach $\Delta d/d \sim 4 \times 10^{-4}$.¹²³ These values are to be compared with what's available with X-rays at synchrotron sources: $\Delta\theta = 10^{-3}$ and $\Delta E/E = 5 \times 10^{-5}$ at 10 keV corresponding to $\lambda = 1.24 \text{ \AA}$, see Eq. (1).^{124,125}

The TOF approach is based to the fact that neutrons with different λ are traveling at different velocities, so that they will reach the sample (first) and the detector (then) at different times.

Working at fixed 2θ angle, with a small $\Delta\theta$ angular acceptance, the d_{hkl} can be obtained measuring the time (t_{TOF}) needed to travel the source-to-detector distance (S), according to the Bragg equation:

$$d_{hkl} = \frac{1}{2 \sin(\theta)} \frac{h}{mv} = \frac{1}{2 \sin(\theta)} \frac{ht_{TOF}}{mS} \quad (37)$$

where the neutron wavelength has been expressed using the de Broglie equation, see Eq. (32). Differentiating Eq. (37) with respect to the angular acceptance and the time resolution of the detector, we obtain:

$$\Delta d_{hkl} = \left| \frac{\partial d_{hkl}}{\partial \theta} \right| \Delta \theta + \left| \frac{\partial d_{hkl}}{\partial t_{TOF}} \right| \Delta t_{TOF} = \frac{\cos(\theta)}{2 \sin^2(\theta)} \frac{ht_{TOF}}{mS} \Delta \theta + \frac{1}{2 \sin(\theta)} \frac{h}{mS} \Delta t_{TOF} \quad (38)$$

It is evident from Eq. (38) that Δd_{hkl} can be minimized using large S distances. Moreover, a TOF-instrument does not need a monochromator, therefore it exploits the whole λ -spectrum emitted by a pulsed source, with an evident benefit on the total flux. In order to cover a larger d -spacing interval, defined by the acquisition time window between two successive neutron bunches, more than one detector bank can be used at different 2θ . The HRPD instrument at ISIS, for instance, is equipped with two detector banks at $2\theta = 90^\circ$ and 168° .¹²³

Finally, the limited access of neutron sources represents an additional practical problem. Table 2 summarized, in a schematic way, the main properties, advantages and disadvantages of diffraction experiments performed with X-ray or neutron beams.

Table 2. Summary of the main properties, advantages and disadvantages of diffraction experiments performed with X-ray or neutron beams. RA = rotating anode; BM = bending magnet; U = undulator.

Property	X-rays	neutrons
Interacts mainly with	all electrons	nuclei and unpaired electrons
Scattering intensity	decreases at high q values	constant at all q values
Beam penetration depth (m)	10^{-1} – 10^{-3} for $1 < Z < 10$; 10^{-3} – 10^{-5} for $10 < Z < 60$; 10^{-5} – 10^{-6} for $60 < Z < 92$;	$\sim 10^{-3}$ for ^{10}B , ^{113}Cd , ^{149}Sm , ^{157}Gd ; 10^{-1} – 10^{-3} for remaining nuclei
Needed sample volume	small, (typically a capillary) $0.1 < D < 1.0$ mm	huge, (typically some cm^3)
Instrument availability	very high at lab; low at synchrotrons	very low at nuclear reactors or spallation sources
Beam flux (particle $\text{s}^{-1} \text{m}^{-2}$)	10^{10} (RA); 10^{17} (BM); 10^{24} (U)	10^{11}
Beam divergence (mrad^2)	0.5×10 (RA); 0.1×5 (BM); 0.01×0.1 (U)	10×10
Beam monochromaticity	10^{-4}	10^{-2}
$\Delta E/E$		
Main advantages	<ul style="list-style-type: none"> • high $\Delta\theta$ (Δq) resolution • fast data collection, allowing time dependent experiments to be done (sub second resolution for BM and U) • no sample radioactive activation • possibility to use μm beams for space resolved experiments 	<ul style="list-style-type: none"> • ability to detect low Z elements • ability to discriminate elements with similar Z • Advantages related to the use of isotopic-substituted samples • no radiation damage • the scattering power is constant at any θ (q)
Main disadvantages	<ul style="list-style-type: none"> • low ability to detect light elements • low ability to discriminate elements with similar Z • inability to discriminate isotopes • risk of radiation damage • the scattering power falls progressively off at increasing θ (or q) • intrinsic severe difficulties to investigate magnetic structures 	<ul style="list-style-type: none"> • ability to obtain spin density maps • moderate $\Delta\theta$ (or Δq) resolution • long acquisition times (hampering the possibility of time-resolved studies) • risk of radioactive activation of the sample • space resolved experiments are critical due to the low available flux and the low efficiency in the beam focusing • elements with high incoherent scattering lengths (such as H) should be avoided

3. XAS spectroscopy: basic background

The aim of this section is to provide the reader with a concise review of the basic physical principles on which the interpretation XAS data is based. For a more detailed description of the theoretical background and experimental aspects of XAS we refer to the extensive specialized literature (e.g. ¹²⁶⁻¹³³).

3.1. XAS theoretical background. XAS measures the variations of the X-ray absorption coefficient μ as a function of the incident X-ray energy E . According to the Fermi Golden Rule,^{6,134,135} the XAS signal is proportional to the electron transition probability from the core-state $|i\rangle$ of energy E_i to the unoccupied state $|f\rangle$ of energy E_f , as expressed by Eq.(39), where the product $\mathbf{e} \cdot \mathbf{r}$ indicates the electronic transition dipole operator,¹³⁶ where $\rho_i(occ)$ and $\rho_f(unocc)$ are the densities of initial occupied and final unoccupied states, respectively, and where $\delta(E_f - E_i - E)$ is a Dirac delta function.¹³²

$$\mu(E) \propto |\langle i | \mathbf{e} \cdot \mathbf{r} | f \rangle|^2 \delta(E_f - E_i - E) \rho_i(occ) \rho_f(unocc) \quad (39)$$

The behavior of the $\mu(E)$ function is represented in Figure 10b. A general decrease of the absorption with increasing incident energy can be noticed, following approximately the law:

$$\mu(E)/\rho \approx Z^4/AE^3, \quad (40)$$

where ρ is the sample density, Z the atomic number and A the atomic mass. This equation holds for a sample containing a unique chemical species like a metal foil, but can be easily generalized for any sample of known composition. In Figure 10b also evident is the presence of the characteristic saw-tooth like edges, whose energy position is a distinctive features of each kind of absorbing atom. These absorption edges correspond to transitions where a core-orbital electron is excited to (i) the free continuum (i.e. when the incident energy is above the ionization energy of the absorber atom) or (ii) unoccupied bond states lying just below the ionization energy. The nomenclature adopted for the edges recalls the atomic orbitals from which the electron is extracted, as shown in Figure 10a: K-edges are related to transitions from orbitals with the principal quantum number $n = 1$ ($1s_{1/2}$), L-edges refers to electron from the $n = 2$ orbitals (L_I to $2s_{1/2}$, L_{II} to $2p_{1/2}$, and L_{III} to $2p_{3/2}$ orbital), and so on for M, N, ... edges.

When the energy of the X-ray photon exceeds the ionization limit (case (i) mentioned above), the excited electron (generally named “photoelectron”) has a kinetic energy E_K given by $E_K = h\nu - E_B$, where E_B indicates the electron binding energy, that is typical of the absorption edge (K, L_I , L_{II} or L_{III}) of the selected atomic species.^{133,137} Once ejected, the photoelectron propagates thorough the sample as a spherical wave diffusing from the absorber atom, with a wavevector of modulus k defined by Eq. (41):

$$k = \frac{2\pi}{\hbar} \sqrt{2m_e E_K} \quad (41)$$

A close zoom on the energy region in proximity of an absorption edge shows a well defined fine-structure. In particular, only when the absorber is surrounded by neighboring atoms (molecules or crystals) a structure of oscillatory nature modulates the smooth $\mu(E)$ profile at energies above the edge. Figure 10c provides an example for the activated $\text{Cr}_3(\text{BTC})_2$ MOF; where the energy ranges around the Cr K-edge. Such modulation in the absorption coefficient derives from the interference between the outgoing photoelectron wave diffusing from the absorber and the wavefronts back-scattered by the neighboring atoms.^{138,139} In a typical XAS experiment, the energy range probed around the edge is conventionally divided into two different regions (Figure 10c):

- (i) X-Ray Absorption Near Edge Structure (XANES) region: portions of the XAS spectrum just below and above the edge energy;
- (ii) Extended X-ray Absorption Fine Structure (EXAFS) region: portion at higher energies in respect to the edge (from tens to hundreds of eV), characterized by the oscillatory modulation in the absorption coefficient.

Hereby, we will briefly discuss the main information that can be extracted from the analysis of each of the two regions listed above.

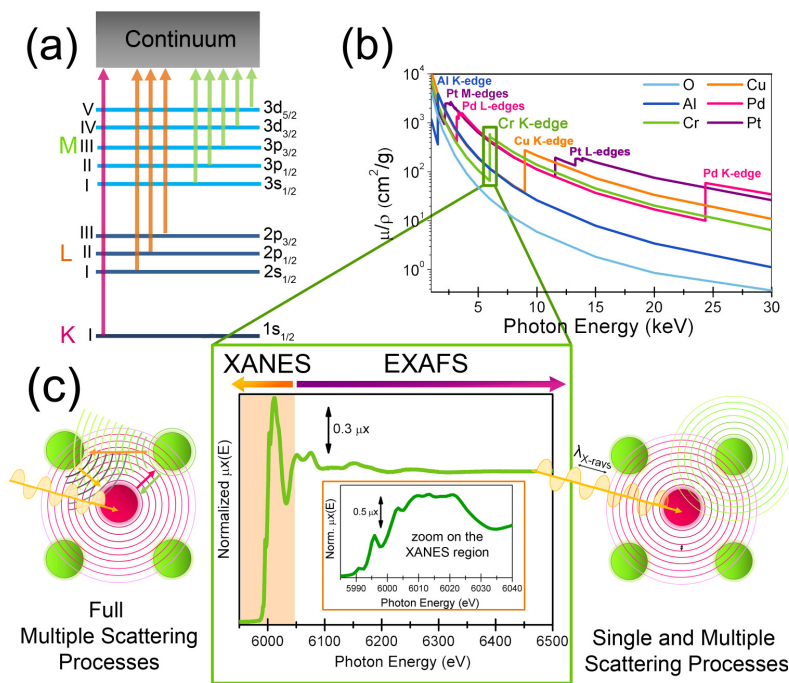


Figure 10. Part (a): X-ray absorption edges nomenclature and representation of their relation with the atomic orbitals from which the electron is extracted. Part (b): General behaviour of the X-ray absorption coefficient μ/ρ , see Eq. (40), as a function of the incident X-ray energy E for O ($Z = 8$), typically contained in MOFs organic ligands, and for some selected metals present in the MOFs cornerstones, i.e. Al ($Z = 13$), Cr ($Z = 24$), Cu ($Z = 29$), Pd ($Z = 46$), and Pt ($Z = 78$). Data obtained from NIST web site <http://physics.nist.gov/PhysRefData/XrayMassCoef/tab3.html>. Note the logarithmic scale of the ordinate axis. (c) Cr K-edge XAFS of activated $\text{Cr}_3(\text{BTC})_2$ MOF¹⁴⁰ (data collected at BM01B beamline of the ESRF). The conventional division between XANES and EXAFS region and the schematic models of full multiple and single scattering processes, dominating respectively the XANES and EXAFS region, are indicated (color code: absorber atom in magenta; neighbor atoms that back-scatter the photoelectron wave outgoing from the absorber in green). Unpublished figure.

3.2. The XANES region. As discussed in another chapter of this book,⁶ devoted to vibrational and electronic spectroscopies, the XANES part of the XAS spectrum reflects the unoccupied electronic levels of the selected atomic species. The investigation of these levels provide information on oxidation and coordination state of the absorber atom.

3.3. The EXAFS region. The EXAFS region of the spectrum is located at higher energies and is characterized by the modulation of the absorption coefficient $\mu(E)$. Such feature is caused by the interference between the X-ray waves diffused by the absorber atom and back-scattered by its neighbors. Hence, EXAFS oscillations can be related via Fourier transform to a specific spatial arrangement of the atoms in the local environment of the absorber, bridging the energy space to the real distances r -space. This crucial point is at the basis of the EXAFS analysis procedure developed after the milestone works of Sayers, Lytle and Stern.^{138,139,141}

The higher photoelectron kinetic energy in the EXAFS region implies that the phenomenon is no more dominated by the full multiple scattering (MS) regime, that instead dominate in the XANES region;¹⁴¹ consequently data analysis can be performed using the simpler Fourier transform operation.¹³⁸

The EXAFS signal $\chi(E)$ is generally expressed as the oscillatory part of the $\mu(E)$ function, normalized to the edge-jump, i.e. $\chi(E) = [\mu(E) - \mu_0(E)]/\Delta\mu_0(E)$, where $\mu_0(E)$ is the atomic-like

background absorption and $\Delta\mu_0(E)$ the normalization factor. Above the absorption edge, the energy E can be substituted with the photoelectron wave-vector k using Eq. (41), therefore obtaining the EXAFS function $\chi(k)$. The relation between the modulation of the $\chi(k)$ signal and the structural parameters is provided by the EXAFS formula that, in the single scattering (SS) approximation, is reported in Eq. (42).

$$\chi(k) = S_0^2 \sum_i N_i F_i(k) e^{-2\sigma_i^2 k^2} e^{-\frac{2r_i}{\lambda(k)}} \frac{\sin [2kr_i + 2\delta_i(k) + \theta_i(k)]}{kr_i^2} \quad (42)$$

S_0^2 is the overall amplitude reduction factor; the index i runs over all the different shells of neighboring atoms around the absorber, $F_i(k)$ is the back-scattering amplitude as a function of k for each shell, in N_i is the coordination number (number of equivalent scatterers), σ_i is the Debye-Waller factor accounting for thermal and static disorder. The parameter r_i indicates the interatomic distance of the i -th shell from the central absorber. The phase shift of the photoelectron is distinguished in two contributions, related to the absorber ($2\delta_i$) and to the scatterer (θ_i).

In Eq. (42) the electron back-scattering amplitude $F_i(k)$ is measured in \AA ,¹⁴²⁻¹⁴⁴ because the cross section, that's is an area, see Eq. (33), is the modulus squared of the back-scattering amplitude $F_i(k)$ plays a similar role than the atomic form factors $f_n(q)$ play in Eqs. (8) or (16) for X-ray scattering. Indeed $F_i(k)$ defines the weight that the i -th neighbor has in the overall EXAFS signal. As the electron scattering is mainly performed by the electron clouds of the neighbor atoms, it is evident that $F_i(k)$ will be larger for larger Z neighbors. Consequently, as was the case for X-ray scattering, EXAFS will be less efficient in the detection of low Z neighbors and the discrimination among neighbors having similar Z will be critical. When the difference in Z is sufficiently large, then both back-scattering amplitude $F_i(k)$ and phase shift functions are markedly different to allow an easy discrimination between the different neighbors, see Figure 11.

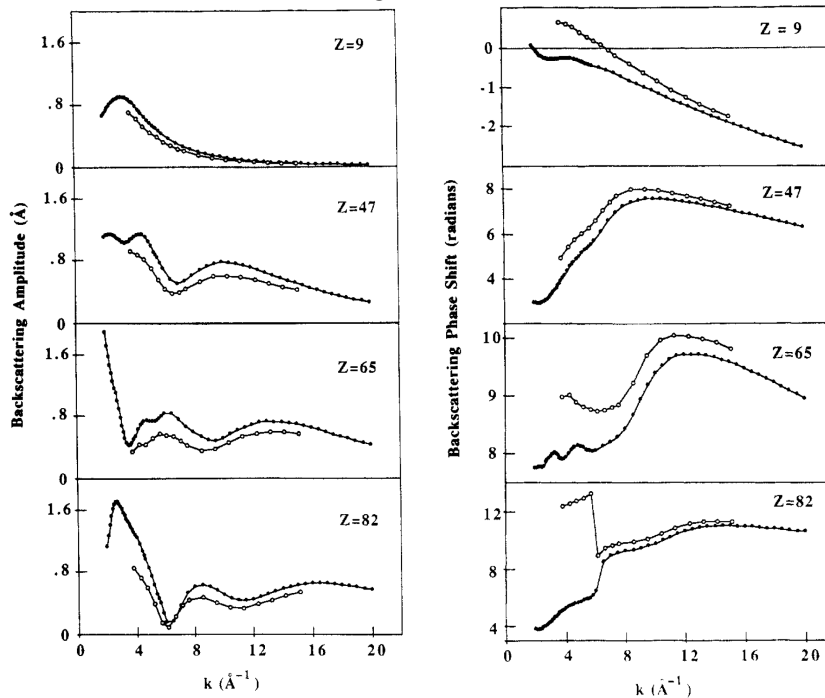


Figure 11. Left panels: Backscattering amplitude functions $F_i(k)$ (in \AA) versus k as obtained from plane wave calculations for F ($Z = 9$), Ag ($Z = 47$), Tb ($Z = 65$), and Pb ($Z = 82$) scattering atoms. Right panels: as left panels for the backscattering phase shift functions $\theta_i(k)$ (in radians) Open and full circles refer to the works of Teo and Lee¹⁴² and of McKale et al.,¹⁴³ respectively. Reproduced with permission from Ref.¹⁴³ (copyright American Chemical Society 1988).

The term $\lambda(k)$ is the energy-dependent photoelectron mean free path, typically few \AA ,¹⁴⁵ determining the local nature of the technique that can investigate only up to $\approx 5-8 \text{\AA}$ around the

photo-excited atom. This apparent limitation of EXAFS is conversely a big advantage in the investigation of disordered materials like glasses or liquids as the long range order is not required.¹⁴⁶

Coming to the Debye-Waller term $\exp(-2\sigma_i^2 k^2)$, it has the same physical origin of the term $\exp(-q^2 u_n^2/6)$ introduced in Section 2.1.4.5, for diffraction experiments,^{63,64} see Eq. (26). Actually the thermal parameters σ_i^2 , measured in an EXAFS experiment, and $u_{n,a}^2, u_{n,b}^2, u_{n,c}^2$, measured in a diffraction experiment, represents two different aspects of the atomic vibrations in crystals. The anisotropic mean squared displacements $u_{n,a}^2, u_{n,b}^2, u_{n,c}^2$, or the isotropic mean squared displacement u_n^2 measure how the n -th atom vibrates inside the unit cell along **a**, **b** and **c** directions (u_n^2 being an average of $u_{n,a}^2, u_{n,b}^2, u_{n,c}^2$). The σ_i^2 parameter measures how the couple of atoms absorber- i -th shell neighbor vibrates along the direction that connect these two atoms. This means that in case of strongly correlated vibrations, the scatterer and the absorber can vibrate in phase, resulting in a low σ_i^2 parameter and in a larger u_n^2 parameter.

The standard EXAFS formula, Eq. (42), provides a convenient parameterization for fitting the local atomic structure around the absorbing atom to the experimental EXAFS data.¹⁴⁷ The dependence of the oscillatory structure of the EXAFS signal on interatomic distance and energy is clearly reflected in the $\sin(2kr_i)$ term. The strength of the interfering waves depends on the type and number of neighboring atoms through the backscattering amplitude $F_i(k)$ and the coordination number N_i , and hence is primarily responsible of the magnitude of the EXAFS signal. Once the phase and amplitude functions have been independently measured on model compounds or *ab initio* computed, the structural parameters N_i, r_i , and σ_i^2 , can be determined in a least square approach where the difference between the experimental and the modeled $k^n \chi(k_j)$ function is minimized along all the sampled experimental points k_j . The minimization routine can be done either in k -space, directly on the measured $k^n \chi(k_j)$ function, or in r -space, working on the Fourier-transformed functions. So, for each coordination shell, the coordination number, the atomic distance and the thermal factor can be extracted from an accurate EXAFS study. Extending the Nyquist-Shannon theorem^{148,149} (also known as sampling theorem) to the EXAFS case, the maximum number of optimized parameters cannot exceed the number of truly independent points (n_{ind}), where n_{ind} is defined by the product of the sampled interval in k -space (Δk) and the interval in R -space (ΔR) containing the optimized shells:

$$n_{\text{ind}} = 2\Delta k \Delta R / \pi. \quad (43)$$

A careful monitoring of the fitting results is fundamental to avoid local or non physical minima of the minimization process. Analogously, correlation parameters between each couple of optimized parameters should ideally be lower than 0.8 in absolute value and should never exceed 0.9. Eq. (43) underlines the importance of acquiring the EXAFS spectrum over the largest possible k -interval. Experimental data collected up to a high maximum k -value k_{max} allows to: (i) increase n_{ind} , as Δk increases; (ii) reduce the correlation between N_i and σ_i parameters; (iii) increase the ability to discriminate between two close distances. The distance resolution (Δr) of an EXAFS spectrum is indeed defined from k_{max} according to the relation:

$$\Delta r = \pi / (2 k_{\text{max}}). \quad (44)$$

Two equally intense signals generated by the same scatterer located at r_1 and r_2 can indeed be singled out only in case the two oscillating functions $\sin(2k r_1)$ and $\sin(2k r_2)$ are able to generate at least a beat in the sampled k -range, and this occurs for $2k(r_1 - r_2) = \pi$. Consequently, in order to reach a distance resolution of $\Delta r = 0.1 \text{ \AA}$ the EXAFS spectrum has to be collected up to about 16 \AA^{-1} . Eq. (44) is the EXAFS-equivalent of Eq. (23) discussed for diffraction experiments.

4. X-rays and neutrons total scattering: basic considerations.

The total scattering technique,¹⁵⁰⁻¹⁵⁸ is able to provide the overall pair distribution function (PDF) $G(r)$ of the material. The experimental setup needed is that of X-ray or neutrons powder diffraction,^{159,160} but the scattering pattern has to be collected to much higher exchanged q -values,

up to at least 20–30 Å⁻¹. Low-λ sources and high-2θ collections are consequently required for PFD analysis. For standard Cu Kα (λ = 1.54 Å) and Mo Kα (λ = 0.71 Å) tubes, a collection up to 2θ = 140 ° results in $q = 7.7$ and 16.6 Å⁻¹, respectively. Working with a synchrotron sources at λ = 0.5, 0.4, 0.3 and 0.2 Å, Q values as high as 23.8, 29.8 and 39.7 and 59.0 Å⁻¹, respectively, can be reached for a data collection up to 2θ = 140 °.

To analyze PDF data, the coherent scattering function $I_C(q)$ has to be extracted from the experimentally collected intensity $I_{\text{exp}}(q)$. Before performing this operation, the background intensity due to extrinsic contributions, e.g. Compton scattering, fluorescence, scattering from the sample holder, and other experimental artifacts¹⁶¹⁻¹⁶³ has to be removed. $I_C(q)$ has sharp intensities where there are Bragg peaks, and broad features in between, the diffuse scattering. The total-scattering structure function, $S(q)$, is then obtained from $I_C(q)$ as follows:^{74,152}

$$S(q) = [I_C(q) - \langle f(q)^2 \rangle + \langle f(q) \rangle^2] / \langle f(q) \rangle^2 \quad (45)$$

where the symbol $\langle \rangle$ denotes an average over all the chemical species in the sample and $f(q)$ is the X-ray atomic form factors. As $f(q)$ decreases upon increasing q , see Figure 3 and related discussion, very long integration times are needed at high q to obtain a good statistic. For this reason, area detectors are more suitable than point detectors because allow the integration on a wide region of the diffraction cone. In addition, the poorer angular resolution of area detector is not a significant disadvantage in a q -region where the diffractogram undergoes only smooth variations. Alternatively, PDF studies can be performed using neutrons because the coherent neutron scattering length is constant in the whole q region of interest, see Section 2.2. Both $I_{\text{exp}}(q)$ and $I_C(q)$ data appear smooth and featureless in the high- q region (this holds even for crystalline materials where usually no Bragg peaks are observed above $q \approx 10$ Å⁻¹). However, after normalizing and dividing by the square of the atomic form-factor, important oscillations appear in this region of the $S(q)$ function. A similar behavior is observed in EXAFS experiments, comparing $\mu(E)$ and $\chi(k)$ functions at high E (high k or high q) after the edge. Finally, the reduced pair distribution function, $G(r)$, is obtained from $S(q)$ through a sine FT:

$$G(r) = \frac{2}{\pi} \int_{q_{\min}}^{q_{\max}} q[S(q) - 1] \sin(qr) dq, \quad (46)$$

where q_{\min} and q_{\max} are the limits of the data collection in q -space, being $q_{\min} \sim 0$ Å⁻¹ and q_{\max} as large as possible. The PDF function (46) gives the inter-atomic distance distribution, having peaks at positions r corresponding to the most probable distances between each pair of atoms in the solid. The PDF function therefore contains EXAFS-like information, that is however not atomically selective: $G(r)$ includes contributions arising from the local environments of all the atomic species present in the sample. In this regard, the intrinsic differences in the nature of the $\chi(k)$ and $S(q)$ signals obtained from EXAFS and PDF experiments on single-component disordered systems were deeply discussed by Filipponi.¹⁶⁴ In that work, particular effort was devoted to connect the $\chi(k)$ signal with quantities commonly employed within the distribution function theory in disordered matter. As the physical phenomenon behind PDF is X-ray scattering and not photoelectron scattering, the PDF signal is not damped by the short photoelectron mean-free path and by the core hole life-time as EXAFS is, see Eq. (42), so valuable structural information is contained in the pair-correlations extending to much higher values of r , than typically reachable by EXAFS (≈ 5 – 8 Å). In fact, with high q -space resolution data, PDFs can be measured out to tens of nanometers (hundreds of angstroms) and the structural information remains quantitatively reliable. With respect to EXAFS, the PDF data analysis has not to deal with MS paths, as only SS signals are present, remarkably simplifying the data modeling. However the PDF signal contains, entangled, the structural information about the local environment around all the atomic species present in the sample, and further complications are related to the isolation of the different contributions.

5. Applications

5.1. Determination of possible interpenetrating frameworks and of possible extra-phases in some MOF-5 synthesis by combining single crystal XRD, XRPD and Zn K-edge EXAFS

5.1.1. Problems related to synthesis reproducibility of MOF-5 Traditionally, MOF syntheses have been designed to yield high quality single crystals suitable for structural analysis. A diversity of methods have been adopted, and they often involve a slow introduction of the reactants to reduce the rate of crystallite nucleation, such as slow diffusion of one component solution into another through a membrane or an immobilizing gel, slow evaporation of a solution of the precursors, or layering of solutions. Fortunately, solvothermal techniques have been found to be a convenient replacement for these often time-consuming methods. However, if an increased yield is more desirable than a high crystal quality, the reaction times can be significantly reduced by increasing reactant concentration and by employing agitation.^{165,166} The product formed under these conditions may or may not be exactly identical to those obtained from methods used to produce highly crystalline MOF materials.

In this regard, MOF-5 material represents a case study because of both its high popularity (it is probably the most highly cited MOF) and the large number of different synthesis recipes reported in the literature. Indeed, the initial findings of reversible hydrogen adsorption,¹⁶⁷⁻¹⁶⁹ thermal robustness^{170,171} and interesting luminescence properties,¹⁷² of MOF-5 have made it one of the most studied MOFs. Moreover, a broad set of synthesis conditions and procedures have been tried to obtain MOF-5 either in large scale or with particular crystallite size or to reduce synthesis time.^{173,174} Yaghi and co-workers have reported several different synthesis methods for MOF-5, and all of them yield a product with a fairly large crystallite size, suitable for structure determination.^{170,175} Huang et al.¹⁷³ reported a synthesis strategy for fast formation of nanocrystalline MOF-5. Naturally, the inherent challenge with a nanocrystalline material is the limited structure information provided by XRPD. Successively Ni et al.¹⁷⁴ presented a new microwave-assisted solvothermal synthesis approach, which allows MOF-5 crystals of uniform size ($4 \pm 1 \mu\text{m}$) to be synthesized in less than a minute. On the basis of the similar, or at least related, powder XRD patterns the products from all the synthesis procedures have been claimed to be the same MOF-5 phase. However, after a careful scrutiny of the published XRPD patterns, Lillerud and co-workers¹⁶⁶ revealed clear intensity differences, especially in the two first and most intense peaks, see left part of Figure 12. Substantial variations in the surface area, ranging from 700 to 3400 m²/g) of MOF-5 prepared according to the different procedures have also been reported, but where not explained.^{168,173,176,177}

5.1.2. XRPD and single crystal XRD studies To clarify this inconsistency in the literature data, Lillerud et al.¹⁶⁶ prepared two set of MOF-5 material, the first repeating Huang's synthesis, resulting in nano-sized crystals (hereafter MOF-5_n), the second modifying slightly Huang's method to obtain micro-sized sufficiently large for single-crystal XRD characterization (hereafter MOF-5_m).

The left part of Figure 12 reports the XRPD patterns of (a) MOF-5_m, (b) MOF-5_n, (c) digitalized powder XRD pattern of MOF-5 (from the work of Huang et al.,¹⁷³) (d) simulated powder XRD pattern of a MOF-5 crystal, and (e) digitalized powder XRD pattern of MOF-5 (from the work of Yaghi et al.¹⁷⁵) From this comparison Lillerud et al.¹⁶⁶ deduced that the experimental pattern obtained on a high-surface-area MOF-5 reported by Yaghi et al.¹⁷⁵ (Figure 12e) is well consistent with the calculated MOF-5 pattern (Figure 12d) and that the patterns of MOF-5_m, MOF-5_n nanocrystalline MOF-5 reported by Huang et al.¹⁷³ (Figure 12a,b,c) are similar among them and deviate significantly from the pattern of the ideal MOF-5 phase (Figure 12d,e). Main differences in the XRPD patterns concern the intensities of the first (6.9° , corresponding to a d of 12.8 Å) and second (9.7° , corresponding to a d of 9.1 Å) peak. As expected, the larger crystals of MOF-5_m give less peak broadening, and the peak at 9.7° consists of two distinct contributions. This peak

splitting phenomenon do not occur for MOF-5_n. On the basis of the reported XRPD patterns and on the Langmuir surface areas of MOF-5_n (747 m²/g) and MOF-5_m (1104 m²/g) Lillerud et al.¹⁶⁶ concluded that MOF-5_m, MOF-5_n and the nanocrystalline MOF-5 reported by Huang et al. (722 m²/g) represent the same phase.

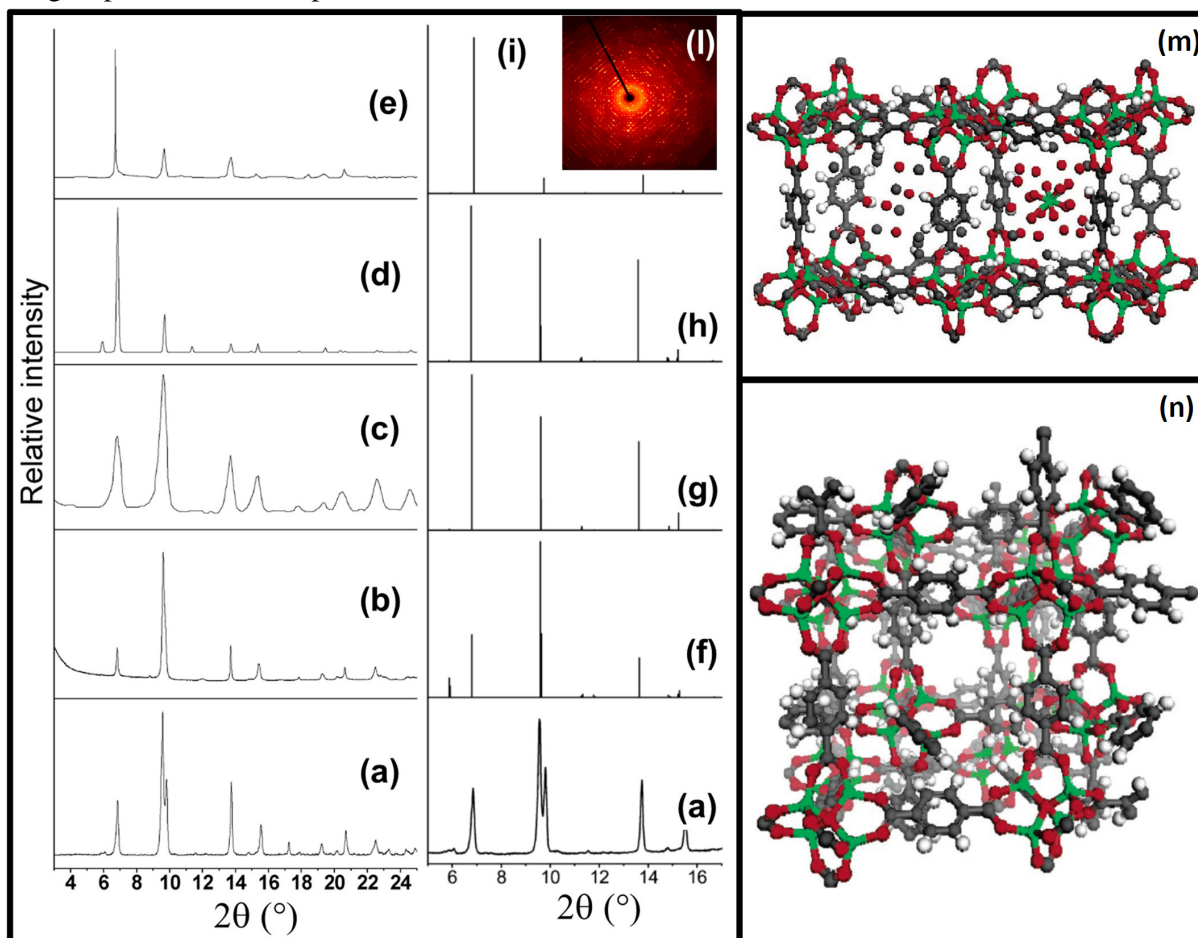


Figure 12. Comparison among experimental XRPD patterns of MOF-5 obtained in different labs, from different synthesis and comparison with some simulated XRPD patterns. Patterns have been collected with (or computed for) Cu K α radiation ($\lambda = 1.5406 \text{ \AA}$). (a) Experimental XRPD of MOF-5_m by Lillerud et al.¹⁶⁶ The pattern has been reported in both left and right parts of the Figure for comparison. (b) Experimental XRPD pattern of MOF-5_n by Lillerud et al.¹⁶⁶ (c) Experimental XRPD pattern by Huang et al.¹⁷³ (d) simulated powder XRD pattern for MOF-5 according to the ideal structure. (e) Experimental XRPD pattern by Yaghi et al.¹⁷⁵ Right part: simulated patterns (reported without line broadening) of; MOF-5_m_Zn (f); MOF-5_m_int with solvent in the pores (g); MOF-5_m_int without solvent in the pores (h); and original MOF-5 when transformed from cubic to trigonal symmetry (i). Part (l) report a 2D diffraction image collected on MOF-5_m at ESRF ID11 beamline ($\lambda = 0.38745 \text{ \AA}$). Parts (m and n): Sticks and balls representation of structure refined from single crystal XRD performed on samples selected from MOF-5_m synthesis. Zn atoms are shown in green, O in red, C in gray, and H in white. Part (m): Structure of MOF-5_m_Zn with Zn cluster in the small cage and unorganized solvent in the large cage; the electron densities are illustrated with partly occupied oxygen and carbon atoms. Part (n): Structure of MOF-5_m_int showing two interpenetrated MOF-5 ideal lattices. Figure adapted from Ref.¹⁶⁶

The microcrystalline nature of samples allowed Lillerud et al.¹⁶⁶ to perform synchrotron radiation single crystal data collection (ESRF ID11, see part (l) of Figure 12, and refinement so attaining a deeper understanding of this material. The single-crystal data were collected for more than ten different MOF-5_m crystals. During this procedure two different kinds of MOF-5_m crystals were discovered, hereafter denoted MOF-5_m_Zn and MOF-5_m_int. MOF-5_m_Zn structure was solved in the trigonal $R\bar{3}m$ space group (No. 166), while the original MOF-5 structure has a cubic symmetry ($Fm\bar{3}m$, No. 225). Its structure, reported in Figure 12m, has a

framework consisting of the same building units as the ideal MOF-5, but exhibiting additional electron density in the center of the cavities (i.e., the half of the cages where the benzene rings are twisted into the cage center). The best refinement was obtained by assigning the electron density to a Zn atom with occupancy of 0.5. The coordination sphere of the Zn atom consists of partially occupied oxygen positions. Figure 12n illustrates the structure of MOF-5_m_int after removal of the solvent. MOF-5_m_int consists of two MOF-5 frameworks interpenetrated with each other. The frameworks are not physically connected, but there is sufficient interaction to cause a significant distortion of the cell from cubic to trigonal. The structure was therefore also refined in the $R\bar{3}m$ space group with an equal occupation of the two frameworks.¹⁶⁶ Summarizing, in MOF-5_m_Zn (Figure 12m) the Zn-O species in the pores cause change in the axes lengths, while in the MOF-5_m_int the interaction between the two interpenetrated frameworks is responsible for the same effect. These results show that the large MOF-5 cell is highly flexible and allows significant changes in the unit cell axes without destroying the structure. The models of the two phases reported in Figure 12m,n are also able to take into account for the large deviation in the surface area of MOF-5 materials (700-3400 m²/g) reported in the literature:^{168,173,176,177} as for MOF-5_m_Zn, the presence of the nonvolatile compounds (Figure 12m) makes the host cavity inaccessible and may also block the entrance to the adjacent cavities, while for MOF-5_m_int, the presence of doubly interpenetrated MOF-5 networks will also reduce the adsorption capacity. These models were also in agreement with the reported XRPD patterns (Figure 12ab), because it is well known from the large experience on zeolitic materials that when crystalline materials have the pores filled with electron density (from whatever origin: template, or adsorbed molecules etc...) then the intensity of the low 2 θ peaks increases.^{178,179}

Combining single crystal XRD and TG data, Lillerud et al.¹⁶⁶ were able to conclude that the MOF-5_m batch is composed by of 94% MOF-5_m_Zn and 6% MOF-5_m_int.

5.1.3. Role of EXAFS in determining extra phase Zn species foreseen by XRD The missing part of the puzzle was a direct, atomically selective, proof that the electron density found in the MOF-5_m_Zn phase (representing 94 % of the MOF-5_m batch) by single crystal XRPD is actually attributable to zinc oxide nanoclusters. Zn K-edge EXAFS is of course the technique of choice to answer to this question. Lillerud et al.¹⁶⁶ performed XANES and EXAFS measurements on both MOF-5_m and MOF-5_n batches finding very similar results, indicating that the average Zn local environment is basically the same in both syntheses. Authors concluded that solvent removal does not affect neither the XANES nor the EXAFS spectra, testifying that Zn atoms in MOF-5 does not exhibit any coordination vacancy.

The fit of the EXAFS signal using the path degeneration, expected from the ideal MOF-5 structure obtained by XRD, failed because was not able to correctly reproduce the relative intensities of the first and second shell contributions: with respect to the experimental datum, the fit underestimated the first shell contribution, attributing to this path a physically too high σ^2 value, while the second shell peak was overestimated with a too small σ^2 value. The failure of this fit was the consequence of the presence of a highly disordered nano-structured zinc oxide phase trapped inside the MOF-5 cavities. Disordered nanoclusters are expected to give mainly just a first shell Zn-O contribution, so explaining the inability to reproduce the intensity ratio between first and second shell contribution using as model the ideal MOF-5 structure. The quality of the fit significantly improved by adding an extra-phase Zn-O contribution.¹⁶⁶ The Zn-O distance of this phase was optimized at 2.11 ± 0.01 Å. This value is somewhat stretched with respect of the Zn-O distance in crystalline zinc oxide as expected for highly disordered nanoclusters. So Zn K-edge EXAFS was able to attribute the electron density found in the single crystal XRD study of the MOF-5_m_Zn phase to highly disordered ZnO nano-clusters.¹⁶⁶

5.2. Combined XRPD, EXAFS and ab initio study of NO, CO and N₂ adsorption on Ni²⁺ sites in CPO-27-Ni.

Dietzel et al.¹⁸⁰ synthesized a three-dimensional honeycomb-like metallorganic framework (Figure 13a) with Ni²⁺ as the metal component: Ni₂(dhtp)(H₂O)₂·8H₂O (dhtp = 2,5-dihydroxyterephthalic acid). This new material, named CPO-27-Ni, belongs to the family of CPO-27-M (Mg, Co, Ni) also known as MOF-74 (synthesized by Yaghi and co-workers) and is isostructural to framework materials with Zn²⁺, Co²⁺ and Mg²⁺ metal component.¹⁸¹⁻¹⁸⁴

The structure of CPO-27-Ni was solved by Dietzel et al.¹⁸⁰ using synchrotron XRPD data collected at BM01B beamline of the ESRF at $\lambda = 0.50134 \text{ \AA}$. The data were refined up to $2\theta_{\max} = 34.5^\circ$ and 28.0° for the hydrated and dehydrated forms, resulting in $d_{\min} = 0.85$ and 1.04 \AA , respectively, see Eq. (23). CPO-27 framework contains one-dimensional channels (Figure 13a) filled with water that can be removed by a mild thermal treatment. Upon dehydration the crystalline structure is preserved and a material with a high surface area is obtained (about $1100 \text{ m}^2/\text{g}$), which contains unsaturated metal sites organized in helicoidal chains.¹⁸⁰ At the intersections of the honeycomb are helical chains of cis-edge connected nickel oxygen octahedra running along the *c* axis. Nearest neighbors helices are of opposite handedness. Each chain is connected by the organic ligand with three adjacent chains, resulting in the honeycomb motif. The channels in the honeycomb have a diameter of $\sim 11 \text{ \AA}$ (see Figure 13a). All of the O atoms of the ligand are involved in the coordination of Ni²⁺; these oxygen atoms account for five out of six ligands for each nickel atom, while the sixth coordinative bond is to a water molecule which points towards the cavity.

CPO-27-Ni, in both its hydrated and dehydrated forms, was studied in detail by Bonino et al.¹⁸⁵ The refined structure from XRPD Rietveld refinement¹⁸⁰ was used as input for the EXAFS model, resulting in an excellent agreement between the set of distances optimized with the two different techniques. The EXAFS signal was quite complex because constituted by several SS and MS paths. Therefore Bonino et al.¹⁸⁵ cross-checked the validity of their EXAFS model analyzing the data collected on dehydrated CPO-27-Ni at 300 and 77 K (see Table 3). The model was validated as all optimized distances were comparable in the two datasets, while the thermal parameters σ , see Eq. (42), increased moving from 77 to 300 K. Water removal from CPO-27-Ni significantly both its XANES and EXAFS spectra. In particular, the average Ni-O first shell distance decreases from $2.03 \pm 0.01 \text{ \AA}$ down to $1.99 \pm 0.01 \text{ \AA}$, while an even more impressive contraction was observed for the second shell Ni-Ni distance, that moves from $2.980 \pm 0.005 \text{ \AA}$ down to $2.892 \pm 0.005 \text{ \AA}$, see Table 3. The desolvation process caused in the removal of the water molecule coordinated to the metal center, resulting in Ni²⁺ cations with a coordinative vacancy potentially able to coordinate ligand molecules. The interaction of NO, CO and N₂ ligands with desolvated CPO-27-Ni has been deeply investigated by means of Ni K-edge XANES and EXAFS spectroscopies, supported by parallel IR and UV-Vis techniques.¹⁸⁵⁻¹⁸⁷

High quality data were obtained in transmission mode up to almost $k = 20 \text{ \AA}^{-1}$, see Figure 13b: this allowed to reach a high resolution in R-space, better than 0.08 \AA see Eq. (44). The EXAFS data (and corresponding best fits) obtained on dehydrated CPO-27-Ni and after interaction with H₂O, NO, CO and N₂ are reported in R-spaces in Figure 13c-g and Table 3. The higher intensity of the EXAFS oscillation in the case of the CPO-27-Ni/CO and CPO-27-Ni/N₂ is evident and is due to the fact that corresponding spectra were collected at 77 K,^{186,187} while the spectra of CPO-27-Ni contacted by H₂O and NO were collected at 300 K.¹⁸⁵ This implied that authors were forced to fix much more parameter in the analysis of the this last case, see Table 3. Independent IR experiments allowed to fix the coordination number of the adsorbed molecules (NO, CO and N₂) to 1,¹⁸⁵⁻¹⁸⁷ see also in this book Section 2.4.4. of Chapter.⁶

Table 3. Summary of the parameters optimized by fitting the EXAFS data collected at 77 K. The fits were performed in R-space in the $1.0\text{-}5.0 \text{ \AA}$ range over k^3 -weighted FT of the $\chi(k)$ functions performed in the $2.0\text{-}18.0 \text{ \AA}^{-1}$ interval. A single ΔE_0 and a single S_0^2 have been optimized for all SS and MS paths. The Ni-O, and Ni-Ni (first and second neighbor) SS paths have been modeled with their own path length and Debye-Waller factors, while a unique σ^2 and a unique path length parameter α , common to all other SS and MS paths, have been optimized. NO, CO and N₂

adsorption have been simulated by treating the molecule as a rigid body linearly adsorbed on Ni²⁺. Consequently only two additional parameters are needed: the Ni-molecule distance (R_{ads}) and the corresponding Debye-Waller factor (σ_{ads}^2). Nind = number of independent points ($\pi\Delta R\Delta k/2$); Nvar = number of optimized parameters. Unpublished table summarizing data from Refs. ¹⁸⁵⁻¹⁸⁷

Sample condition	Dehydrated from Ref. ¹⁸⁵	In vacuo from Ref. ¹⁸⁵	Hydrated from Ref. ¹⁸⁵	+ NO from Ref. ¹⁸⁵	+ CO from Ref. ¹⁸⁶	+ N ₂ from Ref. ¹⁸⁷
T (K)	300	77	300	300	77	77
R_{factor}	0.043	0.033	0.027	0.045	0.018	0.011
Nind	40	40	40	40	40	40
Nvar	10	10	7	7	12	12
ΔE_0 (eV)	-2.5 ± 1.0	-1.7 ± 1.0	0.5 ± 0.5	-2.5 ± 1.0	0.8 ± 0.7	2.1 ± 1.0
S_0^2	1.17 ± 0.09	1.20 ± 0.08	1.17	1.17	1.18 ± 0.06	1.18 ± 0.05
$\langle R_0 \rangle$ (Å)	1.99 ± 0.01	2.00 ± 0.01	2.03 ± 0.01	1.99 ± 0.01	2.024 ± 0.005	2.012 ± 0.005
$\sigma^2(\text{O})$ (Å ²)	0.0049 ± 0.0005	0.0042 ± 0.0004	0.0049	0.0049	0.0044 ± 0.0004	0.0038 ± 0.0003
R_{Ni1} (Å)	2.892 ± 0.005	2.889 ± 0.005	2.980 ± 0.005	2.95 ± 0.01	2.973 ± 0.005	2.937 ± 0.005
$\sigma^2(\text{Ni}_1)$ (Å ²)	0.0055 ± 0.0006	0.0045 ± 0.0004	0.0055	0.0055	0.0038 ± 0.0004	0.0035 ± 0.0003
R_{Ni2} (Å)	4.82 ± 0.02	4.87 ± 0.01	4.78 ± 0.03	4.79 ± 0.02	4.89 ± 0.02	4.86 ± 0.02
$\sigma^2(\text{Ni}_2)$ (Å ²)	0.0059 ± 0.0018	0.0052 ± 0.0014	0.0059	0.0059	0.008 ± 0.002	0.006 ± 0.002
α	-0.008 ± 0.009	-0.003 ± 0.007	-0.021 ± 0.005	-0.024 ± 0.007	-0.013 ± 0.009	-0.003 ± 0.007
σ^2 (Å ²)	0.009 ± 0.004	0.007 ± 0.003	0.009	0.009	0.009 ± 0.005	0.009 ± 0.004
R_{ads} (Å)	-	-	2.10 ± 0.04	1.85 ± 0.02	2.11 ± 0.02	2.27 ± 0.03
σ_{ads}^2 (Å ²)	-	-	0.01 ± 0.01	0.0065 ± 0.002	0.006 ± 0.002	0.010 ± 0.005
$-\Delta H_{\text{ads}}^{\text{expt}}$ (kJ mol ⁻¹)	-	-	100	92	58	17

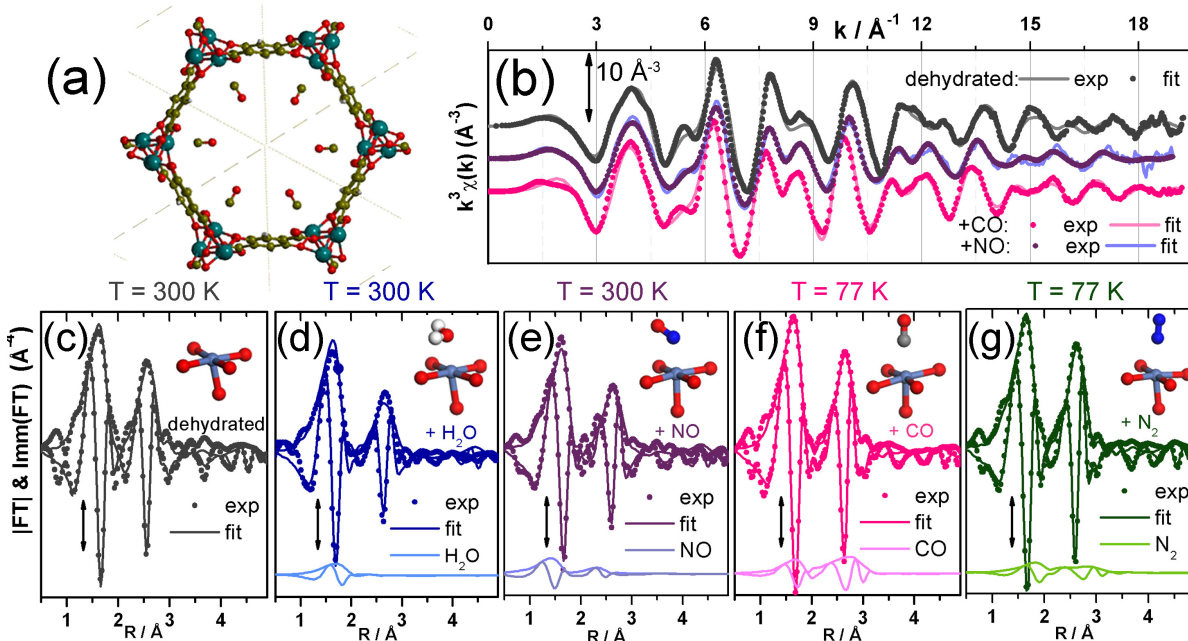


Figure 13. Part (a): the structure CPO-27-Ni/CO (Ni²⁺:CO = 1) optimized by periodic ab initio periodic approach with CRYSTAL code^{188,189} and viewed along the *c* axis. Part (b): $k^3\chi(k)$ of CPO-27-Ni after: desolvation (gray curves); interaction with NO (violet curves); and interaction with CO (pink curves). Parts (c)-(g): modulus and imaginary part of the k^3 -weighted, phase uncorrected, FT of the EXAFS spectra collected on dehydrated CPO-27-Ni (c); and after interaction with H₂O (d); NO (e); CO (f) and N₂ (g). Where adsorbates are present, vertically translated also the contribution (in both modulus and imaginary parts) of the adsorbed molecule optimized in the fits is reported. The models used in the fits adopted a Ni²⁺/adsorbate = 1:1 stoichiometry and assumed a linear adsorption geometry for CO and N₂ and a Ni-N-O angle of 130° for the NO (only the O atom of the H₂O molecule has been included in the fit). Insets report the local environment of Ni²⁺ in its dehydrated form, part (a), and upon molecular adsorption parts (b-e), as optimized by ab initio calculations. In parts (b)-(g) scattered and continuous curves refers to the experimental data and the best fit, respectively. Unpublished figure: the EXAFS spectra have been adapted from Refs. ¹⁸⁵⁻¹⁸⁷

Adsorption of molecules on Ni^{2+} sites strongly modifies the whole framework structure inducing elongation in Ni-O and Ni-Ni distances. Figure 14a-d summarizes experimental structural data (XRPD and EXAFS) on the adsorption of H_2O , NO , CO , CO_2 , and N_2 , molecules on CPO-27-Ni material. Data are reported as a function of the enthalpy of adsorption measured via standard microcalorimetric^{185,186} or via temperature-dependent IR desorption¹⁸⁷ or via isosteric heat of adsorption.¹⁹⁰ The figure summarizes data collected at both 77 and 300 K (open and full symbols, respectively). Comparison with the analogous values obtained from a theoretical study performed at the B3LYP-D*/TZVP level of theory (using a periodic boundary conditions) is reported in parts (e)-(h) of Figure 14.

From the reported set of data, it clearly emerges that computed framework distances and computed adsorption distances are systematically overestimated by the theory. Notwithstanding this fact, the trends observed in the experimental data are clearly mirrored by the theoretical data. In particular, it emerges from both experimental and theoretical data that, the larger is the adsorption energy, the larger is the perturbation induced by the adsorbed molecule to the MOF framework in terms of elongation of elongation of the $\langle R_{\text{O}} \rangle$, R_{Ni1} and R_{Ni2} distances, see parts (a)-(c) and (e)-(g) of Figure 14, respectively. As far as the adsorption distance is concerned, it follows an opposite trend: the larger is the $-\Delta H_{\text{ads}}$ ($-\Delta E_{\text{ads}}^{\text{c}}$), the shorter is R_{ads} , see Figure 14d and Figure 14h, respectively.

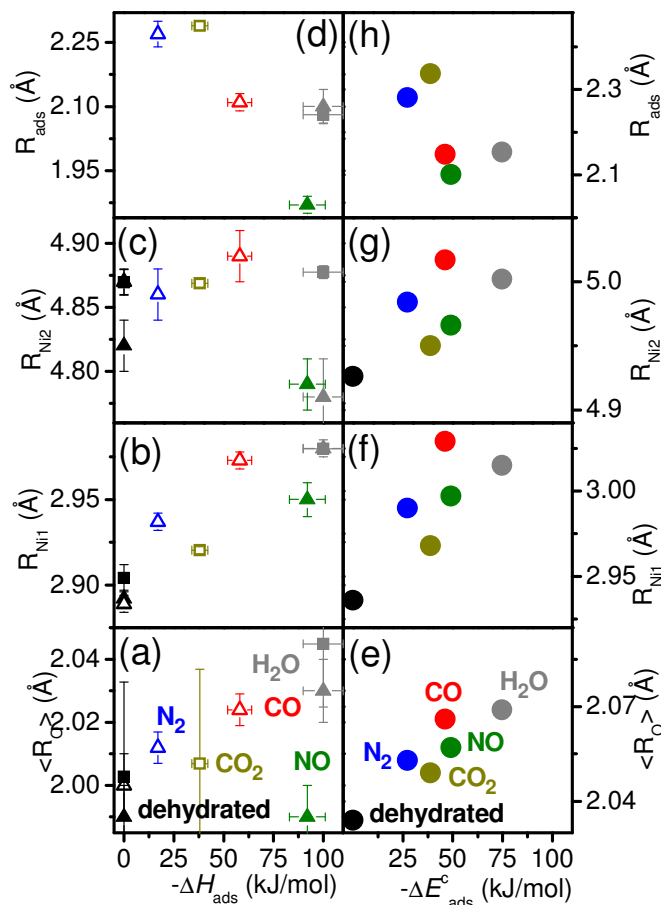


Figure 14. Correlation of the different structural parameters upon molecular adsorption on Ni^{2+} site with the corresponding adsorption energy. Left: experimental values (HRPD circles, EXAFS triangles) and corresponding uncertainties. Full and open symbols refer data collected at 300 and 77 K, respectively. Right: theoretical values. Note that left and right parts do not have the exactly the same ordinate intervals. This reflects the systematic overestimation of the theoretical distances. Beside this fact all trends are well reproduced. Adapted with permission from Ref.¹⁸⁹ Copyright 2012 Elsevier.

Regarding the EXAFS results, it is worth noticing that $\langle R_O \rangle$, and R_{Ni2} increase by decreasing the temperature from RT (filled triangles) to 77 K (empty triangles) while R_{Ni1} does not change. An increase in the cell volume by decreasing the temperature indicates a negative thermal expansion coefficient; this rare property is shared by some other MOF structures, as determined by temperature dependent diffraction experiments on MOF-5¹⁹¹⁻¹⁹³ or foreseen by force-field calculations on the IRMOF-1/-10/-16 family,^{72,194,195} and on HKUST-1.^{196,197}

For what concerns the calculations they predict upon the adsorption an increase of all the framework distances considered and an almost linear relationship between the adsorption energy and the distance elongation Figure 14(e)-(g). These findings have been confirmed by the experiments: as a general statement both XRD and EXAFS indicate an increase of all the framework distances upon molecular adsorption. However, in the experiments a larger spread of the data is observed due to the different coverages adopted in the different experiments. In fact, whereas in the calculations the coverage was fixed to Ni:molecule = 1:1, in the XRD for CO₂ and H₂O a Ni:CO₂ = 1:0.5-0.6 and Ni:H₂O = 1:5 were adopted. It is likely ascribable to the different coverage the different behaviour observed for H₂O adsorption of R_{Ni2} obtained with EXAFS and XRPD, that indicate respectively a shortening and a lengthening of this distance. In fact, whereas the XRPD data have been recorded for the highest coverage, the EXAFS measurements have been recorded at a lower Ni:H₂O ratio and then the Ni_{ads} -Ni₂ shortening is a reflection of the high interaction energy. In fact a shortening of R_{Ni2} has been also observed for NO, the second in interaction energy among molecules considered in Figure 14. Coming to the distance between the Ni atom and the adsorbed molecules (R_{ads}), in this case an opposite trend is observed in both experiments and calculations as expected: in fact this distance shortens by increasing the energetic of the interaction, the shortest distances being observed for the larger interacting molecules that is for H₂O and NO.

The here reviewed multitechnical approach^{180,184-187,189,190} requiring XRPD and EXAFS for structural determination and micro-calorimetry or temperature-dependent IR desorption or isosteric heat of adsorption for adsorption enthalpies determination and supported by periodic DFT calculation, is relevant in understanding and foreseeing applications to a potential practical uses of MOF materials. Indeed, the understanding of the molecular adsorption on a given surface site is the first step in understanding whether the site may have a potential catalytic reactivity or not.¹⁹⁸ On the other hand, measuring (and/or computing) adsorption enthalpies of different molecules allows to establish an adsorption strength scale that is relevant in determining a selective adsorption ranking useful for gas separation and selective adsorption purposes. More in detail: (i) The significant difference in the $-\Delta H_{ads}$ (and $-\Delta E_{ads}^c$) for the adsorption of H₂ and CO implies that CPO-27-Ni is an interesting material for the purification of a H₂/CO mixture used to feed fuel cells. (ii) The material can clearly play a role also in the CO₂ capture, even at relatively high temperatures, i.e. for *post-combustion* capture as demonstrated by the work of Dietzel et al.¹⁹⁰ (iii) Finally, the ability of H₂O to progressively displace NO from the Ni²⁺ sites,¹⁸⁵ makes CPO-27-Ni a good candidate for a controlled NO drug delivery inside the human body, similarly to the HKUST-1 MOF investigated by the group of Morris.^{199,200}

5.3. Combined XRPD, EXAFS and ab initio studies of structural properties on MOFs of the UiO-66/UiO-67 family: same topology but different linkers or metal

The recently discovered UiO-66/67/68 class of isostructural MOFs²⁰¹ has attracted great interest because of its remarkable stability at high temperatures, high pressures and in presence of different solvents acids and bases.¹⁸⁸ UiO-66 is obtained connecting Zr₆O₄(OH)₄ inorganic cornerstones with 1,4-benzene-dicarboxylate (BDC) as linker, while the isostructural UiO-67 material, obtained using the longer 4,4' biphenyl-dicarboxylate (BPDC) linker²⁰² (Figure 15a) and Hf-UiO-66 is obtained keeping the UiO-66 linker (BDC) and substituting the Zr₆O₄(OH)₄ blocks with Hf₆O₄(OH)₄ corners (inset in Figure 15e). XRPD, see Figure 15b,e testifies the quality of the synthesis. Due to the rigidity of the framework several isostructural UiOs has been prepared and tasted for the stability

and gas adsorption. Kandiah et al.²⁰³ studied the thermal and chemical stabilities of isostructural UiO-66-X (X= NH₂, Br and NO₂) and observed the lower stability of this analogue with respect to parent UiO-66. Conversely, as documented by the thermogravimetry studies reported in Figure 15c,f UiO-67²⁰² and Hf-UiO-66²⁰⁴ show thermal and chemical stability similar to that of UiO-66 and exhibit the expected surface area, as determined by low temperature volumetric N₂ adsorption isotherms (Figure 15d,g). Such a high stability is related to the fact that each Zr- (Hf-) octahedron is 12-fold connected to adjacent octahedra. This connectivity is very common for metals, resulting in the highly packed fcc structure, but it is still almost unique in MOF topologies.

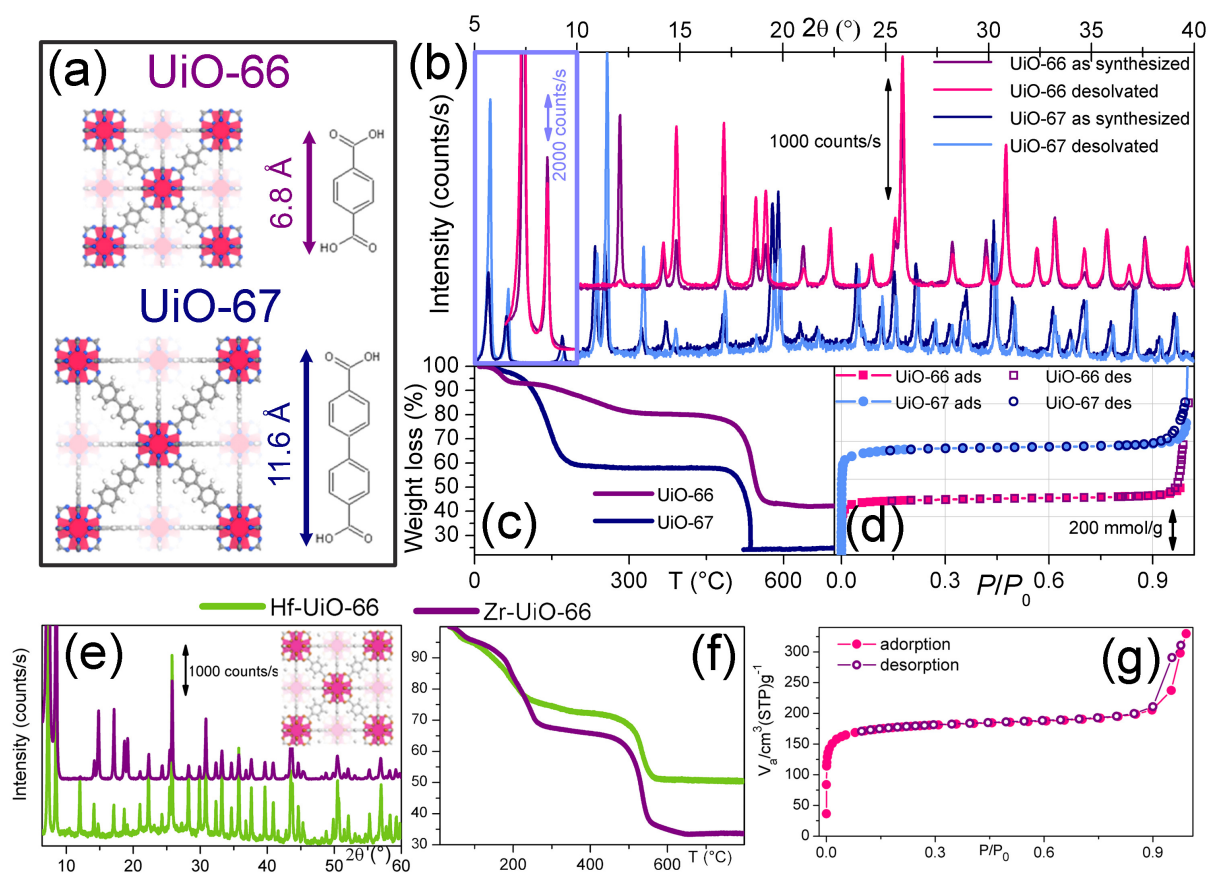


Figure 15. Part (a): From top to bottom: comparison of the dimension of linker and structure for the isostructural UiO-66 and UiO-67 MOFs. Part (b): Comparison of the XRPD patterns ($\lambda=1.540 \text{ \AA}$) for as prepared UiO-66 (UiO-67), violet (dark blue) curve and activated at $300 \text{ }^\circ\text{C}$ (pink and light blue curves). The patterns in the $10\text{-}40 \text{ } 2\theta$ region have been amplified by a factor 4. Patterns related to UiO-66 have been vertically translated for clarity. Part (c): TGA curve of UiO-66 and UiO-67 samples, violet and dark blue curves, respectively. In both cases, the heating ramp was of 5 C/min in a N₂ flow (100 ml/min). Part (d): volumetric N₂ adsorption isotherms recorded at 77 K on UiO-66 (squares) and UiO-67 (circles). Filled and empty scatters refer to the adsorption and desorption branches, respectively. Part (e): XRPD pattern ($\lambda=1.540 \text{ \AA}$) of Hf-UiO-66 (green) and Zr-UiO-66 (violet) in their solvated forms. The inset reports the MOF structure. Part (f): weight loss of Hf-UiO-66 and Zr-UiO-66 relative to the start mass (green and violet curve, respectively). Since hafnium is 41% heavier than zirconium, the Zr-UiO-66 shows both higher initial and breakdown losses. Part (g): N₂ adsorption/desorption isotherm for Hf-UiO-66 at 77 K . Unpublished figure reporting data from Refs.^{188,201,202,204,205}

The desolvation process left almost unchanged the XRPD pattern of such materials (Figure 15b): besides a gain of intensity of the basal reflections (due to the removal of the electron density inside the pores)^{166,178,179} all peaks remains in almost the same 2θ position with small intensity changes. Conversely, an huge modification of the EXAFS spectra is obtained in all cases, see Figure 16.

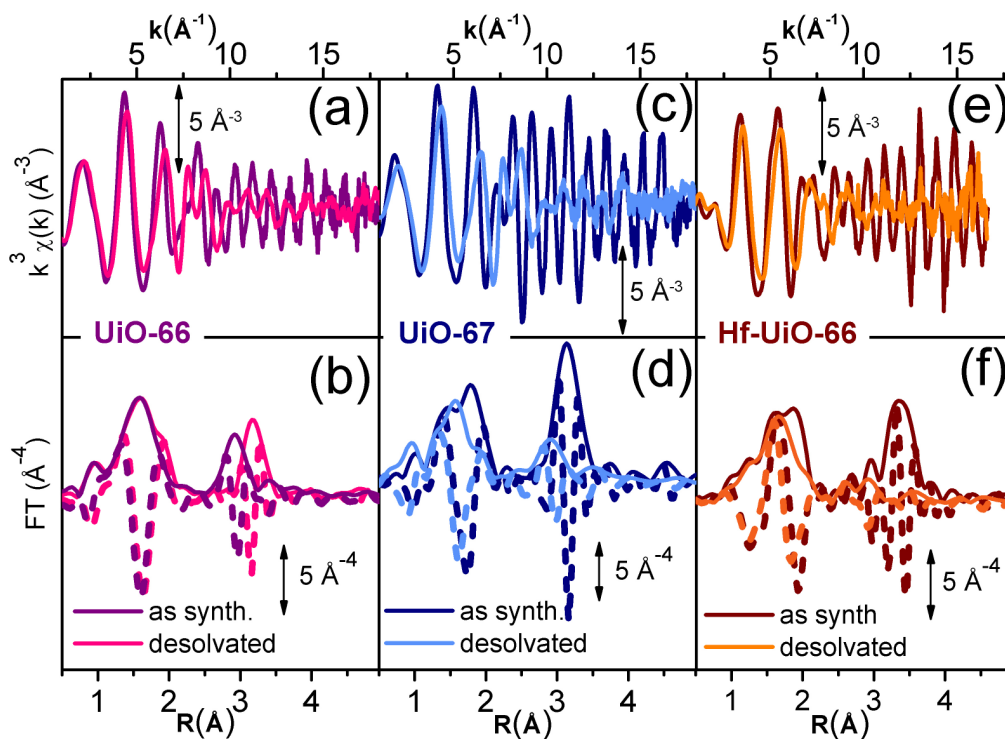


Figure 16. k- (top panels) and R-space (bottom panels) EXAFS data collected on UiO-66, UiO-67 and Hf-UiO-66, parts (a,b), (c,d) and (e,f), respectively. Both as synthesized (or hydroxylated) and desolvated (or dehydroxylated) forms of the three different isostructural MOFs have been measured. With the exception of desolvated Hf-UiO-66 sample (collected at 573 K) remaining spectra were collected at 300 K. Unpublished figure reporting data from refs.^{188,201,202,204,205}

In the three hydroxylated materials, the structure determined from the Rietveld refinement of the XRPD corresponding patterns resulted in a straightforward interpretation of the complex EXAFS signals, see first three columns in Table 4. The dramatic modification undergone by the EXAFS spectrum upon dehydroxylation (see Figure 16) makes the data analysis not so straightforward. In the case of UiO-66 (see Figure 16b, but similar effects are observed in the two other cases) the changes are basically explained in terms of three main effects: (i) small contraction of the first M-O shell accompanied by a small decrease in coordination (erosion of the shoulder around 1.9 Å); (ii) relevant distortion of the second shell contribution showing a maximum that moves from 3.17 Å to 2.91 Å, with a shoulder at 3.41 Å, thus reflecting an important splitting of the R_{M1} distances of the octahedron sides; (iii) the almost complete disappearance of the weak contribution around 4.7 Å, due to the M-M SS signal of the octahedron diagonal (R_{M2}). For the three cases, differently to the hydroxylated cases, the 3D model obtained from the Rietveld refinement of XRPD data in the highly symmetric *Fm-3m* space group was inadequate to simulate the experimental datum. The origin of this failure was, obviously due to the inability of the model to account for two different R_{M1} and R_{M2} distances. For both UiO-66¹⁸⁸ and UiO-67²⁰² cases, the failure of the XRPD model was overcome by using the optimized geometry obtained by ab initio periodic calculations.

The inorganic cornerstones of the as synthesized materials are perfect $M_6(OH)_4O_4$ octahedron (see model in Figure 17b), with 6 equivalent M at the vertex, 12 equivalent M-M1 sides and 3 equivalent and M-M2 diagonals. Upon desolvation 2 structural water molecules are lost per cornerstone unit (Figure 17a), that evolves from $M_6(OH)_4O_4$ to M_6O_6 .^{188,202,204,205} The new M_6O_6 octahedron compressed (2 opposite vertexes approaching, see model in Figure 17c) resulting in the shortening of 8 of the 12 edges, and the elongation of the other 4 edges. To take into account this variation we simulated the EXAFS contribution with two independently parameterized paths fixing for the degeneration a ratio of 1/3 and 2/3 with respect to the case of the single contribution. For the three systems, this combined XRPF, EXADS and DFT approach allowed a full interpretation of the EXAFS data in both hydroxylated and dehydroxylated forms.^{188,202,204,205} Please note that IR spectroscopy was determinant to confirm this model as allowed to observe the disappearance of the O-H stretching band in these materials, see also Section 2.3.3 of chapter⁶ in the present book.

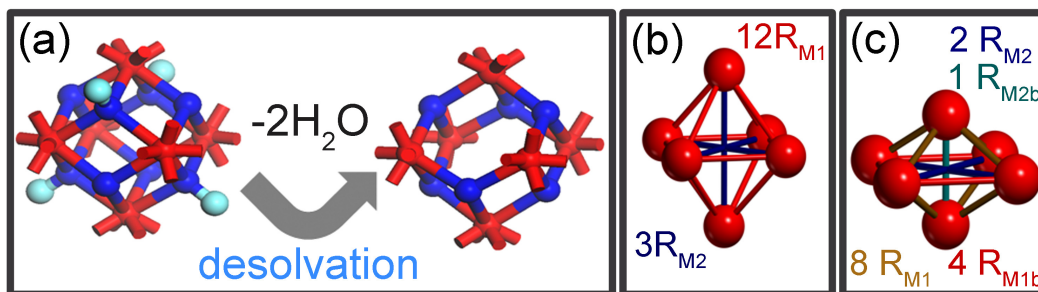


Figure 17. Part (a): Stick and ball representation of the dehydroxylation undergone by the inorganic $M_6O_4(OH)_4$ cornerstone upon thermal treatment at 300 °C in vacuo resulting in a distorted M_6O_6 cluster ($M = Zr$ or Hf). Red, blue and cyan colors refer to M, O and H atoms, respectively. Part (b): Stick and ball representation of the perfect M_6 octahedron, showing 12 equivalent R_{M1} sides and 3 equivalent $R_{M2} = \sqrt{2} R_{M1}$ diagonals. Part (c): Stick and ball representation of a squeezed M_6 octahedron. The 12 sides are now split into 4 in-plane long M_{M1b} sides and 8 prismatic short M_{M1a} sides, while the 3 diagonals evolve into 2 in-plane long M_{M2b} and 1 orthogonal short M_{M2a} diagonals. For clarity, O atoms are omitted in parts (b) and (c). Unpublished Figure reporting schemes published in Refs.^{188,202}

Table 4. Summary of the EXAFS refinement obtained on the hydroxylated and dehydroxylated forms of UiO-66, UiO-67 and Hf-UiO-66. Parameters without error bars were not optimized. The EXAFS refinement of the hydroxylated materials was obtained using as input model the optimized structure from Rietveld refinement of the corresponding XRPD patterns. The EXAFS refinement of the dehydroxylated materials was obtained using as input model optimized *ab initio* calculations for the hydroxylated of UiO-66. With this approach the coordination number (N) of each contribution is fixed by the model stoichiometry. Refinement of the experimental amplitude is done by optimizing the overall amplitude factor S_0^2 only. The fitting of the higher shells was possible only adopting the axial compressed model of the M_6O_6 octahedron represented where eight octahedron sides R_{M1} are split into eight short prismatic distances (R_{M1} , $N=8/3$) and four long planar ones (R_{M1b} , $N=4/3$) and where the three diagonals R_{M2} are split into a short axial diagonal and (R_{M2a} , involving two M atoms out of six; $N=1/3$) and two long planar diagonals (R_{M2b} , involving four M atoms out of six; $N=2/3$): Figure 17c. Unpublished table, reporting data from refs.^{188,201,202,204,205}

	UiO-66	Hydro UiO-67 hydroxylated	Hf-UiO-66	UiO-66	UiO-67 dehydroxylated	Hf-UiO-66
T (K)	300	300	300	300	300	573
R-factor	0.01	0.04	0.02	0.02	0.04	0.05
Δk (\AA^{-1})	2.0-18.0	2.0-16.2	2.0-16.0	2.0-15.0	2.0-15.0	2.0-15.0
ΔR (\AA)	1.0-5.3	1.0-5.3	1.0-5.5	1.0-5.3	1.0-5.3	1.0-3.9
Indip. points	43	38	40	35	35	25
N. variables	14	13	10	15	15	9
ΔE_0 (eV)	5 ± 1	1 ± 1	2.2 ± 0.6	5	1	2.4 ± 0.7
S_0^2	1.17 ± 0.08	1.17	0.91 ± 0.06	1.17	1.17	0.91
R_{μ_3-O} (\AA)	2.087 ± 0.008	2.12 ± 0.02	2.12 ± 0.01	2.06 ± 0.01	2.096 ± 0.007	2.06 ± 0.01
$\sigma^2(\mu_3-O)$ (\AA^2)	0.0036 ± 0.0009	0.005 ± 0.002	0.005 ± 0.002	0.008 ± 0.003	0.006 ± 0.001	0.009 ± 0.002
R_{O1} (\AA)	2.235 ± 0.008	2.26 ± 0.01	2.25 ± 0.01	2.221 ± 0.007	2.249 ± 0.007	2.19 ± 0.01
$\sigma^2(O1)$ (\AA^2)	0.0074 ± 0.0008	0.006 ± 0.001	0.005	0.007 ± 0.002	0.004 ± 0.001	0.009
R_C (\AA)	3.19 ± 0.02	3.40 ± 0.06	3.23 ± 0.06	3.17 ± 0.04	3.15 ± 0.04	3.22 ± 0.05
$\sigma^2(C)$ (\AA^2)	0.004 ± 0.002	0.012 ± 0.002	0.014 ± 0.011	0.009 ± 0.009	0.004 ± 0.003	0.016 ± 0.013
R_{M1} (\AA)	3.511 ± 0.007	3.512 ± 0.006	3.510 ± 0.005	3.35 ± 0.01	3.365 ± 0.015	3.31 ± 0.03
$\sigma^2(M1)$ (\AA^2)	0.007 ± 0.001	0.004 ± 0.001	0.0042 ± 0.0004	0.009 ± 0.001	0.009 ± 0.002	0.009 ± 0.004
R_{M1b} (\AA)	-	-	-	3.74 ± 0.02	3.80 ± 0.03	3.45 ± 0.06
$\sigma^2(M1b)$ (\AA^2)	-	-	-	0.009 ± 0.002	0.008 ± 0.003	0.009
R_{M2} (\AA)	4.99 ± 0.04	4.95 ± 0.03	4.964	4.14 ± 0.07	4.15 ± 0.07	-
$\sigma^2(M2)$ (\AA^2)	0.010 ± 0.006	0.004 ± 0.002	0.008 ± 0.002	0.008 ± 0.006	0.006 ± 0.004	-
R_{M2b} (\AA)	-	-	-	5.30 ± 0.04	5.46 ± 0.05	-
$\sigma^2(M2b)$ (\AA^2)	-	-	-	0.008	0.006	-

EXAFS spectroscopy allows to detect the evolution from $M_6(OH)_4O_4$ to M_6O_6 ($M = Zr$ or Hf) of the inorganic cornerstones of UiO-66, UiO-67 and Hf-UiO-66 MOFs occurring in the desolvation process, that

escaped XRPD detection. On Zr-UiO-66 and Zr-UiO-67, period calculations performed with CRYSTAL code²⁰⁶ at DFT level of theory support EXAFS data.

5.4. Molecular adsorption inside MOFs: determination of adsorption geometries by neutron diffraction

For the reasons outlined above (see Section 2.2 and in particular the discussions on Figure 9 and Table 2) neutron diffraction is an excellent structural technique to determine the location of adsorbed molecules (particularly deuterated ones) inside MOFs structures.²⁰⁷ In this regard, neutron diffraction is complementary to EXAFS (see Sections 5.2 and 5.3) in the determination of the molecular adsorption on the metal sites, with the additional advantage of being able to locate also the molecules adsorbed on the organic part of the framework.

Interesting results have been reported by several groups, among them, we mention the adsorption experiments of: D₂ on MOF-5,¹¹⁹ HKUST-1,²⁰⁸ ZIF-8,²⁰⁹ CPO-27-Zn,²¹⁰ Y(BTC)(H₂O)₄,²¹¹ and Cr MIL-53²¹² frameworks; of CD₄ in sodalite-type Mn-MOF,^{213,214} HKUST-1,²¹⁵ PCN-11,²¹⁵ PCN-14,²¹⁵ and CPO-27-M (M = Mg, Mn, Co, Ni, Zn)²¹⁶ frameworks; of O₂ on Cr₃(BTC)₂,¹⁴⁰ and CPO-27-Fe;²¹⁷ of N₂ on CPO-27-Fe;²¹⁷ and of CO₂ on CPO-27-Mg,²¹⁸ and HKUST-1.²¹⁸

The selected example to describe the potentialities of neutron diffraction versus X-ray diffraction is the study of O₂ loading on Cr₃(BTC)₂, the Cr²⁺ analogue of HKUST-1 MOF, reported by the group of Long in Berkley.¹⁴⁰ First these authors used neutron powder diffraction to prove that Cr₃(BTC)₂ crystallize in the same *Fm-3m* space group than the Cu²⁺-homologue,²¹⁹ see Figure 18a (compare top and bottom patterns collected for the desolvated materials). Insertion of Cr²⁺, substituting Cu²⁺, implies a small cell expansion from $a = 26.2243(5) \text{ \AA}$, $V = 18035(1) \text{ \AA}^3$ of HKUST-1 to $a = 26.6652(3) \text{ \AA}$, $V = 18959.8(6) \text{ \AA}^3$ of Cr₃(BTC)₂, that is accompanied by a significant shrinking of the metal-metal distance in the dimer from $R_{\text{Cu-Cu}} = 2.50 \pm 0.02 \text{ \AA}$, see Ref.,¹⁹ $R_{\text{Cr-Cr}} = 2.06 \pm 0.02 \text{ \AA}$.¹⁴⁰ The impressive change in structure of the [Cr₂C₄O₈] cages is as expected since Cr²⁺ centers can form a strong (quadruple) metal-metal bond upon loss of the axial solvent²²⁰ whereas Cu²⁺ does not. The neutron diffraction data were definitive on this point.¹⁴⁰ The data collection was done with $\lambda = 2.0785 \text{ \AA}$ up to a $2\theta_{\text{max}} = 140^\circ$, where Bragg peaks were clearly present, resulting in a $d_{\text{min}} = 1.11 \text{ \AA}$ or a $q_{\text{max}} = 5.68 \text{ \AA}^{-1}$, see Eq. (23). In this regard, comparison between parts (a) and (b) of Figure 18 is striking in terms of the higher potentiality of neutrons with respect to X-rays in obtaining high signal to noise data for the high 2θ Bragg peaks.

The interest aspect of this new Cr₃(BTC)₂ MOF material is that it is able fix O₂ molecules from air with high selectivity and in a reversible way.¹⁴⁰ This peculiarity is relevant because the separation of O₂ from air is carried out in industry using cryogenic distillation on a scale of 100 Mtons/year, as well as using zeolites in portable devices for medical applications. Moreover, in the next future O₂ may be needed in large scale for CO₂-free energy production inside fuel cells. Thus, there is a clear benefit to developing materials that might enable this process to be carried out with a lower energy cost.

Long et al.¹⁴⁰ followed the interaction of Cr₃(BTC)₂ with O₂ by neutron powder diffraction, collected at 4 K, IR, UV-Vis-NIR and XANES spectroscopies. Neutron powder diffraction revealed a decrease of the unit cell from $a = 26.6652(3) \text{ \AA}$, $V = 18959.8(6) \text{ \AA}^3$ to $a = 25.956(2) \text{ \AA}$, $V = 17487(4) \text{ \AA}^3$, accompanied by an impressive elongation of the distance in the dimer, that moves from $R_{\text{Cr-Cr}} = 2.06 \pm 0.02 \text{ \AA}$ to $R_{\text{Cr-Cr}} = 2.8 \pm 0.1 \text{ \AA}$ (Figure 18c). The Rietveld refinement afforded a model in which 0.87(3) O₂ molecules are coordinated to the axial sites of each paddle-wheel unit (Figure 18d), while 0.197(7) occupy the smallest pore openings within the framework (middle structure in Figure 18d). Authors concluded that, although the resolution of the data was insufficient to determine the orientation of O₂, the observed metal-centroid distance, $R_{\text{Cr-O2}} = 1.97(5) \text{ \AA}$, is consistent with a side-on coordination mode.

In Table 5 structural data on desolvated and on O₂-interacting Cr₃(BTC)₂ are summarized and compared with similar data obtained on the isostructural Cu₃(BTC)₂, i.e. HKUST-1, in its

dehydrated form and after interaction with H₂O or NH₃ ligands. The removal of the water molecule coordinated to Cu²⁺ during the desolvation process in Cu₃(BTC)₂ results in a small contraction of the unit cell $\Delta a/a = -0.5\%$ that is accompanied by an important shrinking of the [Cu₂C₄O₈] cage of $R_{\text{Cu-Cu}} / R_{\text{Cu-Cu}} = -5.0\%$. It is interesting to underline how Cr₃(BTC)₂, behaves differently when the coordinated O₂ molecule is removed from the Cr²⁺ site: the MOF lattice undergoes a much larger contraction $\Delta a/a = -2.7\%$, that is however accompanied by a huge deformation of the [Cr₂C₄O₈] cage opposite to what observed for the Cu²⁺-homologue MOF, of $R_{\text{Cr-Cr}}/R_{\text{Cr-Cr}} = +35\%$. Such impressive behaviour can be explained only on the basis of an extremely high flexibility of the [Cr₂C₄O₈] cage. Structural values on the effect of molecular adsorption (H₂O, NH₃ or O₂) on the two isostructural systems are summarized in Table 5.

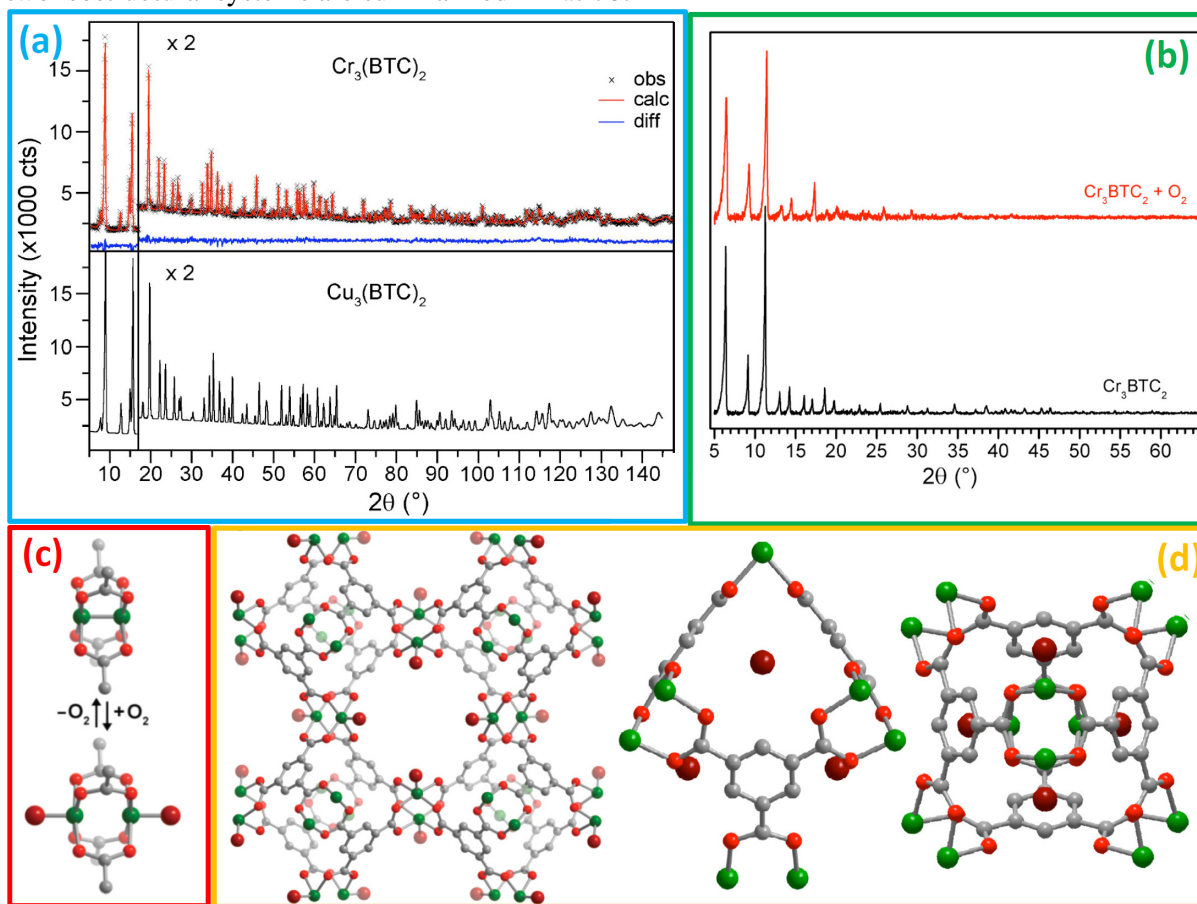


Figure 18. Part (a) top: neutron powder diffraction pattern of desolvated Cr₃(BTC)₂ MOF (× symbols) Rietveld refinement (red curve) and residual (blue curve). Panel (a) bottom: neutron powder diffraction pattern of desolvated Cu₃(BTC)₂ MOF (black curve). Data have been collected on the high resolution BT-1 diffractometer at the NIST Centre for Neutron Research (US) with $\lambda = 2.0785$ Å. Panel (b): XRPD pattern of desolvated Cr₃(BTC)₂ MOF before (black curve) and after (red curve) O₂ dosage. $\lambda = 1.54$ Å. Part (c): modification of the [Cu₂C₄O₈] cage upon O₂ coordination. Note that O₂ absorption causes an increase of the Cr–Cr distance 2.06(2) to 2.8(1) Å. Part (d): different views of the structure of the O₂ loaded Cr₃(BTC)₂ as refined from the neutron powder diffraction. In parts (c) and (d) green, red, and grey spheres represent Cr, O, and C framework atoms, respectively, while large red spheres represent the centroid of the bound O₂ molecules. Reproduced with permission from ref.¹⁴⁰ (copyright American Chemical Society 2010).

It is finally worth recalling that to evaluate possible oxidation state changes of Cr upon oxygenation of the activated framework, Long et al.¹⁴⁰ have collected the Cr K-edge XANES spectra (see the corresponding chapter,⁶ this book) of the as prepared, desolvated and O₂-contacted material. They concluded that the observed shift was consistent with partial charge transfer from the Cr metal center to the bound O₂ molecule.

Table 5. Summary on the structural data of isostructural $\text{Cu}_3(\text{BTC})_2$, i.e. HKUST-1, and $\text{Cu}_3(\text{BTC})_2$ obtained with different techniques. M = Cu or Cr. Unpublished Table reporting data published in quoted Refs.

Material	coordination on M site	a (Å)	V (Å ³)	$R_{\text{M-M}}$ (Å)	$R_{\text{M-adsorbate}}$
$\text{Cu}_3(\text{BTC})_2$	H_2O	26.343(5) ^a	18280(7) ^a	2.628(2) ^a ; 2.64(2) ^b ; 2.65(2) ^d	2.19(2) ^b ; 2.24(3) ^d
$\text{Cu}_3(\text{BTC})_2$	-	26.2243(5) ^c	18035(1) ^c	2.50(2) ^b ; 2.58(2) ^d	-
$\text{Cu}_3(\text{BTC})_2$	NH_3	-	-	2.80(3) ^d	2.31(1) ^d
$\text{Cr}_3(\text{BTC})_2$	-	26.6652(3) ^e	18959.8(6) ^e	2.06(2) ^e	-
$\text{Cr}_3(\text{BTC})_2$	O_2	25.956(2) ^e	17487(4) ^e	2.8(1) ^e	1.97(5) ^e

^a Single crystal X-ray diffraction;²¹⁹ ^b Cu K-edge EXAFS;¹⁹ ^c XRPD;¹⁹ ^d Cu K-edge EXAFS;²²¹ ^e neutron powder diffraction.¹⁴⁰

5.5. Trapping guest molecules within Nanoporous MOFs through pressure-induced amorphization: a PDF approach

The final section of this chapter is devoted to discuss the potentialities of the total scattering, or PDF, approach. The peculiarity of the PDF approach is to provide a local range structural information based on the X-ray (neutron) scattering process (see Section 4), that makes PDF intermediate between EXAFS and X-ray (neutron) diffraction choices in terms of local vs. long range order of materials. Concerning the application of the technique to the structural determination of MOFs materials, PDF certainly represents an ideal complementary technique to support diffraction data (as is the case for EXAFS discussed in sections 5.1-5.3); it is however evident that its peculiarity becomes essential in the study of processes that imply a partial or total amorphization of the framework.

The example selected to show the potentialities of the PDF approach is the work of Chapman et al.^{222,223} who investigated the impact of modest, industrially accessible pressures (~ 1 GPa) on the structure and porosity of $\text{Zn}(\text{2-methylimidazole})_2$ (ZIF-8),^{224,225} a high-surface area MOF with expanded zeolite topologies where the bidentate imidazolate-based ligand replicates the characteristic T-O-T angle of zeolites. The topology of ZIF-8, with imidazolate-bridged zinc tetrahedra, corresponds to the one of the high symmetry sodalite zeolite. The cubic framework ($I\bar{4}3m$ space group with $a \sim 17.0$ Å) can be described by a space-filling packing of regular truncated octahedra, defining 12.0 Å diameter pores connected via 3.5 Å diameter apertures (6-rings), with the 4-rings being too small to transmit guests (see Figure 19a). In a first work, Chapman et al.²²² have demonstrated that ZIF-8 exhibits an irreversible pressure-induced amorphization, which starts at moderate pressures (see Figure 19b). Authors succeeded in the generation of a new type of non-crystalline MOF still exhibiting nanoporosity, that has been modified with respect to that of the pristine crystalline phase as proven by the differences in the absorption/desorption of nitrogen²²² and iodine²²³ molecules. In particular, the TGA curves reported in Figure 19a, show how the retention of I_2 is enhanced in the amorphized ZIF-8 compared to the crystalline one. The mass losses were shifted to higher temperatures for the amorphized materials, by up to 150 °C. These gains were most pronounced for the intermediate I_2 loadings. The retained nanoporosity property of the amorphous phase is a consequence of the fact that the structure retained some structural order after the amorphization process. In a successive work, these authors decided to use the PDF approach to investigate such structural order.²²³

The well-defined long-range correlations, evident in PDFs for the crystalline materials, are absent for the amorphized ZIF-8 systems (Figure 19d). However, the shorter range features, including those up to 6 Å, which correspond to the Zn-imidazolate-Zn links, are entirely preserved in the amorphous materials. The combined retention of guests, porosity, and the Zn...Zn' connectivity in the pressure-amorphized materials suggests that the sodalite topology of ZIF-8 is preserved, despite the local structural changes responsible of destroying the long-range order, that is, the crystallinity. Authors concluded that structural changes are likely to involve symmetry-reducing distortions of the 6-ring apertures, eliminating the well-defined features in the PDF beyond ~6 Å and hampering diffusion of guest molecules through the framework.²²³ While the long-range framework order is

eliminated upon amorphization, the short-range I–I and I–framework interactions remain unchanged. Indeed, a larger change in local structure is associated with the annealing and surface-desorption compared to the amorphization itself (Figure 19e). Specifically, the nearest neighbor I–I peak shifts from 2.8 to 2.6 Å while simultaneously narrowing, indicating less disorder (dynamic or static). This is accompanied by an increase in the relative intensity of the second and third peaks at 3.85 and 4.3–4.4 Å, associated with intermolecular interactions within pores (Figure 19e). These changes reflect a refinement of the I₂ arrangement within the pores upon annealing, that enhances the retention of I₂ by the framework as documented by the TGA curves reported in Figure 19c.

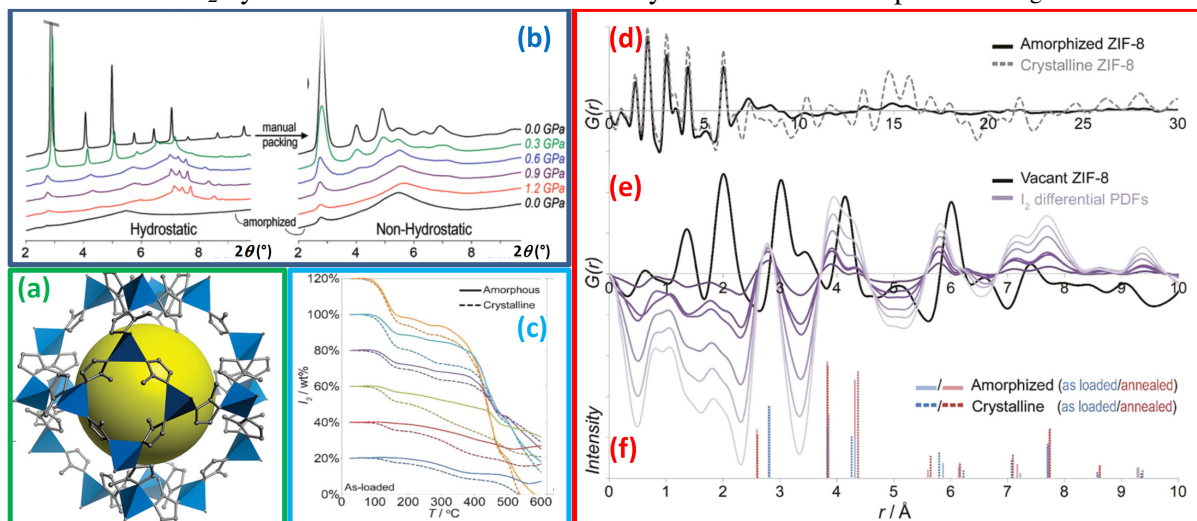


Figure 19. Part (a): representation of the ZIF-8 structure, showing the 12 Å pores. Part (b): XRPD data, collected with $\lambda = 0.60511$ Å at the 1-BM beamline at the APS synchrotron (Argonne, IL, USA), showing irreversible amorphization of the ZIF-8 framework under both hydrostatic (left) and non-hydrostatic (right) compressions (1 Atm = 1.01×10^5 Pa). Part (c) TGA curves reporting the differences between crystalline (dashed curves) and amorphized (continuous curves) ZIF-8 materials during the I₂ release process for different I₂ starting. The mass losses for the vacant ZIF-8 materials have been subtracted to the reported curves. Part (d): Representative PDFs, $G(r)$, for the crystalline and amorphous materials. Part (e): differential PDFs corresponding to I–I and I–framework interactions in the pressure-amorphized as-loaded series (120 wt % loading). Part (f): intensity and position of features in differential PDFs for crystalline and amorphous, and as-loaded and annealed samples. Parts (a),(b) Reproduced with permission from Ref.²²² (copyright 2009, American Chemical Society). Parts (c)-(f) Reproduced with permission from Ref.²²³ (copyright 2011, American Chemical Society).

We briefly close this section mentioning two additional examples of the use of a PDF analysis in the understanding of the structure of complex MOFs. The first example comes from the group of Hupp,²²⁶ who recently reported on the synthesis of a new, twofold interpenetrated framework that demonstrate an impressive steps in the adsorption and hysteresis in the desorption of CO₂. Combining XRPD with PDF analyses, authors were able to demonstrate that the remarkable structural changes undergone by the framework upon CO₂ sorption involve the interpenetrated frameworks that move with respect to each other.²²⁶

The second example comes from the Cheetham group.¹¹⁴ Authors have followed the reversible amorphization processes undergone by ZIF-4 MOF upon heating to 300 °C by neutron and X-ray total scattering. The collected high q -data were used as a basis for reverse Monte Carlo refinement of an atomistic model of the structure of a-ZIF. Authors were able to describe the amorphous structure in terms of a continuous random network analogous to that of *a*-SiO₂.¹¹⁴ On top of this, optical microscopy, electron diffraction and nanoindentation measurements reveal amorphous ZIF phase to be an isotropic glasslike phase capable of plastic flow on its formation. Authors conclude suggesting the possibility to design broad new families of amorphous and glasslike materials that exploit the chemical and structural diversity of MOFs.¹¹⁴

6. Conclusions and Perspectives

From the case studies reported in this chapter it becomes evident that besides the unavoidable standard laboratory XRPD investigation, the possibility to extend the structural characterization to *less common* techniques such as neutron powder diffraction, metal K-or L-edges EXAFS and neutrons or X-rays PDF will allow to better characterize complex materials such as MOFs are. Such information should be coupled with a spectroscopic investigation of the vibrational and electronic properties of the material.⁶ Finally, the presence in the group of competencies in computational chemistry²²⁷ is highly recommended as quantum mechanics will allow to verify the stability of the structures inferred from Rietveld refinement.

Acknowledgements

We are deeply indebted with F. Camara (Department of Earth Science University of Turin, Italy) for the long and constructive discussions that contributed to a significant improvement of the contents of this chapter. F. Camara and M. Ceretti (Institut de Chimie Moléculaire et des Matériaux Université de Montpellier 2, France) are acknowledged for a critical lecture of the manuscript. M. Ceretti is also acknowledged for providing the neutron powder diffractograms reported in Figure 8b. We thank A. Piovano (ILL, Grenoble, France) for computing the neutron and X-ray simulated patterns reported in Figure 8a. Finally, CL and EB are grateful to the students of the *Advanced Crystallography* class of the MaMaSELF European Master in Materials Science²²⁸ that have contributed to found several typos in a first draft of Sections 1-4 used as lecture notes.

References and Notes.

- 1 P. E. Werner, L. Eriksson and M. Westdahl, *J. Appl. Crystallogr.*, 1985, **18**, 367.
- 2 A. Altomare, C. Giacovazzo, A. Guagliardi, A. G. G. Moliterni and R. Rizzi, *J. Appl. Crystallogr.*, 2000, **33**, 1305.
- 3 A. Altomare, C. Giacovazzo, A. Guagliardi, A. G. G. Moliterni, R. Rizzi and P. E. Werner, *J. Appl. Crystallogr.*, 2000, **33**, 1180.
- 4 C. Giacovazzo, A. Altomare, C. Cuocci, A. G. G. Moliterni and R. Rizzi, *J. Appl. Crystallogr.*, 2002, **35**, 422.
- 5 A. Altomare, R. Caliendo, M. Camalli, C. Cuocci, I. da Silva, C. Giacovazzo, A. G. G. Moliterni and R. Spagna, *J. Appl. Crystallogr.*, 2004, **37**, 957.
- 6 F. Bonino, C. Lamberti, S. Chavan, J. G. Vitillo and S. Bordiga, *Characterization of MOFs by combined vibrational, and electronic spectroscopies*, in: Metal-Organic Frameworks in heterogeneous catalysis; F. X. Llabrés i Xamena and J. Gascón, Ed.; RSC: Cambridge, **2013**.
- 7 E. Pidko, *Computational methods: DFT*, in: Metal-Organic Frameworks in heterogeneous catalysis; F. X. Llabrés i Xamena and J. Gascón, Ed.; RSC: Cambridge, **2013**.
- 8 I. Waller, *Phil. Mag.*, 1927, **4**, 1228.
- 9 I. Waller, *Nature*, 1927, **120**, 155.
- 10 G. Wentzel, *Zeit. f. Physik.*, 1927, **43**, 1.
- 11 I. Waller, *Zeit. f. Physik.*, 1928, **51**, 213.
- 12 R. W. James, *The Optical Principles of the Diffraction of x-rays*; G. Bell and Sons Ltd., **1948**.
- 13 A. Guinier, *X-ray Diffraction*; Dover: New York, US, **1963**.
- 14 B. E. Warren, *X-ray Diffraction*; Dover: New York, **1969**.
- 15 C. Giacovazzo, *Direct Phasing in Crystallography: Fundamentals and Applications*; Oxford University Press: Oxford, **1998**; Vol. 8.
- 16 The Euler's formula teaches us that the exponential of a pure imaginary argument is a periodic function in both its real and imaginary parts: $\exp(ix) = \cos(x) + i \sin(x)$.
- 17 R. Shannon, *Acta Cryst. A*, 1976, **32**, 751.
- 18 Note that $\rho(-\mathbf{r}) = \rho(\mathbf{r})$ is no more fully true when the atom will be part of a molecule or embedded inside a crystal as the formation of chemical bonds breaks the spherical symmetry.
- 19 C. Prestipino, L. Regli, J. G. Vitillo, F. Bonino, A. Damin, C. Lamberti, A. Zecchina, P. L. Solari, K. O. Kongshaug and S. Bordiga, *Chem. Mater.*, 2006, **18**, 1337.
- 20 J. C. Slater, *Phys. Rev.*, 1930, **36**, 57.
- 21 E. Clementi and D. L. Raimondi, *J. Chem. Phys.*, 1963, **38**, 2686.
- 22 E. Clementi, D. L. Raimondi and W. P. Reinhardt, *J. Chem. Phys.*, 1967, **47**, 1300.
- 23 E. Clementi and C. Roetti, *Atom. Data Nucl. Data Tables*, 1974, **14**, 177.
- 24 T. Koga, H. Tatewaki and A. J. Thakkar, *Phys. Rev. A*, 1993, **47**, 4510.
- 25 T. K. Ghanty and S. K. Ghosh, *J. Phys. Chem.*, 1996, **100**, 17429.
- 26 D. T. Cromer and J. T. Waber, *Acta Cryst.*, 1965, **18**, 104.

- 27 P. A. Doyle and P. S. Turner, *Acta Crystallogr. A*, 1968, **24**, 390.
- 28 D. T. Cromer and J. B. Mann, *Acta Crystallogr. A*, 1968, **24**, 321.
- 29 D. T. Cromer and J. T. Waber, *Mean atomic scattering factors in electrons for free atoms and chemically significant ions. in International Tables for X-ray Crystallography, Volume IV*; Kynock Press: Birmingham, **1974**.
- 30 A. G. Fox, M. A. O'Keefe and M. A. Tabbernor, *Acta Crystallogr. A*, 1989, **45**, 786.
- 31 P. J. Brown, A. G. Fox, E. N. Maslen, M. A. O'Keefe and B. T. M. Willis, *Intensity of diffracted intensities*, in: *International Tables for Crystallography* E. Prince, Ed.; International Union of Crystallography: on-line edition, **2006**; Vol. C, p. 554.
- 32 E. N. Maslen, A. G. Fox and M. A. O'Keefe, *X-ray Scattering*, in: *International Tables for Crystallography*; E. Prince, Ed.; Kluwer Academic: Dordrecht, **2004**; Vol. C, p. 554.
- 33 R. N. Bracewell, *The Fourier Transform and Its Applications, 3rd Edition* McGraw-Hill: New York, **1999**.
- 34 G. Portale and A. Longo, *Small Angle X-ray scattering for the study of nanostructures and nanostructured materials*, in: *Characterization of Semiconductor Heterostructures and Nanostructures (II Ed.)*; C. Lamberti and G. Agostini, Ed.; Elsevier: Amsterdam, **2013**, p. 289.
- 35 J. L. Hodeau, V. Favre-Nicolin, S. Bos, H. Renevier, E. Lorenzo and J. F. Berar, *Chem. Rev.*, 2001, **101**, 1843.
- 36 W. Friedrich, P. Knipping and M. von Laue, *Bayerische Akademie der Wissenschaften*, 1912, 303.
- 37 H. Ihee, *Acc. Chem. Res.*, 2009, **42**, 356.
- 38 C. Kittel, *Introduction to Solid State Physics*, in; John Wiley & Sons, **2004**, p. Chapter 2.
- 39 W. L. Bragg, *Proc. Cambridge Phil. Soc.*, 1913, **17**, 43–57.
- 40 W. H. Bragg and W. L. Bragg, *Proc. R. Soc. Lond. A*, 1913, **88**, 428.
- 41 W. H. Bragg, *Proc. R. Soc. Lond. A*, 1913, **89**, 246.
- 42 J. R. Helliwell, A. J. Blake, J. Blunden-Ellis, M. Moore and C. H. Schwalbe, *Crystallogr. Rev*, 2012, **18**, 3.
- 43 J. R. Helliwell, *Crystallogr. Rev*, 2012, **18**, 280.
- 44 T. Cormen, H., C. E. Leiserson, R. L. Rivest and C. Stein, *Introduction to Algorithms (3rd ed.)*; MIT Press and McGraw-Hill: Boston (section 30.2: The DFT and FFT pp. 906-914), **2009**.
- 45 D. J. Tranchemontagne, J. L. Mendoza-Cortes, M. O'Keefe and O. M. Yaghi, *Chem. Soc. Rev.*, 2009, **38**, 1257.
- 46 A. Bacchi, M. Carcelli and P. Pelagatti, *Crystallogr. Rev*, 2012, **18**, 253.
- 47 A. K. Cheetham and A. P. Wilkinson, *Angew. Chem.-Int. Edit. Engl.*, 1992, **31**, 1557.
- 48 R. J. Harrison, *Rev. Mineral. Geochem.*, 2006, **63**, 113.
- 49 J. R. Helliwell, *Crystallogr. Rev*, 2012, **18**, 33.
- 50 E. Aubert and C. Lecomte, *J. Appl. Cryst.*, 2007, **40**, 1153.
- 51 A. L. Patterson, *Phys. Rev.*, 1934, **46**, 372.
- 52 A. L. Patterson, *Z. Kristallogr.*, 1934, **90**, 517.
- 53 M. G. Rossmann and E. Arnold, *Patterson and molecular-replacement techniques*, in: *International Tables for Crystallography*, **2006**; Vol. B, p. 235.
- 54 M. G. Rossmann and D. M. Blow, *Acta Cryst.*, 1962, **15**, 24.
- 55 W. A. Hendrickson, *Science*, 1991, **254**, 51.
- 56 S. E. Ealick, *Curr. Opin. Chem. Biol.*, 2000, **4**, 495.
- 57 J. L. Smith, W. A. Hendrickson, T. T. C. and J. Berendzen, *MAD and MIR*, in: *International Tables for Crystallography* **2006**; Vol. F, p. 299.
- 58 G. Oszlanyi and A. Suto, *Acta Crystallogr. Sect. A*, 2008, **64**, 123.
- 59 D. E. Sands, *Introduction to Crystallography*; Dover Publications: New York, **1994**.
- 60 M. F. C. Ladd and R. A. Palmer, *Structure Determination by X-Ray Crystallography*; Kluwer Academic/Plenum Publishers: New York, **2003**.
- 61 G. Taylor, *Acta Crystallogr. D*, 2003, **59**, 1881.
- 62 C. C. Wilson, *Crystallogr. Rev*, 2009, **15**, 3.
- 63 P. Debye, *Ann. Phys.*, 1913, **348**, 49.
- 64 I. Waller, *Z. Phys.*, 1923, **17**, 398.
- 65 W. Massa, *Crystal Structure Determination*; Springer-Verlag: Berlin, **2004**.
- 66 G. S. Matouzenko, E. Jeanneau, A. Y. Verat and A. Bousseksou, *Dalton Trans.*, 2011, **40**, 9608.
- 67 G. A. Martynov, *J. Mol. Liq.*, 2003, **106**, 123.
- 68 P. Debye, *Ann. der Physik*, 1915, **46**, 809.
- 69 J. G. Kirkwood and E. M. Boggs, *J. Chem. Phys.*, 1942, **10**, 394.
- 70 B. R. A. Nijboer and L. Van Hove, *Phys. Rev.*, 1952, **85**, 777.
- 71 B. Widom, *J. Chem. Phys.*, 1964, **41**, 74.
- 72 O. Glatter and O. Kratky, *Small angle x-ray scattering*; Academic Press: London, **1982**.
- 73 L. A. Feigin and D. I. Svergun, *Structure analysis by small angle X-ray and neutron scattering*; Plenum Press: New York, **1987**.
- 74 E. S. Bozin, P. Juhás and S. J. L. Billinge, *Local structure of bulk and nanocrystalline semiconductors using total scattering method*, in: *Characterization of Semiconductor Heterostructures and Nanostructures (II Ed.)*; C. Lamberti and G. Agostini, Ed.; Elsevier: Amsterdam, **2013**, p. 289.

- 75 C. S. Tsao, M. S. Yu, T. Y. Chung, H. C. Wu, C. Y. Wang, K. S. Chang and H. L. Chent, *J. Am. Chem. Soc.*, 2007, **129**, 15997.
- 76 S. H. Yeon, S. Osswald, Y. Gogotsi, J. P. Singer, J. M. Simmons, J. E. Fischer, M. A. Lillo-Rodenas and A. Linares-Solanod, *J. Power Sources*, 2009, **191**, 560.
- 77 M. Klimakow, P. Klobes, A. F. Thunemann, K. Rademann and F. Emmerling, *Chem. Mat.*, 2010, **22**, 5216.
- 78 C. S. Tsao, C. Y. Chen, T. Y. Chung, C. J. Su, C. H. Su, H. L. Chen, U. S. Jeng, M. S. Yu, P. Y. Liao, K. F. Lin and Y. R. Tzeng, *J. Phys. Chem. C*, 2010, **114**, 7014.
- 79 J. Juan-Alcaniz, M. Goesten, A. Martinez-Joaristi, E. Stavitski, A. V. Petukhov, J. Gascon and F. Kapteijn, *Chem. Commun.*, 2011, **47**, 8578.
- 80 A. Mallick, E. M. Schon, T. Panda, K. Sreenivas, D. D. Diaz and R. Banerjee, *J. Mater. Chem.*, 2012, **22**, 14951.
- 81 L. de Broglie, *Ann. Phys. (Paris)*, 1925, **2**, 22.
- 82 Relativistic corrections can no more be neglected for when working with SEM or TEM machines. In a TEM working at 300 keV, the relativistic corrected de Broglie wavelength is 0.0197 Å, while a value 0.0223 Å results adopting the $\lambda=h/(mv)$ equation. See e.g. D. B. Williams and C. B. Carter, *Transmission Electron Microscopy*, Plenum, New York, 1996; M. De Graef, *Introduction to Conventional Transmission Electron Microscopy*, Cambridge University Press, Cambridge 2003.
- 83 M. Siegbahn, *Phil. Mag.*, 1919, **37**, 601.
- 84 The Davisson and Germer experiment consisted of firing an electron beam from an electron gun perpendicular to the Ni(111) phase. As the potential V was fixed, then the energy of the electrons (eV) was fixed, and so the de Broglie wavelength. The experiment included an electron gun consisting of a heated filament that released thermally excited electrons, which were then accelerated through a potential difference V giving them a defined kinetic energy ($E = eV$) towards the nickel crystal. To avoid collisions of the electrons with other molecules on their way towards the surface, the experiment was obviously conducted in a vacuum chamber. To measure the number of electrons that were scattered at different angles, an electron detector that could be moved on an arc path about the crystal was used. The detector was designed to accept only elastically scattered electrons. When the electrons hit the surface, they were scattered by atoms which originated from crystal planes inside the nickel crystal at precise angular positions that were in agreement with the Bragg law previously demonstrated for X-rays. When the voltage was changed from 54 to 174 V, the angular position where scattered electrons were observed changed according to the electron wavelength change foreseen by de Broglie Equation.
- 85 G. P. Thomson and A. Reid, *Nature*, 1927, **119**, 890.
- 86 G. P. Thomson, *Nature*, 1927, **120**, 802.
- 87 G. P. Thomson, *Proc. R. Soc. Lond. A*, 1928, **117**, 600.
- 88 G. P. Thomson, *Proc. R. Soc. Lond. A*, 1928, **119**, 651.
- 89 G. P. Thomson, *Proc. R. Soc. Lond. A*, 1929, **125**, 651.
- 90 G. P. Thomson, *Am. J. Phys.*, 1961, **29**, 821.
- 91 G. P. Thomson, *Contemporary Phys.*, 1968, **9**, 1.
- 92 J. Chadwick, *Nature*, 1932, **129**, 312.
- 93 J. Chadwick, *Proc. R. Soc. Lond. A*, 1932, **136**, 692.
- 94 J. Chadwick, *Proc. R. Soc. Lond. A*, 1933, **142**, 1.
- 95 C. G. Shull, *Rev. Mod. Phys.*, 1995, **67**, 753.
- 96 E. O. Wollan, C. G. Shull and M. C. Marney, *Phys. Rev.*, 1948, **73**, 527.
- 97 C. G. Shull, E. O. Wollan, G. A. Morton and W. L. Davidson, *Phys. Rev.*, 1948, **73**, 842.
- 98 E. O. Wollan and C. G. Shull, *Phys. Rev.*, 1948, **73**, 830.
- 99 E. O. Wollan, W. L. Davidson and C. G. Shull, *Phys. Rev.*, 1949, **75**, 1348.
- 100 W. C. Koehler, E. O. Wollan and C. G. Shull, *Phys. Rev.*, 1950, **79**, 395.
- 101 C. G. Shull, E. O. Wollan and W. A. Strauser, *Phys. Rev.*, 1951, **81**, 483.
- 102 C. G. Shull, E. O. Wollan and W. C. Koehler, *Phys. Rev.*, 1951, **84**, 912.
- 103 C. G. Shull and E. O. Wollan, *Phys. Rev.*, 1951, **81**, 527.
- 104 E. Fermi and L. Marshall, *Phys. Rev.*, 1947, **71**, 666.
- 105 E. Fermi and L. Marshall, *Phys. Rev.*, 1947, **71**, 915.
- 106 E. Fermi, W. J. Sturm and R. G. Sachs, *Phys. Rev.*, 1947, **71**, 589.
- 107 E. Fermi and L. Marshall, *Phys. Rev.*, 1947, **72**, 408.
- 108 R. J. T. Houk, B. W. Jacobs, F. El Gabaly, N. N. Chang, A. A. Talin, D. D. Graham, S. D. House, I. M. Robertson and M. D. Allendorf, *Nano Lett.*, 2009, **9**, 3413.
- 109 H. F. Greer and W. Z. Zhou, *Crystallogr. Rev.*, 2011, **17**, 163.
- 110 C. Wiktor, S. Turner, D. Zacher, R. A. Fischer and G. Van Tendeloo, *Microporous Mesoporous Mat.*, 2012, **162**, 131.
- 111 O. I. Lebedev, F. Millange, C. Serre, G. Van Tendeloo and G. Ferey, *Chem. Mat.*, 2005, **17**, 6525.
- 112 J. Cravillon, S. Munzer, S. J. Lohmeier, A. Feldhoff, K. Huber and M. Wiebcke, *Chem. Mat.*, 2009, **21**, 1410.
- 113 M. Yamada and S. Yonekura, *J. Phys. Chem. C*, 2009, **113**, 21531.
- 114 T. D. Bennett, A. L. Goodwin, M. T. Dove, D. A. Keen, M. G. Tucker, E. R. Barney, A. K. Soper, E. G. Bithell, J. C. Tan and A. K. Cheetham, *Phys. Rev. Lett.*, 2010, **104**, Art. n. 115503.

- 115 J. Hermannsdorfer and R. Kempe, *Chem.-Eur. J.*, 2011, **17**, 8071.
- 116 L. H. Schwartz and J. B. Cohen, *Diffraction from Materials*; Academic Press: New York, **1977**.
- 117 S. W. Lovesey, *Theory of Neutron Scattering from Condensed Matter; Volume 1: Neutron Scattering*; Clarendon Press: Oxford, **1984**.
- 118 V. F. Sears, *Neutron News*, 1992, **3/3**, 26.
- 119 T. Yildirim and M. R. Hartman, *Phys. Rev. Lett.*, 2005, **95**, 215504.
- 120 P. Atkins, *Physical Chemistry 3rd Edition* Oxford University Press: Oxford, **1986**.
- 121 E. Suard and A. Hewat, *Neutron News*, 2001, **12(4)**, 30.
- 122 E. Steichele and P. Arnold, *Phys. Lett. A*, 1973, **44**, 165.
- 123 R. M. Ibberson, *Nucl. Instrum. Methods Phys. Res. Sect. A*, 2009, **600**, 47.
- 124 A. N. Fitch, *Nucl. Instrum. Methods Phys. Res. Sect. B*, 1995, **97**, 63.
- 125 A. N. Fitch, *J. Res. Natl. Inst. Stand. Technol.*, 2004, **109**, 133.
- 126 D. R. Sandstrom and F. W. Lytle, *Ann. Rev. Phys. Chem.*, 1979, **30**, 215.
- 127 P. A. Lee, P. H. Citrin, P. Eisenberger and M. Kincaid, *Rev. Mod. Phys.*, 1981, **53**, 769.
- 128 E. A. Stern, *Theory of EXAFS*, in: X-Ray Absorption: Principles, Applications, Techniques of EXAFS, SEXAFS and XANES; D. C. Koningsberger and R. Prins, Ed.; John Wiley & Sons: New York, **1988**; Vol. 92, p. 3.
- 129 A. Filipponi, A. Di Cicco and C. R. Natoli, *Phys. Rev. B*, 1995, **52**, 15122.
- 130 A. Filipponi and A. Di Cicco, *Phys. Rev. B*, 1995, **52**, 15135.
- 131 J. J. Rehr and R. C. Albers, *Rev. Mod. Phys.*, 2000, **72**, 621.
- 132 F. Boscherini, *X-ray absorption fine structure in the study of semiconductor heterostructures and nanostructures*, in: Characterization of Semiconductor Heterostructures and Nanostructures; C. Lamberti, Ed.; Elsevier: Amsterdam, **2008**, p. 289.
- 133 S. Bordiga, E. Groppo, G. Agostini, J. A. van Bokhoven and C. Lamberti, *Chem. Rev.*, 2013, **113**, dx.doi.org/10.1021/cr2000898.
- 134 P. A. M. Dirac, *Proc. Roy. Soc. (London) A*, 1927, **114**, 243.
- 135 E. Fermi, *Nuclear Physics*; University of Chicago Press: Chicago, **1950**.
- 136 B. K. Teo and D. C. Joy, *EXAFS Spectroscopy: Techniques and Applications* Plenum: New York, **1981**.
- 137 E. Borfecchia, C. Garino, L. Salassa and C. Lamberti, *Phil. Trans. R. Soc. A*, 2013, in press.
- 138 D. E. Sayers, E. A. Stern and F. W. Lytle, *Phys. Rev. Lett.*, 1971, **27**, 1204.
- 139 F. W. Lytle, D. E. Sayers and E. A. Stern, *Phys. Rev. B*, 1975, **11**, 4825.
- 140 L. J. Murray, M. Dinca, J. Yano, S. Chavan, S. Bordiga, C. M. Brown and J. R. Long, *J. Am. Chem. Soc.*, 2010, **132**, 7856.
- 141 E. A. Stern, *Phys. Rev. B*, 1974, **10**, 3027.
- 142 B.-K. Teo and P. A. Lee, *J. Am. Chem. Soc.*, 1979, **101**, 2815.
- 143 A. G. McKale, B. W. Veal, A. P. Paulikas, S. K. Chan and G. S. Knapp, *J. Am. Chem. Soc.*, 1988, **110**, 3763.
- 144 M. Vaarkamp, I. Dring, R. J. Oldman, E. A. Stern and D. C. Koningsberger, *Phys. Rev. B*, 1994, **50**, 7872.
- 145 For a compilation of electron inelastic mean free path lengths (λ) in solids for energies in the range 0–10 000 eV above the Fermi level, see e.g. Seah, M. P.; Dench, W. A. *Surf. Interface Anal.* **1979**, *1*, 2.
- 146 A. Filipponi, *J. Phys.-Condes. Matter*, 2001, **13**, R23.
- 147 K. Asakura, *Analysis of EXAFS*, in: X-ray absorption fine structure for catalysts and surfaces; Y. Iwasawa, Ed.; World Scientific: Singapore, **1996**; Vol. 2, p. 33.
- 148 H. Nyquist, *Trans. AIEE*, 1928, **47**, 617–644. Reprinted in *Proc. IEEE* **2002** *90* 280.
- 149 C. E. Shannon, *Proc. Institute Radio Engin.*, 1949, **37**, 10–21. Reprinted in *Proc. IEEE* 1988 **86** 447.
- 150 B. H. Toby and T. Egami, *Acta Crystallogr. A*, 1992, **48**, 336.
- 151 D. A. Keen, *J. Appl. Crystallogr.*, 2001, **34**, 172.
- 152 T. Egami and S. J. L. Billinge, *Underneath the Bragg peaks: structural analysis of complex materials*; Pergamon Press: Oxford, **2003**.
- 153 S. J. L. Billinge and M. G. Kanatzidis, *Chem. Commun.*, 2004, 749.
- 154 M. Fernandez-Garcia, A. Martinez-Arias, J. C. Hanson and J. A. Rodriguez, *Chem. Rev.*, 2004, **104**, 4063.
- 155 S. J. L. Billinge and I. Levin, *Science*, 2007, **316**, 561.
- 156 F. M. Michel, L. Ehm, S. M. Antao, P. L. Lee, P. J. Chupas, G. Liu, D. R. Strongin, M. A. A. Schoonen, B. L. Phillips and J. B. Parise, *Science*, 2007, **316**, 1726.
- 157 J. L. Hodeau and R. Guinebretiere, *Appl. Phys. A-Mater. Sci. Process.*, 2007, **89**, 813.
- 158 E. S. Bozin, P. Juhás and S. J. L. Billinge, *Local structure of bulk and nanocrystalline semiconductors using total scattering methods*, in: Characterization of Semiconductor Heterostructures and Nanostructures II; G. Agostini and C. Lamberti, Ed.; Elsevier: Amsterdam, **2013**.
- 159 P. J. Chupas, X. Y. Qiu, J. C. Hanson, P. L. Lee, C. P. Grey and S. J. L. Billinge, *J. Appl. Crystallogr.*, 2003, **36**, 1342.
- 160 P. J. Chupas, K. W. Chapman, H. L. Chen and C. P. Grey, *Catal. Today*, 2009, **145**, 213.
- 161 T. Proffen and S. J. L. Billinge, *J. Appl. Cryst.*, 1999, **32**, 572.
- 162 X. Qiu, J. W. Thompson and S. J. L. Billinge, *J. Appl. Cryst.*, 2004, **37**, 678.

- 163 C. L. Farrow, P. Juhas, J. W. Liu, D. Bryndin, E. S. Bozin, J. Bloch, T. Proffen and S. J. L. Billinge, *J. Phys.-Condes. Matter*, 2007, **19**, Art. n. 335219.
- 164 A. Filipponi, *J. Phys.-Condes. Matter*, 1994, **6**, 8415.
- 165 J. L. C. Rowsell and O. M. Yaghi, *Microporous Mesoporous Mater.*, 2004, **73**, 3.
- 166 J. Hafizovic, M. Bjorgen, U. Olsbye, P. D. C. Dietzel, S. Bordiga, C. Prestipino, C. Lamberti and K. P. Lillerud, *J. Am. Chem. Soc.*, 2007, **129**, 3612.
- 167 N. L. Rosi, J. Eckert, M. Eddaoudi, D. T. Vodak, J. Kim, M. O'Keeffe and O. M. Yaghi, *Science*, 2003, **300**, 1127.
- 168 J. L. C. Rowsell, A. R. Millward, K. S. Park and O. M. Yaghi, *J. Am. Chem. Soc.*, 2004, **126**, 5666.
- 169 S. Bordiga, J. G. Vitillo, G. Ricchiardi, L. Regli, D. Cocina, A. Zecchina, B. Arstad, M. Bjorgen, J. Hafizovic and K. P. Lillerud, *J. Phys. Chem. B*, 2005, **109**, 18237.
- 170 H. Li, M. Eddaoudi, M. O'Keeffe and O. M. Yaghi, *Nature*, 1999, **402**, 276.
- 171 M. Eddaoudi, H. L. Li and O. M. Yaghi, *J. Am. Chem. Soc.*, 2000, **122**, 1391.
- 172 S. Bordiga, C. Lamberti, G. Ricchiardi, L. Regli, F. Bonino, A. Damin, K. P. Lillerud, M. Bjorgen and A. Zecchina, *Chem. Commun.*, 2004, 2300.
- 173 L. M. Huang, H. T. Wang, J. X. Chen, Z. B. Wang, J. Y. Sun, D. Y. Zhao and Y. S. Yan, *Microporous Mesoporous Mater.*, 2003, **58**, 105.
- 174 Z. Ni and R. I. Masel, *J. Am. Chem. Soc.*, 2006, **128**, 12394.
- 175 O. M. Yaghi, M. Eddaoudi, H. Li, J. Kim and N. Rosi, *Patent WO 02/088148 A1*, 2002.
- 176 M. Eddaoudi, D. B. Moler, H. L. Li, B. L. Chen, T. M. Reineke, M. O'Keeffe and O. M. Yaghi, *Accounts Chem. Res.*, 2001, **34**, 319.
- 177 B. Panella and M. Hirscher, *Adv. Mater.*, 2005, **17**, 538.
- 178 M. Milanesio, G. Artioli, A. F. Gualtieri, L. Palin and C. Lamberti, *J. Am. Chem. Soc.*, 2003, **125**, 14549.
- 179 G. Agostini, C. Lamberti, L. Palin, M. Milanesio, N. Danilina, B. Xu, M. Janousch and J. A. van Bokhoven, *J. Am. Chem. Soc.*, 2010, **132**, 667.
- 180 P. D. C. Dietzel, B. Panella, M. Hirscher, R. Blom and H. Fjellvag, *Chem. Commun.*, 2006, 959.
- 181 P. D. C. Dietzel, Y. Morita, R. Blom and H. Fjellvag, *Angew. Chem.-Int. Edit.*, 2005, **44**, 6354.
- 182 N. L. Rosi, J. Kim, M. Eddaoudi, B. L. Chen, M. O'Keeffe and O. M. Yaghi, *J. Am. Chem. Soc.*, 2005, **127**, 1504.
- 183 P. D. C. Dietzel, R. E. Johnsen, R. Blom and H. Fjellvåg, *Chem. Eur. J.*, 2008, **14**, 2389.
- 184 L. Valenzano, B. Civalieri, S. Chavan, G. T. Palomino, C. O. Arean and S. Bordiga, *J. Phys. Chem. C*, 2010, **114**, 11185.
- 185 F. Bonino, S. Chavan, J. G. Vitillo, E. Groppo, G. Agostini, C. Lamberti, P. D. C. Dietzel, C. Prestipino and S. Bordiga, *Chem. Mater.*, 2008, **20**, 4957.
- 186 S. Chavan, J. G. Vitillo, E. Groppo, F. Bonino, C. Lamberti, P. D. C. Dietzel and S. Bordiga, *J. Phys. Chem. C*, 2009, **113**, 3292.
- 187 S. Chavan, F. Bonino, J. G. Vitillo, E. Groppo, C. Lamberti, P. D. C. Dietzel, A. Zecchina and S. Bordiga, *Phys. Chem. Chem. Phys.*, 2009, **11**, 9811.
- 188 L. Valenzano, B. Civalieri, S. Bordiga, M. H. Nilsen, S. Jakobsen, K.-P. Lillerud and C. Lamberti, *Chem. Mater.*, 2011, **23**, 1700.
- 189 L. Valenzano, J. G. Vitillo, S. Chavan, B. Civalieri, F. Bonino, S. Bordiga and C. Lamberti, *Catal. Today*, 2012, **182**, 67.
- 190 P. D. C. Dietzel, V. Besikiotis and R. Blom, *J. Mater. Chem.*, 2009, **19**, 7362.
- 191 J. L. C. Rowsell, E. C. Spencer, J. Eckert, J. A. K. Howard and O. M. Yaghi, *Science*, 2005, **309**, 1350.
- 192 W. Zhou, H. Wu, T. Yildirim, J. R. Simpson and A. R. H. Walker, *Phys. Rev. B*, 2008, **78**, Art. n. 054114.
- 193 N. Lock, Y. Wu, M. Christensen, L. J. Cameron, V. K. Peterson, A. J. Bridgeman, C. J. Kepert and B. B. Iversen, *J. Phys. Chem. C*, 2010, **114**, 16181.
- 194 D. Dubbeldam, K. S. Walton, D. E. Ellis and R. Q. Snurr, *Angew. Chem.-Int. Edit.*, 2007, **46**, 4496.
- 195 S. S. Han and W. A. Goddard, *J. Phys. Chem. C*, 2007, **111**, 15185.
- 196 M. Tafipolsky, S. Amirjalayer and R. Schmid, *J. Phys. Chem. C*, 2010, **114**, 14402.
- 197 S. Amirjalayer, M. Tafipolsky and R. Schmid, *J. Phys. Chem. C*, 2011, **115**, 15133.
- 198 A. Corma, H. Garcia and F. X. Llabres i Xamena, *Chem. Rev.*, 2010, **110**, 4606.
- 199 B. Xiao, P. S. Wheatley, X. B. Zhao, A. J. Fletcher, S. Fox, A. G. Rossi, I. L. Megson, S. Bordiga, L. Regli, K. M. Thomas and R. E. Morris, *J. Am. Chem. Soc.*, 2007, **129**, 1203.
- 200 S. Bordiga, L. Regli, F. Bonino, E. Groppo, C. Lamberti, B. Xiao, P. S. Wheatley, R. E. Morris and A. Zecchina, *Phys. Chem. Chem. Phys.*, 2007, **9**, 2676.
- 201 J. H. Cavka, S. Jakobsen, U. Olsbye, N. Guillou, C. Lamberti, S. Bordiga and K. P. Lillerud, *J. Am. Chem. Soc.*, 2008, **130**, 13850.
- 202 S. Chavan, J. G. Vitillo, D. Gianolio, O. Zavorotynska, B. Civalieri, S. Jakobsen, M. H. Nilsen, L. Valenzano, C. Lamberti, K. P. Lillerud and S. Bordiga, *Phys. Chem. Chem. Phys.*, 2012, **14**, 1614.
- 203 M. Kandiah, M. H. Nilsen, S. Usseglio, S. Jakobsen, U. Olsbye, M. Tilset, C. Larabi, E. A. Quadrelli, F. Bonino and K. P. Lillerud, *Chem. Mater.*, 2010, **22**, 6632.
- 204 J. Jakobsen, D. Gianolio, D. Wragg, M. H. Nilsen, H. Emerich, S. Bordiga, C. Lamberti, U. Olsbye, M. Tilset and K. P. Lillerud, *Phys. Rev. B*, 2012, **86**, art. n. 125429.

- 205 D. Gianolio, J. G. Vitillo, B. Civalleri, S. Bordiga, U. Olsbye, K. P. Lillerud, L. Valenzano and C. Lamberti, *J. Phys.: Conf. Ser.*, 2013, in press.
- 206 R. Dovesi, R. Orlando, B. Civalleri, C. Roetti, V. R. Saunders and C. M. Zicovich-Wilson, *Z. Kristallogr.*, 2005, **220**, 571.
- 207 S. V. Kolotilov and V. V. Pavlishchuk, *Theor. Exp. Chem.*, 2009, **45**, 277.
- 208 V. K. Peterson, Y. Liu, C. M. Brown and C. J. Kepert, *J. Am. Chem. Soc.*, 2006, **128**, 15578.
- 209 H. Wu, W. Zhou and T. Yildirim, *J. Am. Chem. Soc.*, 2007, **129**, 5314.
- 210 Y. Liu, H. Kabbour, C. M. Brown, D. A. Neumann and C. C. Ahn, *Langmuir*, 2008, **24**, 4772.
- 211 J. H. Luo, H. W. Xu, Y. Liu, Y. S. Zhao, L. L. Daemen, C. Brown, T. V. Timofeeva, S. Q. Ma and H. C. Zhou, *J. Am. Chem. Soc.*, 2008, **130**, 9626.
- 212 F. M. Mulder, B. Assfour, J. Huot, T. J. Dingemans, M. Wagemaker and A. J. Ramirez-Cuesta, *J. Phys. Chem. C*, 2010, **114**, 10648.
- 213 M. Dincă, A. Dailly, Y. Liu, C. M. Brown, D. A. Neumann and J. R. Long, *J. Am. Chem. Soc.*, 2006, **128**, 16876.
- 214 M. Dincă, W. S. Han, Y. Liu, A. Dailly, C. M. Brown and J. R. Long, *Angew. Chem.-Int. Edit.*, 2007, **46**, 1419.
- 215 H. Wu, J. M. Simmons, Y. Liu, C. M. Brown, X. S. Wang, S. Ma, V. K. Peterson, P. D. Southon, C. J. Kepert, H. C. Zhou, T. Yildirim and W. Zhou, *Chem.-Eur. J.*, 2010, **16**, 5205.
- 216 H. Wu, W. Zhou and T. Yildirim, *J. Am. Chem. Soc.*, 2009, **131**, 4995.
- 217 E. D. Bloch, L. J. Murray, W. L. Queen, S. Chavan, S. N. Maximoff, J. P. Bigi, R. Krishna, V. K. Peterson, F. Grandjean, G. J. Long, B. Smit, S. Bordiga, C. M. Brown and J. R. Long, *J. Am. Chem. Soc.*, 2011, **133**, 14814.
- 218 H. Wu, J. M. Simmons, G. Srinivas, W. Zhou and T. Yildirim, *J. Phys. Chem. Lett.*, 2010, **1**, 1946.
- 219 S. S. Y. Chui, S. M. F. Lo, J. P. H. Charmant, A. G. Orpen and I. D. Williams, *Science*, 1999, **283**, 1148.
- 220 F. A. Cotton, E. A. Hillard, C. A. Murillo and H. C. Zhou, *J. Am. Chem. Soc.*, 2000, **122**, 416.
- 221 E. Borfecchia, S. Maurelli, D. Gianolio, E. Groppo, M. Chiesa, F. Bonino and C. Lamberti, *J. Phys. Chem. C*, 2012, **116**, 19839.
- 222 K. W. Chapman, G. J. Halder and P. J. Chupas, *J. Am. Chem. Soc.*, 2009, **131**, 17546.
- 223 K. W. Chapman, D. F. Sava, G. J. Halder, P. J. Chupas and T. M. Nenoff, *J. Am. Chem. Soc.*, 2011, **133**, 18583.
- 224 K. S. Park, Z. Ni, A. P. Cote, J. Y. Choi, R. D. Huang, F. J. Uribe-Romo, H. K. Chae, M. O'Keeffe and O. M. Yaghi, *Proc. Natl. Acad. Sci. U. S. A.*, 2006, **103**, 10186.
- 225 X. C. Huang, Y. Y. Lin, J. P. Zhang and X. M. Chen, *Angew. Chem.-Int. Edit.*, 2006, **45**, 1557.
- 226 K. L. Mulfort, O. K. Farha, C. D. Malliakas, M. G. Kanatzidis and J. T. Hupp, *Chem.-Eur. J.*, 2010, **16**, 276.
- 227 G. M. Day, *Crystallogr. Rev.*, 2011, **17**, 3.
- 228 MaMaSELF is the European Master in Materials Science focused on the use of Large Scale facilities (synchrotrons and neutron sources) developed within the Erasmus-Mundus frame. It involves French (Montpellier-2 and Rennes-1), German (TUM and LMU, München) and Italian (Turin) Universities as full partners and has several associated partners in Swiss, France, Germany, Italy, Russia, Japan, US and India. <http://www.mamaself.eu/>.